
Politecnico di Torino

**Politecnico di Torino**

MASTER's degree in Aerospace Engineering

# Preliminary assessment of a liquid methane powered commercial hypersonic aircraft

**Supervisor:**
Ferretto Davide
**Co-Supervisor:**
Fusaro Roberta

**Candidate:**
Azzaro Bradea
David Victor

Academic Year 2024/25

# Abstract

The renewed interest in high-speed civil transport has motivated the investigation of low-emission cryogenic fuel alternatives capable of combining extreme performance with operational viability and environmental sustainability. This thesis investigates the preliminary design and performance evaluation of a 200-passenger hypersonic transport aircraft powered by **Liquid Methane (LNG)**, identifying it as a strategic compromise between conventional kerosene and the technological challenges of cryogenic hydrogen.

The core of this work involves the development of a dedicated sizing tool in *MATLAB*. Although based on the *Hypersonic Aerospace Sizing Analysis* framework, the code underwent significant refinement to improve accuracy, most notably by implementing a dynamic calculation for mission fuel and a variable thrust sizing logic. The algorithm operates through a robust fixed-point iteration loop, calibrated on a reference vehicle, which ensures convergence to an optimal configuration.

Complementary to the sizing process, a Matching Chart analysis was conducted to define the feasible design space. This step served to validate that the selected Thrust-to-Weight ratio ($T/W$) and Wing Loading ($W/S$) satisfy the strict performance constraints across subsonic, supersonic, and hypersonic regimes.

To quantify the engineering trade-offs associated with the fuel choice, the converged LNG baseline was compared against a **Liquid Hydrogen ($LH_2$)** variant designed for the identical mission. The comparative analysis reveals a complex picture: while the superior specific impulse of hydrogen leads to a 29.7 % reduction in Maximum Take-Off Mass (MTOM) and a 54.5 % savings in fuel mass, these benefits are heavily counterbalanced by volumetric constraints. The $LH_2$ vehicle requires 188 % more fuel volume, resulting in a larger airframe that suffers a 27.0 % reduction in aerodynamic efficiency (L/D).

From an economic standpoint, a preliminary assessment for a 2035 scenario suggests that LNG maintains a decisive operational advantage, with a fuel cost per mission approximately 45% lower than hydrogen.

Environmentally, while hydrogen eliminates carbon emissions, LNG represents a good compromise. It significantly decarbonises flight compared to kerosene while avoiding the release of massive amounts of water vapour into the stratosphere, a critical drawback of hydrogen

propulsion.

The study concludes that the LNG configuration represents a viable **near-term architecture** that significantly mitigates the carbon footprint of conventional kerosene. Consequently, it stands as an optimal **transitional solution** to bridge the gap until green hydrogen technologies achieve full industrial maturity and the environmental implications of their substantial stratospheric water vapour emissions are fully addressed.

# Ringraziamenti

Scrivere queste ultime righe mi fa realizzare che questo lungo capitolo della mia vita si sta davvero concludendo. Chi mi conosce sa che la scrittura non è esattamente il mio "superpotere" e non sarò troppo poetico, ma ci tengo a ringraziare anche se brevemente chi ha reso possibile questo traguardo.

Il primo grazie va al mio relatore, il Prof. Davide Ferretto, per avermi guidato con molta gentilezza e disponibilità, e per avermi dato fiducia durante lo svolgimento di questo lavoro conclusivo con cui termina il fantastico percorso di studi vissuto al Politecnico.

Il grazie più grande, però, è per la mia famiglia. A Iulia e Francesco, per avermi dato la possibilità di intraprendere questo viaggio, anche se tutt'altro che lineare. Siete stati la mia forza e la mia tenacia, specialmente durante l'infortunio: è stato senza alcun dubbio il momento più buio e demotivante, soprattutto per me che fatico ad accettare di restare indietro e di dovermi fermare. Ma se ne sono uscito è anche merito vostro. Grazie per avermi supportato nei momenti pesanti; anche quando non esternavo le mie preoccupazioni per non impensierirvi, voi in qualche modo lo capivate sempre. Grazie soprattutto per avermi sempre lasciato libero di scegliere. Non mi avete mai rimproverato o giudicato, nemmeno quando ho deciso di "sacrificare" qualche sessione d'esame pur di preparare le barche del team e andare alle gare, rigorosamente a giugno e luglio in piena sessione estiva. Se oggi sono qui, è perché mi avete insegnato a camminare con le mie gambe.

Un pensiero speciale va ai miei nonni. A Matei, per il quale sono un piccolo genio incompreso e motivo di vanto con gli amici durante le loro intense partite a carte. Probabilmente non ha ancora capito bene cosa io abbia studiato per tutti questi anni, ma gli basta sapere che "c'entrano gli aerei" per vedermi come un "mostro". Sono sicuro che se ho intrapreso questo percorso è merito tuo e della praticità che mi hai trasmesso sin da piccolo, quando a soli 8 anni mi facevi tagliare la legna e costruire sedie senza preoccuparti troppo che mi potessi fare male, facendoti aiutare a riparare qualsiasi cosa. Grazie a questo hai stimolato la mia curiosità su come le cose vengono progettate e costruite: pensa un po', sono partito dalle sedie in legno e ora costruisco foil e barche!

A nonna Gica, che mi ha cresciuto facendomi spesso da seconda mamma. Mi fa male pensare che tu non possa vedermi oggi, ma so che in qualche modo sei qui a festeggiare

con me. Questo traguardo è anche tuo.

Un abbraccio al mio cuginetto Patrick, che mi vede come un'ispirazione e riempie i fogli disegnando aerei o improbabili "barche volanti". Mi fa sorridere che lui non abbia paura di volare "perché tanto gli aerei li controlla il cugino", a differenza della zia che continua a essere terrorizzata (ci ho provato a lavorarci su, ma è un caso perso!). E un grazie enorme al cugino più grande, Flavius, che più che un cugino è stato il fratello che non ho mai avuto. Siamo cresciuti insieme e ricordo bene la tristezza delle prime sessioni estive, quando ho realizzato che diventare grandi significava vederci sempre meno da lì in poi. Ma anche se l'università e la distanza ormai ci permettono di vederci pochissimo, ogni volta è come se il tempo non fosse passato.

Un capitolo a parte lo merita il Polito Sailing Team, a cui ho dedicato un'enorme parte del mio tempo e del mio cuore. Siete senza dubbio uno dei motivi per cui questa magistrale è durata un po' più del previsto, ma siete anche il motivo per cui è stata infinitamente meno noiosa. Mi avete dato opportunità di crescita che nessun libro avrebbe mai potuto offrirmi e siete diventati, tra un ply di "basalto" e l'altro, una vera famiglia.

Infine, agli amici e ai colleghi di corso. A chi c'è stato fin dall'inizio e a chi ho incontrato lungo la strada. Grazie per aver condiviso con me le giornate in aula studio, le ansie pre-esame e le gioie dopo il voto. E come dimenticare le giornate durante le sessioni passate chiusi in casa? La determinazione sui libri durava sì e no un'ora, per poi lasciare spazio allo studio tattico delle ricette per pranzo e cena. Ma non ricette qualunque: dovevano essere rigorosamente proteiche e anaboliche, ma comunque degne di Masterchef. Il tutto si concludeva immancabilmente con un bel: "Vabbè, oggi è andata così, ma da domani...". Abbiamo perso un mare di tempo, è vero, ma ne è valsa assolutamente la pena. Siete stati la parte migliore di questi anni a Torino.

Grazie a tutti.

# Contents

# List of Figures

# List of Tables

# Chapter 1

# Introduction

## 1.1 Motivation and general context

In the last few decades, the interest in high speed air transportation has started to grow again, mainly driven by the constant need for faster intercontinental travel and by the technological progress achieved in propulsion systems and advanced materials. Reaching **hypersonic flight**, generally defined for Mach numbers higher than five, still represents one of the greatest challenges in aerospace engineering. At such extreme speeds, every aspect of the vehicle, from aerodynamics to propulsion and structural design, becomes tightly connected, and even small changes can affect the overall performance. Designing a system that can operate efficiently while remaining lightweight, safe, and economically viable is therefore a complex multidisciplinary task.

For civil transport applications, the problem becomes even more demanding. In addition to traditional issues of propulsion efficiency and aerodynamic performance, the choice of fuel and its storage system plays a central role. At very high altitudes, emissions of $CO_2$ and water vapour can have a stronger environmental impact compared to those released at lower flight levels, because they interact directly with the upper atmosphere and can contribute to long–term climatic effects. For this reason, **alternative fuels** such as liquid methane or liquid hydrogen are being considered as possible substitutes for conventional kerosene. Among them, liquid methane appears to be a more immediate and practical option: it offers cleaner combustion, is easier to store and handle than hydrogen, and can be integrated in the near term using existing technologies. Hydrogen, while more energy dense, is still limited by the complexity and environmental cost of its production processes, which currently rely heavily on fossil sources.

Within this context, developing a reliable **preliminary design methodology** becomes fundamental. Such a tool makes it possible to assess from the very beginning whether a given hypersonic concept is technically and economically viable. In particular, it allows to investigate how variations in key input parameters such as the payload capacity, the

mission range, the type of fuel and the propulsion system affect the overall performance, mass distribution, and feasibility of the vehicle. This preliminary design phase represents a crucial step in turning a theoretical concept idea into a effective functional hypersonic aircraft.

## 1.2 Fuel selection and comparative assessment

Fuel selection represents one of the key drivers in the design of future high-speed civil transport aircraft, influencing not only propulsion efficiency and overall performance, but also tank configuration, vehicle mass distribution, and environmental footprint. Traditionally, kerosene-based fuels such as *Jet-A* or *JP-7* have dominated both commercial and military aviation due to their high energy density and, above all, their ease of handling and storage. However, the growing focus on sustainability and the need to limit greenhouse gas emissions have prompted renewed interest in alternative fuels, particularly **Liquid Methane** or **Liquid Natural Gas (LNG)** and **Liquid Hydrogen ($LH_2$)**, both of which offer significant environmental and energetic advantages for next-generation hypersonic vehicles.

### 1.2.1 Thermophysical and energetic properties

Table 1.1 summarises the main physical and energetic characteristics of kerosene, liquid methane, and liquid hydrogen.

| **Property** | **Kerosene** (Jet-A) | **Liquid Methane** (LNG) | **Liquid Hydrogen** ($LH_2$) |
|---|---|---|---|
| Density $[kg/m^3]$ | 800 | 450 | 71 |
| Heating Value $[MJ/kg]$ | 43.0 | 55.0 | 120.0 |
| Volumetric Energy Density $[MJ/L]$ | 34.4 | 22.5 | 8.5 |
| Boiling Temperature $[K]$ | 500–530 | 111 | 20 |
| $CO_2$ Emission $[kg/kg_{fuel}]$ | 3.15 | 2.75 | 0 |

**Table 1.1:** Comparison of main properties of candidate fuels for hypersonic applications

From the comparison, it emerges that methane offers a balanced compromise between performance and operational simplicity. Compared to kerosene, it provides approximately 25 % higher specific energy per unit of mass, while reducing carbon dioxide emission by approximately 13 %. At the same time, its boiling point of 111 K allows storage under moderately cryogenic conditions, much less demanding than the 20 K required for hydrogen. The volumetric energy density, though lower than that of kerosene, is considerably greater than that of liquid hydrogen.

Unlike kerosene, methane combustion produces negligible soot and unburned hydrocarbons, reducing non-$CO_2$ climate forcing effects (i.e., mitigating indirect warming effects such

as contrail formation, water vapour emissions, and $NO_x$-induced ozone production that contribute to atmospheric radiative forcing beyond $CO_2$ emissions).

The combination of these properties makes LNG particularly suitable for hypersonic aircraft, where energy content, thermal behaviour, and storage efficiency are key drivers for both performance and design feasibility.

### 1.2.2 Environmental considerations

From an environmental perspective, liquid methane can achieve up to **30% lower life-cycle greenhouse gas emissions** compared to conventional jet fuels, provided that methane leakage during extraction and transport is minimised. Among hydrocarbon fuels, methane contains the lowest carbon fraction and its complete combustion yields only water and carbon dioxide, following the simple stoichiometric reaction:

$$CH_4 + 2O_2 \rightarrow CO_2 + 2H_2O$$

To further illustrate the difference in **carbon emissions**, burning $1,000\ l$ of kerosene produces approximately $2,520\ kg$ of $CO_2$, whereas the same volume of liquid methane generates about $1,237.5\ kg$ of $CO_2$, corresponding to a reduction of nearly 51 %.

| **Fuel** | **Mass [kg]** | **$CO_2$ Emissions [kg]** |
|---|---|---|
| Kerosene (Jet-A) | 800 | 2,520 |
| Liquid Methane (LNG) | 450 | 1,237.5 |

**Table 1.2:** Comparison of $CO_2$ emissions for the combustion of 1000 $l$ of kerosene and LNG.

Hydrogen, although the cleanest fuel in terms of direct emissions, still faces substantial technological and environmental challenges. Its low density demands large cryogenic tanks, up to ten times the volume of kerosene ones, introducing severe penalties in terms of aerodynamic drag, vehicle size, and mass distribution. Moreover, current industrial production of hydrogen, mainly based on steam reforming of natural gas, remains energy-intensive and carbon-intensive. Even so-called "green hydrogen," produced through water electrolysis using renewable energy, is limited by low efficiency, high cost, and limited infrastructure.

Methane, conversely, benefits from a well-established global supply chain and mature cryogenic handling technology, already proven in the aerospace and marine sectors. This makes LNG an immediately deployable solution capable of supporting the progressive decarbonisation of aviation.

### 1.2.3 Comparative overview

Figure 1.1 shows a comparison between the **specific and volumetric energy densities** of the three fuels. Hydrogen clearly offers the highest energy per unit mass but the lowest

per unit volume, leading to practical much lower usability and design penalties in vehicle size. Methane instead offers a more balanced compromise, providing a higher performance than kerosene while mitigating the extreme cryogenic and volumetric penalties of hydrogen.

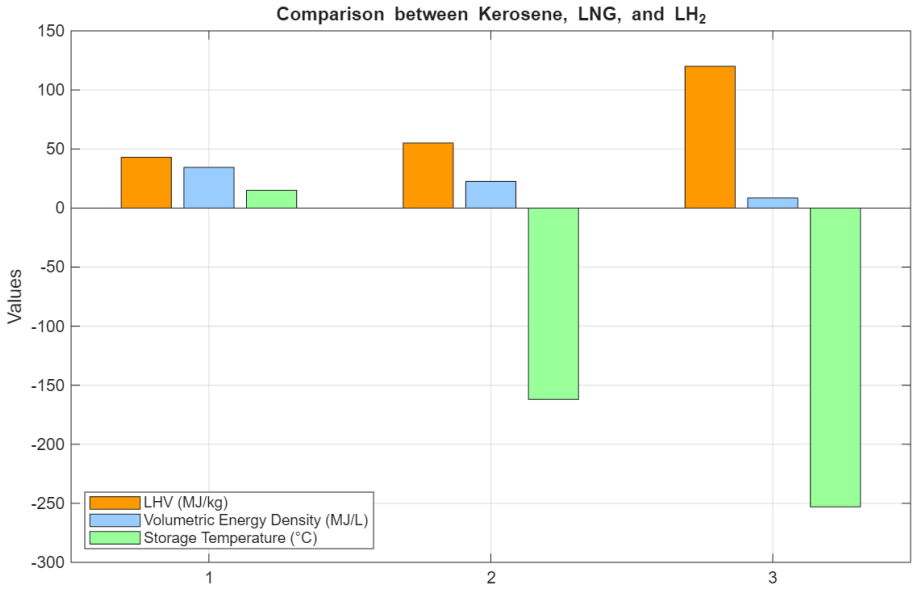


**Figure 1.1:** Comparison between specific & volumetric energy densities and storage temperature of Kerosene, LNG and $LH_2$.

In summary, liquid methane presents a favourable thermodynamic and energetic profile, combining manageable storage conditions with a measurable reduction in environmental impact. Although methane does not achieve the zero-carbon potential of hydrogen, its production and storage technologies are already mature and are globally available. Therefore, LNG represents a practical and realistic **transitional solution** towards cleaner aviation fuels, as it can be adopted in the short term using existing industrial infrastructure. At the same time, it enables the gradual introduction of hydrogen-based propulsion systems, making their future adoption smoother as the related technologies become more sustainable and economically viable.

Even if it is not a fully carbon-free option the combination of efficiency, lower environmental impact and greater technological readiness makes **Liquid Methane** an **ideal candidate for near-term hypersonic civil transport applications**.

## 1.3 Historical background of hypersonic flight

The ambition to fly at hypersonic speeds has accompanied aerospace development since the early years of the space age. Initially motivated by military and scientific objectives, hypersonic research progressively expanded toward atmospheric re-entry, advanced propulsion systems, and, more recently, civil transport applications. During the past seven decades, numerous experimental programmes have contributed to the establishment of the physical

understanding, technological capabilities, and design methodologies required for sustained flight in this extreme regime.

### 1.3.1 Early developments

One of the first milestones in hypersonic research was the ***X-15*** programme, conducted by NASA and the U.S. Air Force between 1959 and 1968. The rocket-powered X-15 reached a maximum speed of Mach 6.7 and altitudes exceeding $100km$, providing invaluable flight data on aerodynamic heating, control effectiveness, and pilot handling at high Mach numbers. Although not air-breathing, the X-15 established the foundation for modern hypersonic aerothermodynamics and thermal protection design.


**Figure 1.2:** X-15

**Figure 1.3:** X-30

During the 1980s, the U.S. initiated the ambitious *National Aero-Space Plane (NASP)* programme. The goal of NASP was to develop a **single-stage-to-orbit (SSTO)** vehicle powered by a scramjet-based propulsion system; this experimental aircraft concept was designated the **X-30**. Despite its premature cancellation in the early 1990s, the programme advanced critical technologies in computational fluid dynamics, lightweight structures, and high-temperature materials, many of which later influenced subsequent hypersonic demonstrators.

### 1.3.2 Modern experimental programmes

During the early 2000s, a series of international experiments marked the transition from purely theoretical studies to real flight tests of hypersonic concepts driven by air-breathing engines. Australia's ***HyShot*** project (2002) achieved the first successful in-flight ignition of a scramjet engine. Soon after, the United States launched the ***HIFiRE*** programme (Hypersonic International Flight Research Experimentation), which conducted several missions exploring flight regimes between Mach 5 and Mach 8.

NASA's ***X-43A***, whose first flight attempt took place in 2001, and Boeing's ***X-51A Waverider*** (2010–2013) further demonstrated sustained scramjet powered flight, with the

latter reaching speeds around Mach 7 for several minutes, a historic achievement for air-breathing hypersonic propulsion.

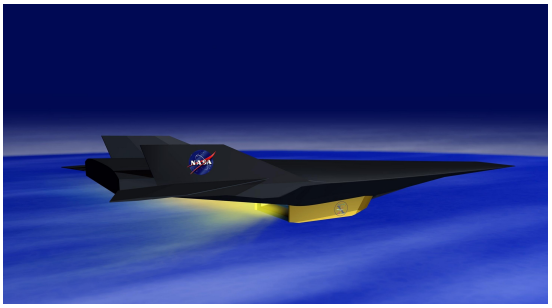

**Figure 1.4:** X-43 A

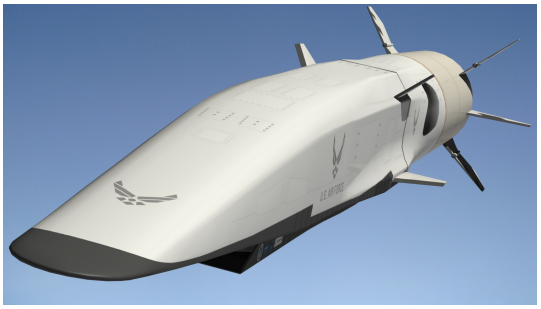

**Figure 1.5:** X-51A Waverider

At the same time, European research programmes were initiated to investigate hypersonic flight for both civil and environmental purposes. Among these, the **HEXA-FLY** project, coordinated by the *European Space Agency (ESA)* and launched in 2014, focused on high-speed sustainable transport and re-entry demonstrators. The project addressed key challenges such as aerodynamic efficiency, noise reduction, and emissions within a coordinated European framework.

### 1.3.3 High-speed civil transport concepts

While most of the early hypersonic programmes were primarily military or experimental, the last decades have seen growing interest in applying these technologies to high-speed **civil transportation**. *NASA*, together with its industrial partners, such as the *Lockheed California Company* and *McDonnell Douglas Corporation*, developed several conceptual design studies to assess the feasibility of hypersonic airliners operating at Mach 6.

The operating environment of a hypersonic aircraft differs significantly from that of conventional subsonic transport, and because of this, notable changes in configuration and structural layout are inevitable. At such extreme speeds, aerodynamic efficiency dictates that the wings must be thin and compact to minimise drag, which in turn limits their internal volume for fuel storage. As a consequence, fuel tanks must be accommodated within the fuselage, introducing new constraints on internal layout, since the same volume must also house the payload and pressurised cabin.

Different **fuselage shapes** were investigated to address this challenge, with circular and elliptical cross-sections emerging as the most promising options. Several fuselage–wing integration concepts were also explored for a Mach 6 civil transport, including conventional wing–body, semi–blended wing–body, and fully blended wing–body configuration, also known as “waverider”.

A further design variable concerned the type of **fuel tank**, either *integral*, where the tank is built into the airframe, or *non-integral*, where separate insulated tanks are installed within the structure. Although integral tanks provide higher volumetric efficiency, they pose issues

related to structural integrity and heat transfer between the fuel and the airframe at high temperatures.

In the mid 1970s, the *McDonnell Douglas Corporation* conducted an extensive comparative study on various fuselage and fuel-tank arrangements for a 200-passenger Mach 6 transport aircraft fueled with liquid hydrogen designed for a range of approximately $9,260\,km$ (Ref. [1]). Three main configurations were examined:

- Circular wing–body with non-integral fuel tanks,
- Circular wing–body with integral fuel tanks,
- Elliptical blended wing–body with integral fuel tanks.

Among these, the **elliptical blended wing–body** with integral tanks was identified as the most promising design, combining the lowest structural weight with the greatest range potential. Its superior performance was attributed to the higher aerodynamic efficiency and the greater use of internal volume.

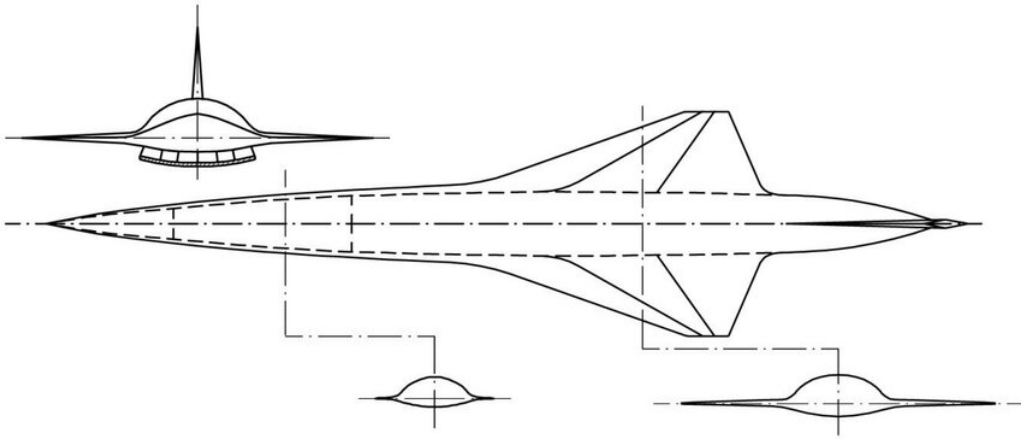

**Figure 1.6:** Elliptical blended wing–body configuration [2]

By the beginning of the 1980s, NASA launched the ***HYCAT*** programme, which comprised five conceptual configurations, from *HYCAT-1* to *HYCAT-5*. Each variant, shown in Figure 1.7, explored different aerodynamic layouts and propulsion architectures with the aim of defining an optimal Mach 6 transport concept capable of carrying approximately 200 passengers over intercontinental distances. Among these concepts, the *HYCAT-1* and *HYCAT-4* configurations demonstrated the most promising performance, leading to the development of a sixth and final prototype, the *HYCAT-1A*, which combined the strengths of both two preceding designs.

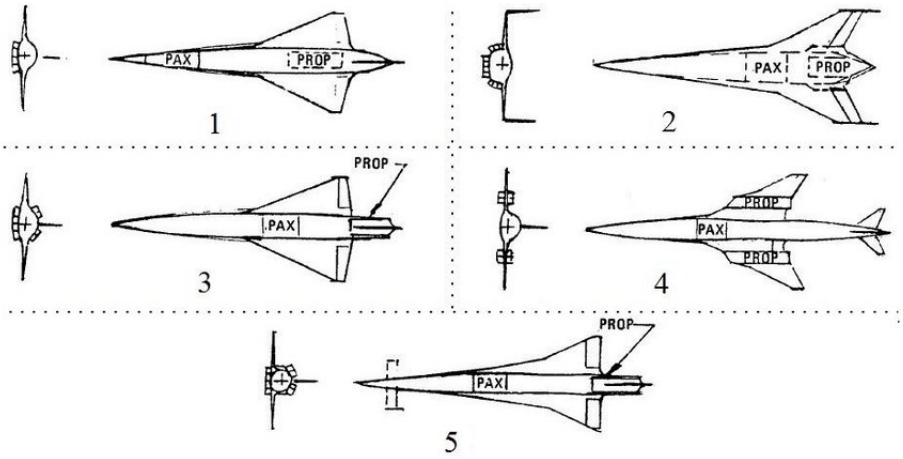


**Figure 1.7:** The *HYCAT* family of airliners

Specifically, the *HYCAT-1* was characterised by a tailless blended-body layout with engines mounted beneath the fuselage. In contrast, the *HYCAT-4* incorporated conventional horizontal and vertical tail surfaces. It introduced a distinctive "over-under" propulsion system, integrating a turbojet engine above the wing and a scramjet below.

Among all designs, the *HYCAT-1A* emerged as the most promising configuration. It was derived from the highly efficient aerodynamic layout of the original *HYCAT-1*, which served as a baseline and was subsequently modified to enhance stability and passenger accommodation. The updated configuration introduced a horizontal tail and wing flaps, while the cabin layout was redesigned into a double-deck arrangement to optimise internal volume and comfort.

## 1.4 Thesis objectives and methodology

The primary goal of this thesis is the development of a **preliminary design code** for a liquid methane powered hypersonic transport aircraft. The tool, implemented in MATLAB, partially builds on the methodology of NASA's *Hypersonic Aerospace Sizing Analysis (HASA)* framework, adapting and extending it to accommodate the use of alternative fuels and updated mission requirements.

Through an **iterative process**, the code estimates the **geometric characteristics** and the **mass breakdown** of the vehicle. In addition, it generates key performance diagrams, such as **Payload–Range** and **Matching Charts**, and produces a preliminary **two-dimensional sketch** of the overall layout, including the wing and tail surfaces. Beyond the development of the design tool itself, this work also aims to assess the technical feasibility of a hypersonic transport concept powered by liquid methane, examining its potential advantages and limitations within the current technological and operational context. In this regard, the *HYCAT-1A* configuration has been adopted in the present work as the primary reference model for developing and validating the proposed preliminary design

methodology.

## 1.5 Structure of the thesis

The thesis is structured as follows:

- **Chapter 1 – Introduction:** provides the general motivation and context of the work. The chapter begins with an overview of current challenges in high-speed and hypersonic air transport, followed by a comparative assessment of candidate fuels with particular attention to liquid methane as a viable alternative for near-term applications. The chapter then contains a brief historical overview of hypersonic flight and concludes with an outline of the objectives of the study.
- **Chapter 2 – Reference Mission and Aircraft:** describes the baseline configuration *HYCAT-1A*, which serves as a reference vehicle for the present study. The chapter presents the mission profile, aerodynamic characteristics, and adopted propulsion system.
- **Chapter 3 – Mission Trajectory:** outlines the modelling of the mission profile and the corresponding numerical implementation, through the different flight phases: climb, cruise, and descent. The definition of the trajectory is fundamental because it is needed to estimate the fuel consumption and key performance parameters, which are later used in the design analysis.
- **Chapter 4 – Preliminary Design Method:** presents the custom MATLAB code developed for the thesis. This chapter describes the adopted methodology, the input parameters required, and the overall sizing process, including both geometric and weight estimation. In addition, there are two dedicated sections to explain the equations used to compute the fuel fractions and the graphical reconstruction of the aircraft geometry.
- **Chapter 5 – Results and Performance Evaluation:** reports the results obtained from the preliminary design analysis, including the matching chart diagrams for subsonic, supersonic, and hypersonic regimes, as well as the payload–range diagram. The chapter concludes with some considerations about the feasibility of the methane-powered hypersonic transport configuration.
- **Chapter 6 - Comparative Analysis: Liquid Hydrogen Case Study:** expands the analysis by introducing a Liquid Hydrogen ($LH_2$) powered variant. This configuration is sized using the identical methodology to provide a direct benchmark, allowing for a detailed discussion of the mass, geometric, aerodynamic, and economic trade-offs between the two vehicles.
- **Chapter 7 - Conclusions and Future Work:** concludes the thesis by summarising the key findings and the overall viability of the LNG configuration in light of the

comparison. It also outlines the limitations of the current model and suggests key areas for future research.

- **Appendix A – The International Standard Atmosphere (ISA) Model:** provides the reference equations and parameters used to model the atmospheric properties required for the performance calculations.

# Chapter 2

# Reference Mission and Aircraft

This chapter introduces the reference mission and aircraft configurations, focussing on the *HYCAT-1A* and *HYCAT-1* configurations. These concepts, originally investigated within NASA's Hypersonic Aerospace Sizing Analysis (HASA) framework and further investigated by Lockheed under the contract *NAS1-15057*, provide a solid foundation for the present study. Their mission profiles, mass breakdowns, and aerodynamic datasets are extensively documented, ensuring that the design process relies on validated and traceable information rather than speculative assumptions. In particular, the aerodynamic coefficients derived for the *HYCAT-1* configuration have been used to reconstruct the drag polar across a wide Mach number range, from subsonic conditions up to Mach 6, while the comparative analysis of propulsion architectures presented in the Lockheed study supports the selection of the most suitable engine configuration for the target mission.

The *HYCAT-1A* concept represented one of the most advanced proposals for a hypersonic civil transport vehicle, developed during the 1980s by the *Lockheed California Company*. It was envisioned as a Mach 6 transport aircraft with the capacity to carry approximately 200 passengers over a maximum range of 9260 km (5000 nautical miles). The design was part of NASA's broader effort to assess the feasibility of long-range and high-speed civil aviation, with the specific aim of complementing or surpassing the operational envelope of the *Concorde* and other supersonic transports of that era.

From a configuration point of view, the *HYCAT-1* adopted a tailless layout with highly integrated lifting surfaces, optimised to minimise wave drag and ensure efficient cruise performance at hypersonic speeds. The subsequent variant, *HYCAT-1A*, introduced refinements in geometry and mass distribution, and is often cited in the literature as the most representative version for performance assessment. These configurations are particularly suitable for conceptual design studies, as they provide a well documented geometric baseline together with performance and aerodynamic data validated against wind tunnel testing.

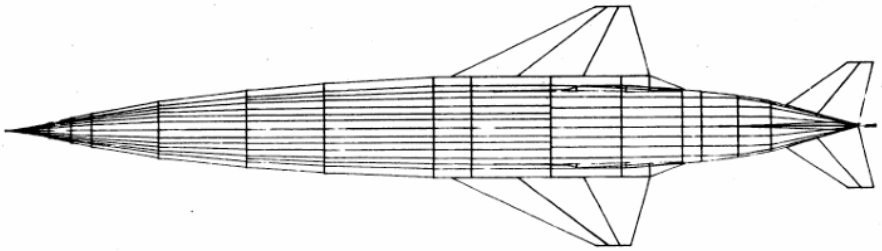

**Figure 2.1:** Hycat-1A basic configuration

## 2.1 Mission

The experience of the *'Concorde'* has demonstrated the technical feasibility of high-speed transatlantic flight. However, no comparable supersonic or hypersonic aircraft has ever been operated on long-range transpacific routes. This absence is particularly significant in the context of the Pacific Rim, one of the most densely connected regions in terms of long-haul air traffic, with numerous intercontinental routes linking Asia to the western coast of the Americas. In this context, the development of a hypersonic aircraft capable of covering intercontinental distances is not only technologically justifiable but also strategically important in terms of connectivity and competitiveness.

To define the **design range**, several representative long-haul routes between major U.S. hubs and key cities in the Asia–Pacific region were examined. Among them are San Francisco – Tokyo ($8,300\,km$), San Francisco – Shanghai ($9,900\,km$), Tokyo – Los Angeles ($8,800\,km$), Tokyo – Seattle ($7,710\,km$) and Seattle – Beijing ($8,700\,km$). These routes were selected because they are among the most demanding in terms of distance, traffic, and strategic interest.

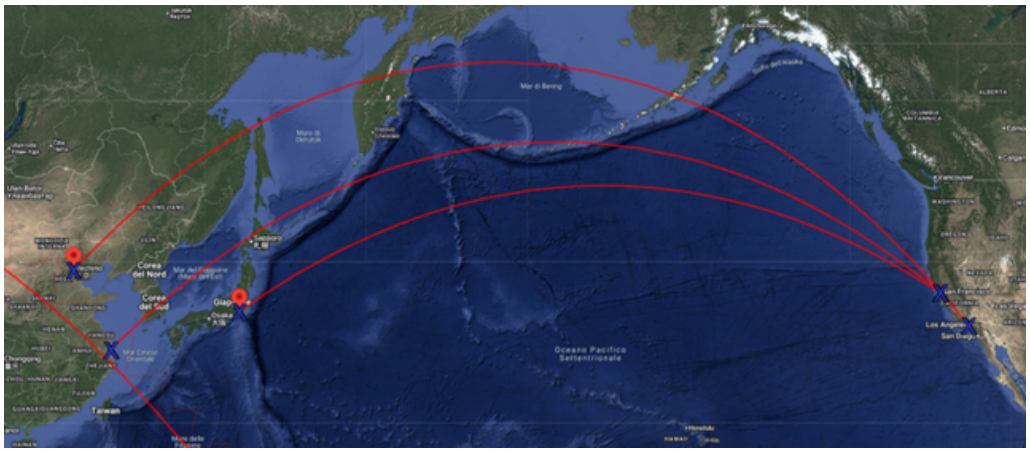


**Figure 2.2:** Over Pacific routes

Based on the findings of this survey, the design requirement for the range of the aircraft was established at $\mathbf{10,000\,km}$. This capability allows continuous intercontinental flights across the Pacific Ocean, without the need of refuelling stops, and leaves an operation margin to account for operational flexibility, allowing efficient point-to-point flights between locations such as Los Angeles and Beijing or San Francisco and Shanghai within a single flight.

## 2.2 Aerodynamic

In reference [3], the aerodynamic characteristics of the vehicle were assessed using different theoretical approaches. Specifically, the *Vortex Lattice Lifting Surface* theory was applied to evaluate the subsonic and supersonic regimes, while the *Hypersonic Arbitrary Body Aerodynamic* computer programme was used for the hypersonic domain. In addition, the *NASA Wave Drag program* was used to estimate the wave drag contribution. The theoretical results were subsequently validated by comparison with wind tunnel data obtained from a scale model of the *HYCAT-1*.

### 2.2.1 Lift coefficient

The following Figure 2.3 illustrates the variation of the lift coefficient with the Mach number for three representative angles of attack: 4°, 8° and 12°. These angles were selected to capture the aerodynamic behaviour of the configuration across different flight attitudes, ranging from moderate to high lift conditions. The lift coefficient increases with the angle of attack, showing the expected trend as the Mach number increases from the subsonic to the hypersonic regime. It should be noted that the curve corresponding to an angle of attack of 12° terminates around Mach 1, since such a high angle is typically encountered only during low-speed phases such as take-off and approach.

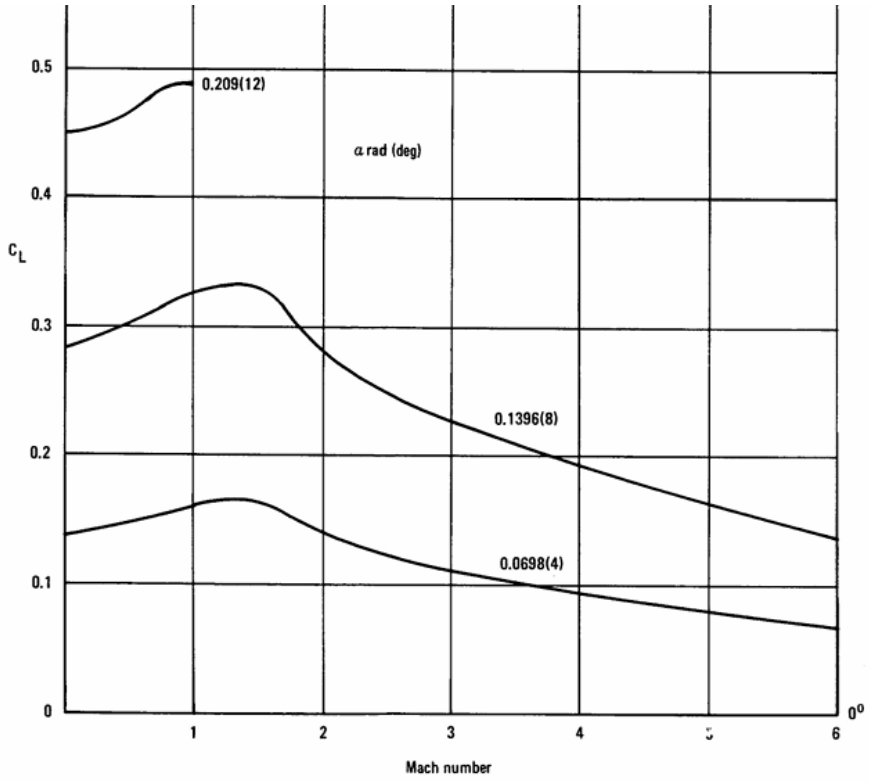


**Figure 2.3:** HYCAT-1A, lift coefficient

### 2.2.2 Drag coefficient

In aerodynamics, the total drag force is typically classified into three main components: friction drag, induced drag, and wave drag:

- ***Friction drag***, often referred to as skin-friction drag, arises from viscous effects within the boundary layer along the aircraft surfaces. This type of drag is strongly influenced by the overall surface area, the roughness of the surface, and the Reynolds number associated with the flow conditions.
- ***Induced drag*** arises from the generation of lift, being directly linked to the strength of wingtip eddies. Its coefficient generally increases with the Mach number, reaching a maximum in the transonic or low supersonic regime. Beyond this point, it decreases, becoming lower than its subsonic values once the Mach number exceeds approximately 2.
- ***Wave drag*** arises because of compressibility effects that become prominent at transonic and supersonic speeds. This phenomenon is primarily attributed to the formation of shock waves, which induce pressure discontinuities on the aircraft surfaces. As the Mach number approaches unity, wave drag rapidly increases and can become the predominant source of drag at higher speeds.

The **total drag coefficient** of the vehicle is evaluated using the build-up method, ex-

pressing the overall drag as the sum of three main components:

$$C_D = C_{D_i} + C_{D_f} + C_{D_w} \tag{2.1}$$

In this study, the **induced and wave drag** contributions for the *HYCAT-1A* baseline configuration were not recalculated. Instead, these data were adopted directly from the reference report [3], where they were evaluated during the original *HYCAT* programme. These coefficients are shown in Fig. 2.4 & 2.5. In contrast, the friction drag values were not explicitly provided in the reference reports.

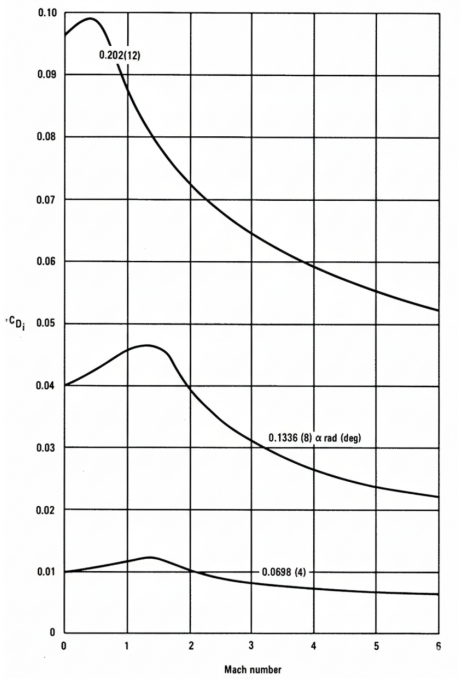


**Figure 2.4:** HYCAT-1A, induced drag

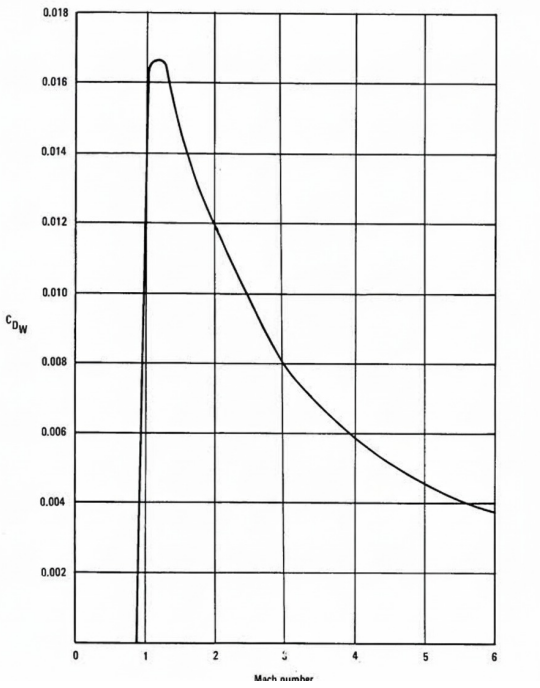


**Figure 2.5:** HYCAT-1A, wave drag

Since the *HYCAT-1* is a horizontal tailless configuration, the **friction drag** over the Mach range was derived from available data on both *HYCAT-1* and *HYCAT-4*, the latter including a horizontal tail. The reference also provides the incremental drag contribution associated with various components, which allows the application of the build-up method. Based on the founded increments, the horizontal tail is estimated to contribute about 5 % of the total zero-lift drag at Mach 6, a value consistent with expectations for similar high-speed configurations. The friction drag coefficient of *HYCAT-1A* is calculated using the following equation:

$$C_{D_f}|_{HYCAT-1A} = C_{D_f}|_{HYCAT-1} + 0.05 \cdot C_{D_f}|_{HYCAT-4} \tag{2.2}$$

To generate the friction drag curve for the *HYCAT-1A* configuration, first the available data for *HYCAT-1* and *HYCAT-4* were used to reconstruct their two curves in *MATLAB*,

reported in Figures 2.6 & 2.7. Then, assuming a uniform 5 % contribution from the horizontal tail, the corresponding friction drag for the *HYCAT-1A* was derived.

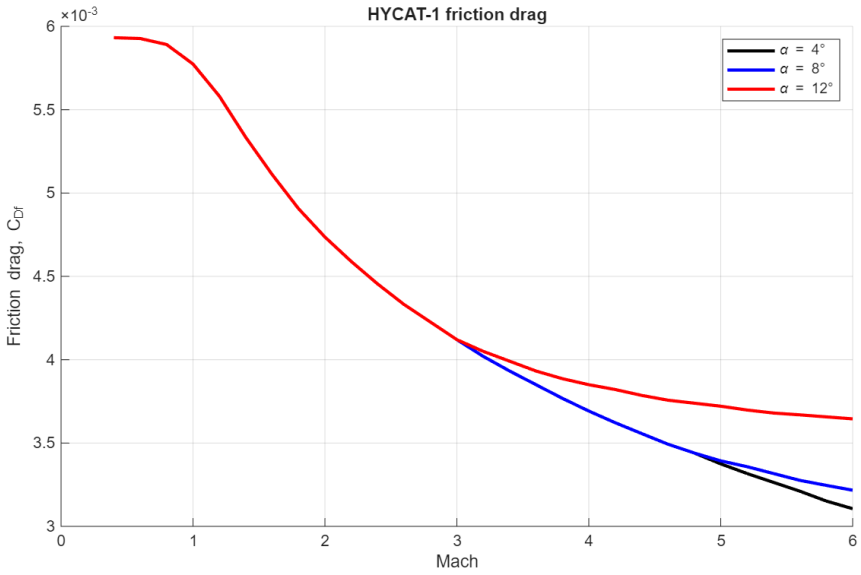


**Figure 2.6:** HYCAT-1, friction drag

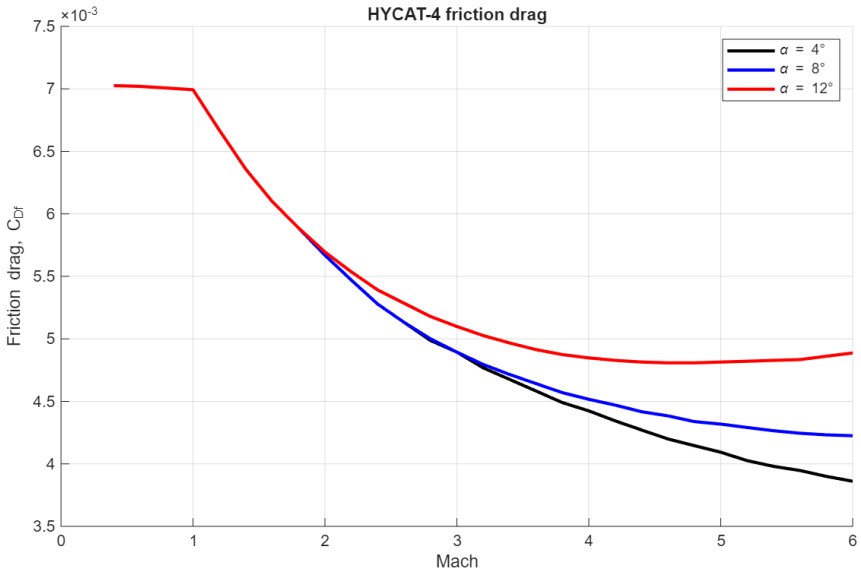


**Figure 2.7:** HYCAT-4, friction drag

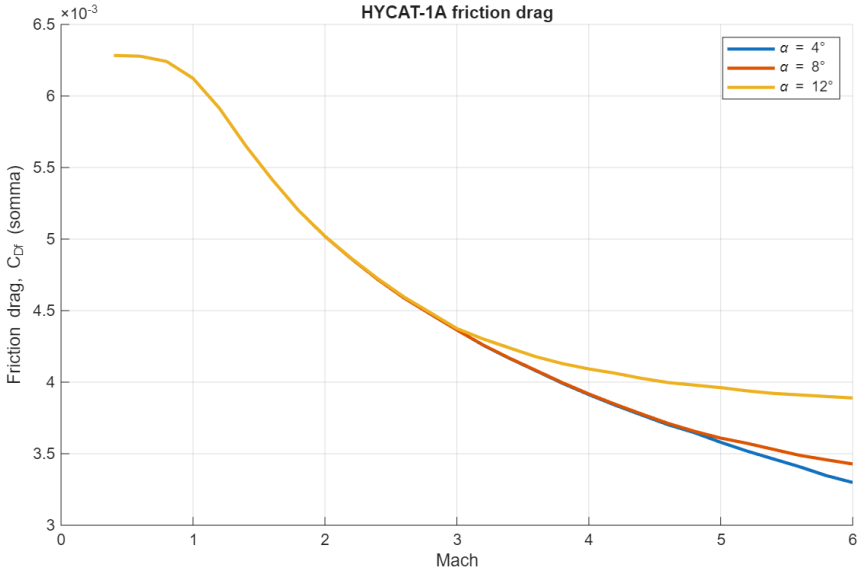


**Figure 2.8:** HYCAT-1A, friction drag

### 2.2.3 Low speed aerodynamic

The **low-speed aerodynamic characteristics** of the same aircraft were also analysed and presented in Ref. [3]. Figure 2.9 illustrates the drag polar of the *HYCAT-1A* configuration at Mach 0.35, both with the flaps retracted and extended, and accounting for the presence or absence of the ground effect. In the same figure, the variation of the lift coefficient $C_L$ with the angle of attack $\alpha$ is reported under the same conditions. These data are used for take-off and landing performance calculations.

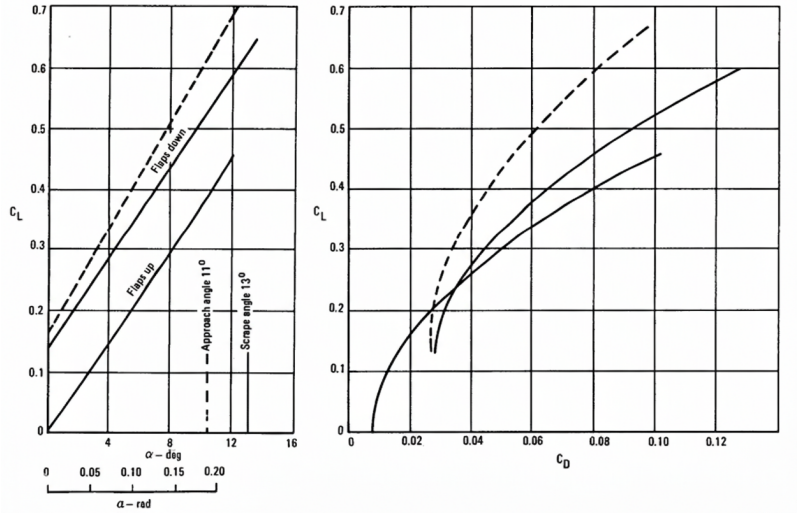


**Figure 2.9:** HYCAT-1A, low speed CL and CD

## 2.3 Propulsion system

A vehicle designed to operate at hypersonic speeds must be able to maintain efficient performance over a wide range of Mach numbers, a requirement that cannot be satisfied by a single propulsion system. For this reason, multiple propulsion modes are often integrated within the same system, forming what is referred to as a *Combined Cycle Engine (CCE)*. Two main categories of such systems exist: the *Turbine-Based Combined Cycle (TBCC)* engine and the *Rocket-Based Combined Cycle (RBCC)* engine.

Air-breathing propulsion systems, such as the TBCC, are generally preferred for atmospheric flight, even at elevated altitudes, because they utilise the surrounding ambient air for combustion rather than relying on onboard oxidizer storage. This feature significantly reduces the overall mass of the vehicle and improves propulsive efficiency. Considering that the design objective of this study is to achieve a cruise speed of Mach 6, the **Turbine-Based Combined Cycle engine** was selected as the most appropriate propulsion concept.

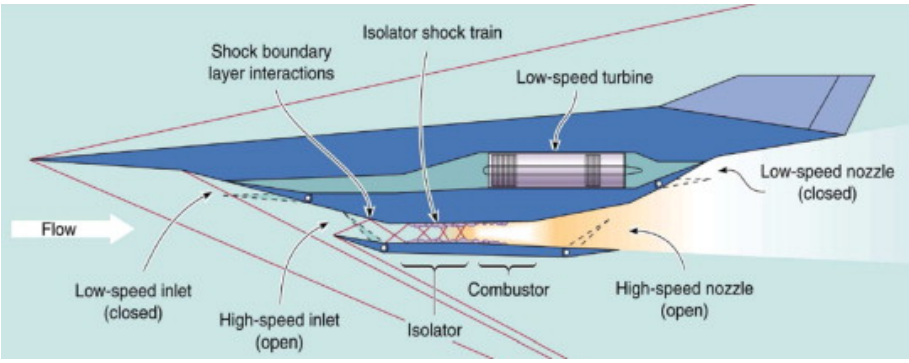


**Figure 2.10:** Turbine Based Combined Cycle propulsion concept [4]

### 2.3.1 Turbine-Based Combined Cycle in "Over-Under" configuration

Turbine-Based Combined Cycle (TBCC) propulsion systems integrate **two distinct operating modes** to efficiently cover a wide range of flight conditions. At lower Mach numbers, propulsion is provided by a **turbine-based cycle**, typically a *turbojet* or *turbofan*, which provides efficient performance during take-off, climb, and subsonic to transonic cruise. As the vehicle accelerates into the supersonic and hypersonic regimes, the system switches to a **ram-based cycle**, such as a *ramjet* or *scramjet*, which becomes more effective as the dynamic pressure increases. This staged operational approach allows the engine to maintain good efficiency and stable thrust production across the entire flight envelope, from take-off to hypersonic cruise. A detailed description of the primary engine types suitable for this application is provided below:

- The **TurboJet** is a jet engine that uses a turbine-driven compressor to pressurise the incoming air before mixing it with fuel for combustion. The resulting high energy

exhaust gases pass through a turbine which drives the compressor and are then expelled through a nozzle to produce thrust. Turbojets are particularly well-suited for subsonic and low-supersonic speeds, remaining effective up to approximately Mach 2–3.

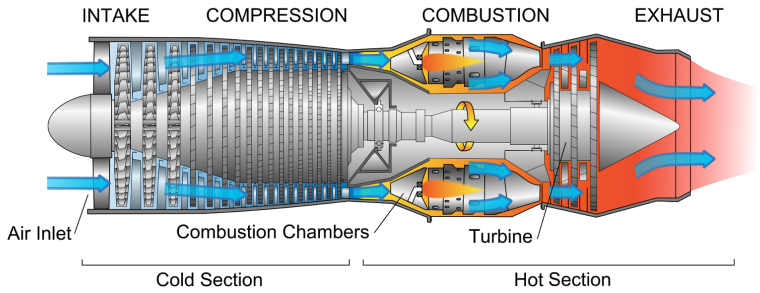


**Figure 2.11:** TurboJet engine

- The **RamJet**, on the contrary, has no moving parts such as compressors or turbines. It relies entirely on the high forward speed of the vehicle to compress the incoming air. The air enters through an inlet, is compressed by ram pressure, mixed with fuel in the combustion chamber, ignited, and expelled at high velocity through the nozzle. Ramjets cannot operate efficiently at subsonic or transonic speeds, but they perform effectively between Mach 3 and Mach 6.

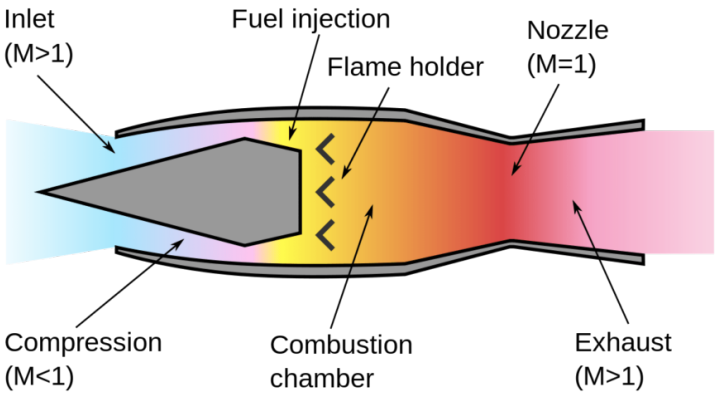


**Figure 2.12:** RamJet engine

- The **ScramJet**, known as "*supersonic combustion ramjet*", is an evolved version of the ramjet used for flight over Mach 6. Unlike the conventional ramjet, the airflow through the combustion chamber remains supersonic throughout the combustion process. This enables operation in the hypersonic regime, typically between Mach 6 and Mach 10, while maintaining high efficiency at extreme speeds.

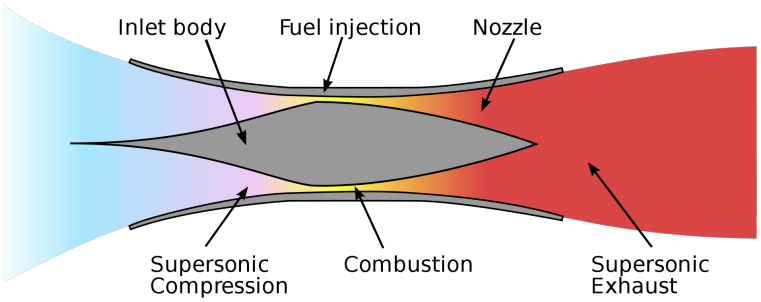


**Figure 2.13:** ScramJet engine

Two main architectural layouts can be commonly adopted: the "***Wrap-Around***" and the "***Over-Under***" configurations. In the wrap-around design, the ram-based flow path is arranged around the turbine-based engine, and the two cycles share a common inlet and nozzle. In contrast, in the over-under configuration, the combustion chambers and flow paths are separated with the turbine-based engine mounted above the ram-based engine.

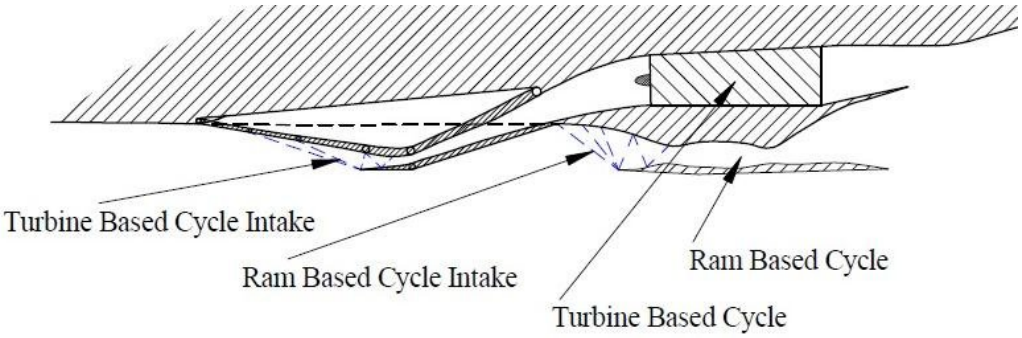


**Figure 2.14:** Turbine Based Combined Cycle in "Over-Under" configuration [5]

The "over-under" configuration was identified by NASA as the most suitable architecture for hypersonic applications due to its aerodynamic integration potential and reduced interference between propulsion streams. For these reasons, it has been adopted as the design configuration in both the *HYCAT-1* and *HYCAT-1A* vehicles where the engines are mounted directly beneath the fuselage, with the propulsion system being totally integrated into the body and the skin making up part of the intake and nozzle structure.

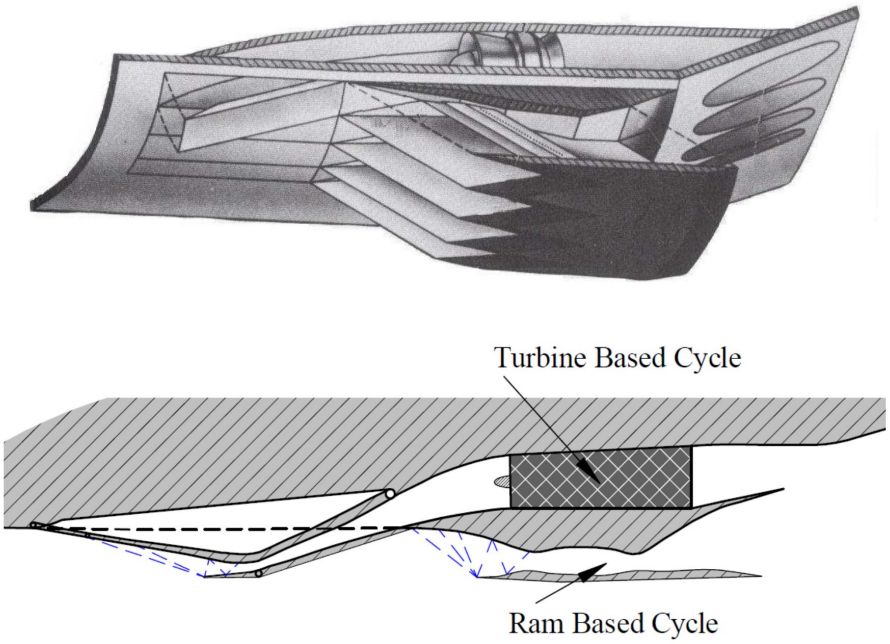


**Figure 2.15:** Turbine Based Combined Cycle in "Over-Under" configuration with separated intake and nozzle [5]

In the research conducted under NASA contract *NAS1-15057*, two alternative *Turbine-Based Combined Cycle (TBCC)* propulsion concepts were thoroughly analysed, as documented in Report [6]. The **first configuration**, depicted in Figure 2.16, consists of a turbojet equipped with a variable geometry inlet and a **scramjet** with a separate fixed geometry. The **second configuration**, illustrated in Figure 2.17, instead features a single variable geometry inlet shared between a turbojet and a **ramjet** engine. In the latter case, a movable flap is required to divert the airflow between the two propulsion cycles.

Although the fixed-geometry scramjet of the first configuration simplifies the overall design by eliminating the need for other moving components, it also introduces significant drawbacks. The exposed intake of the scramjet leads to high installation drag during both subsonic and transonic flight when the scramjet is turned off, and the fixed geometry of the scramjet intake exhibits limited airflow capacity during the regime in which it is turned on.

On the other hand, the second configuration offers several advantages: reduced drag at low Mach numbers, higher amount of thrust in the supersonic regime due to the variable inlet, and the elimination of the need for the turbojet inlet retraction. However, its main limitation lies in the maximum attainable flight speed, since the specific impulse of the ramjet decreases rapidly beyond Mach 6 compared to the scramjet.

A total reduction of approximately 2.5 - 3.0 % in total gross weight appears achievable by employing a ramjet as the ram-based engine instead of a scramjet. This weight decrease lies in the lower mass of the propulsion system and the reduced fuel consumption, the latter resulting from the higher installation drag associated with the scramjet configuration at

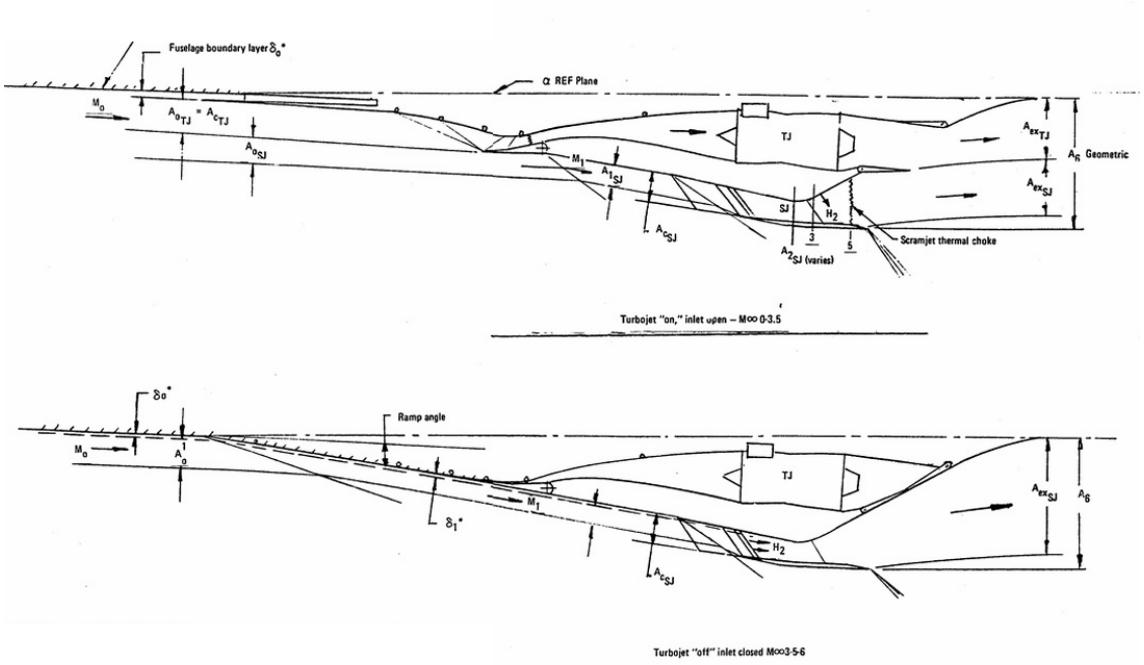


**Figure 2.16:** Turbojet-Scramjet system with separate inlet

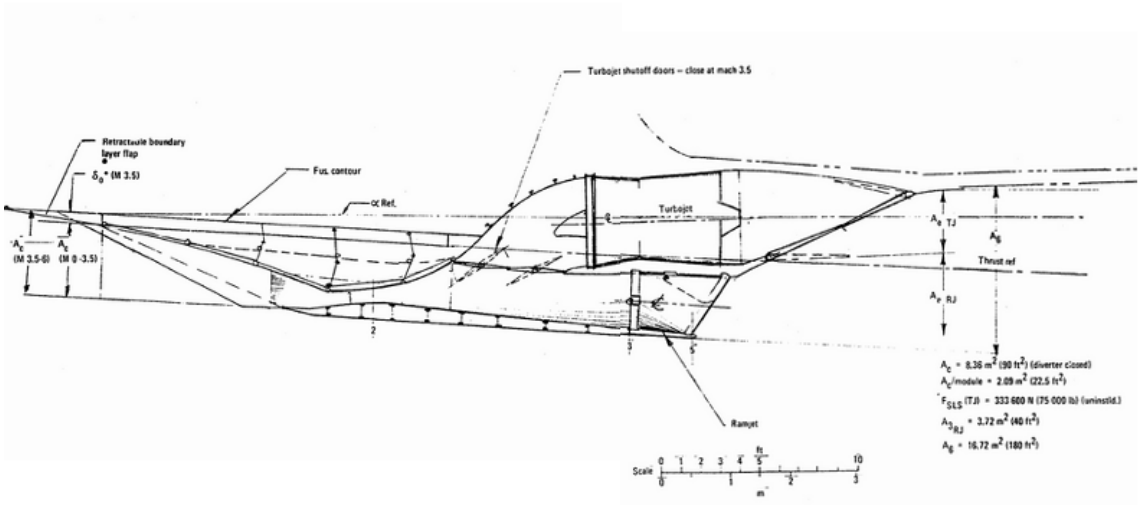


**Figure 2.17:** Turbojet-Ramjet system with Common Variable Geometry Inlet

lower speeds. In particular, the scramjet exhibits a noticeable drag peak around transonic conditions and up to Mach 1.5. Furthermore, near Mach 3.5, when the turbojet is shut down, a deficiency in the available thrust from the scramjet is observed, requiring either an increase in the inlet capture area to sustain performance or the extension of turbojet

operation to higher Mach numbers in order to benefit from the corresponding rise in dynamic pressure, which would in turn imply, respectively, an increase in drag or higher fuel consumption.

### 2.3.2 Final propulsion configuration

The ***Turbojet-Ramjet*** *combined cycle* in "Over-under" configuration with a **common variable-geometry intake** was selected as the most suitable option.

It should be noted that the choice to adopt a ramjet configuration is directly influenced by the design cruise speed of the vehicle, set at $Mach6$, which represents the upper operational limit for ramjet propulsion. Beyond this value, the efficiency of the ramjet decreases significantly due to a rapid decrease in both the specific impulse $I_{SP}$ and the thrust. For flight speeds exceeding Mach 6, a combined turbojet-scramjet propulsion system would provide better performance; however, such a configuration would be penalized at lower supersonic speeds, where the presence of the scramjet inlet results in a considerable additional drag.

The selected operational logic of the propulsion system varies with the flight Mach number as follows:

- **Mach 0 – 0.9:** only the turbojet is active, ensuring efficient performance in subsonic flight.
- **Mach 0.9 – 3.5:** the propulsion system operates with both the turbojet and ramjet active; in this regime, most of the incoming air is directed to the turbojet, while any surplus not required by the turbojet is routed to the ramjet.
- **Mach 3.5 – 6:** the turbojet is shut-down, the diverter is closed, and propulsion relies entirely on the ramjet, which provides improved efficiency at these velocities.

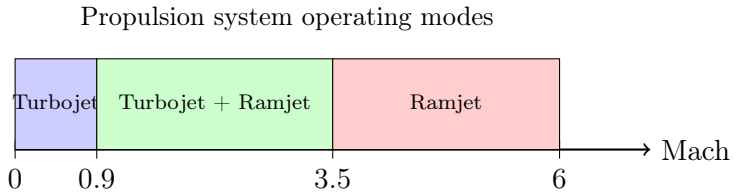


**Figure 2.18:** Operational logic of the *HYCAT-1* propulsion system as a function of Mach number.

# Chapter 3

# Mission Trajectory

The representative flight path for the high-speed vehicle operating from take-off through Mach 6 cruise to landing is inspired by the nominal flight path of the *HYCAT-1* [6] [3], considering operational limits such as dynamic pressure constraints and maximum altitude. The reconstruction of the flight profile is based on data extracted from a reference plot, shown in Figure 3.1, which provides a representation of the altitude variation with respect to the Mach number. The original plot was digitised and interpolated to obtain discrete altitude values corresponding to key Mach numbers during the climb and descent phases of the flight. These interpolated data points serve as the foundation for building the full aerodynamic trajectory profile.

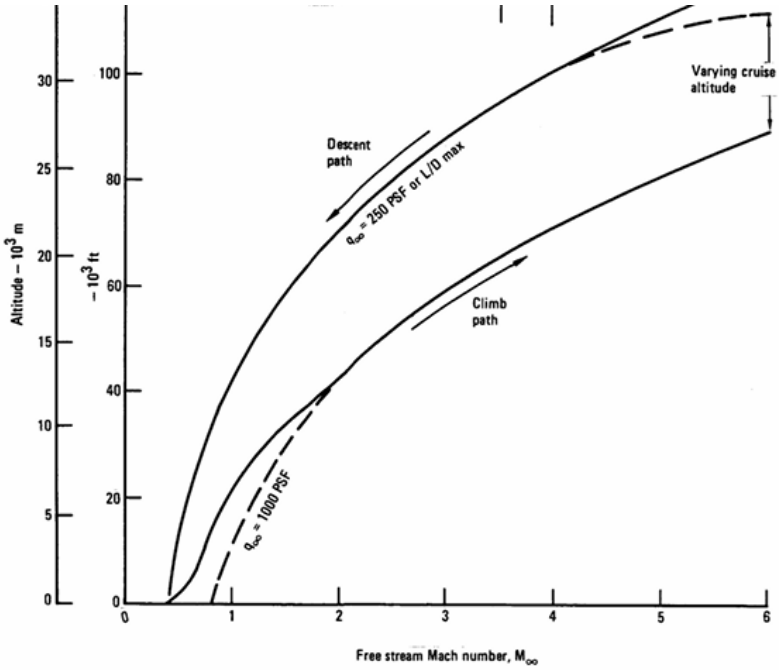


**Figure 3.1:** Nominal flight path [3]

## 3.1 Climb segment

The climb begins at sea level and proceeds to a maximum altitude of $28,600\,m$, reaching a final Mach number of 6.0. The climbing path is divided into **two regimes** based on dynamic pressure $q$:

- From take-off (Mach 0.35) to Mach 2.0, the vehicle follows a **variable dynamic pressure path**, with $q$ remaining below $47.88\,kPa$ $(1,000\,psf)$.
- From Mach 2.0 to Mach 6.0, the vehicle follows a **constant dynamic pressure path** of $47.88\,kPa$, which governs the relationship between the Mach number and the altitude through the equation:

$$q = \frac{1}{2}\rho(h) \cdot (M \cdot a(h))^2 \tag{3.1}$$

  where $\rho(h)$ is the atmospheric density and $a(h)$ is the local speed of sound at altitude $h$. The altitudes along this portion of the climb, for a given Mach number, were calculated by inverting this relationship and assuming the standard conditions defined by the *International Standard Atmosphere (ISA).*

During the climb phase, the aircraft was set to cover a total horizontal distance of $2,069km$, which is consistent with the mission reference data. To determine the distance travelled and the elapsed time, the trajectory was modelled on the basis of the available data, generating a series of points defined by Mach number and corresponding altitude.

Once these (Mach, Altitude) points were established, the local velocity at each point was computed as follows:

$$V = Mach \cdot a(h) \tag{3.2}$$

where the local speed of sound, $a(h)$, which varies with altitude, is determined using the *International Standard Atmosphere (ISA)* model, as detailed in the Appendix A.

The total time and horizontal distance were then obtained by integrating these velocities over the Mach increments along the climb profile.

## 3.2 Cruise segment

In typical high-speed missions, the cruise altitude is not strictly constant but exhibits a gradual increase. The reference source also reports this behaviour, providing a range of altitudes for the cruise phase. Specifically, the climb is defined to reach approximately $27,000\,m$, after which the cruise altitude increases progressively, reaching $28,600\,m$. For the purposes of this study and to simplify the trajectory modelling, it was assumed that the entire cruise phase occurred at a **fixed altitude** of $\mathbf{28,600\,m}$, with the climb extended up to the same level.

Once the climb and descent distances were established from the reference data, the cruise distance was proportionally adjusted to obtain a total mission range of $10,000\,km$, while preserving the relative durations and operational constraints of the climb and descent phases. The cruise segment was modelled at a fixed speed of Mach 6.0 over a horizontal distance of $6,790\,km$. The time of flight for this phase is computed directly from the cruise distance and velocity.

## 3.3 Descent segment

The descent phase begins at the end of the cruise segment, which occurs at a constant Mach number of 6.0 and an altitude of $28,600\,m$. This phase is characterised by a gradual reduction in both Mach number and altitude, and the trajectory is divided into **two main sub-phases**: a **Mach deceleration at constant altitude**, followed by a descent along a **constant dynamic pressure** path.

From the cruise condition at Mach 6.0 and $28,600\,m$ altitude, the vehicle must first reduce its velocity while maintaining its altitude. The Mach number is gradually reduced at constant altitude until a point is reached where the local dynamic pressure equals a prescribed limit, in this case $11.97\,kPa\,(250\,lbf/ft^2)$ that is reached when the Mach is approximately 4. Once the dynamic pressure constraint is reached, the vehicle begins a controlled descent along a path that maintains $q = 11.97\,kPa$. This constraint directly couples altitude and Mach number, requiring that as the vehicle slows further, the altitude must be reduced accordingly to maintain the specified aerodynamic loading.

The descent profile was constructed using interpolated data extracted from the same reference Mach–altitude diagram. This data set defines discrete Mach numbers from Mach 4.0 to 0.4, and the corresponding altitudes from $28,500\,m$ to approximately $460\,m$. These values were used to define the trajectory from the end of deceleration to near sea level. The total horizontal distance covered during descent was set to $1,141\,km$, based on mission reference data. Using the Mach number at each point and the corresponding local speed of sound (dependent on altitude), the local velocity was computed. This allowed for the calculation of both the segment durations and the cumulative time and distance.

## 3.4 Numerical implementation

The trajectory was modelled in *MATLAB* using a segmented logic for each flight phase. Based on the reference mission profile, a series of discrete waypoints were defined, each consisting of a Mach number and the corresponding Altitude.

For each segment between these waypoints during both **ascent and descent**, the following computational logic was applied:

- The **local speed of sound**, which is a function of temperature and thus altitude,

was computed using the *International Standard Atmosphere (ISA)* model.

- The **True Airspeed (TAS)** was then calculated as the product of the Mach number and the local speed of sound, as per equation 3.2.
- The segment distance was derived by discretising the total phase distance, and the corresponding **time interval** was calculated based on the average velocity of the segment ($dt = dx/v_{avg}$).

Conversely, the **cruise phase** was modelled as a steady-state segment at constant altitude and Mach number, where the total time is derived simply from the total cruise range and the constant flight velocity.

It is important to note that the waypoints were selected to strictly respect the dynamic pressure constraints of the reference vehicle. Specifically, for the constant-dynamic pressure phases, the corresponding altitude waypoints were derived analytically by inverting the dynamic pressure equation 3.1 for the target Mach numbers. This flight profile ensures that the dynamic pressure increases during the initial ascent and then stabilises, maintaining a consistent flight path up to the cruise condition.

To analyse and validate the mission trajectory, the resulting profiles are illustrated in the following figures, offering a full visualisation of the flight path dynamics. Complementing this visual overview, the detailed breakdown of each phase is presented in Table 3.1.

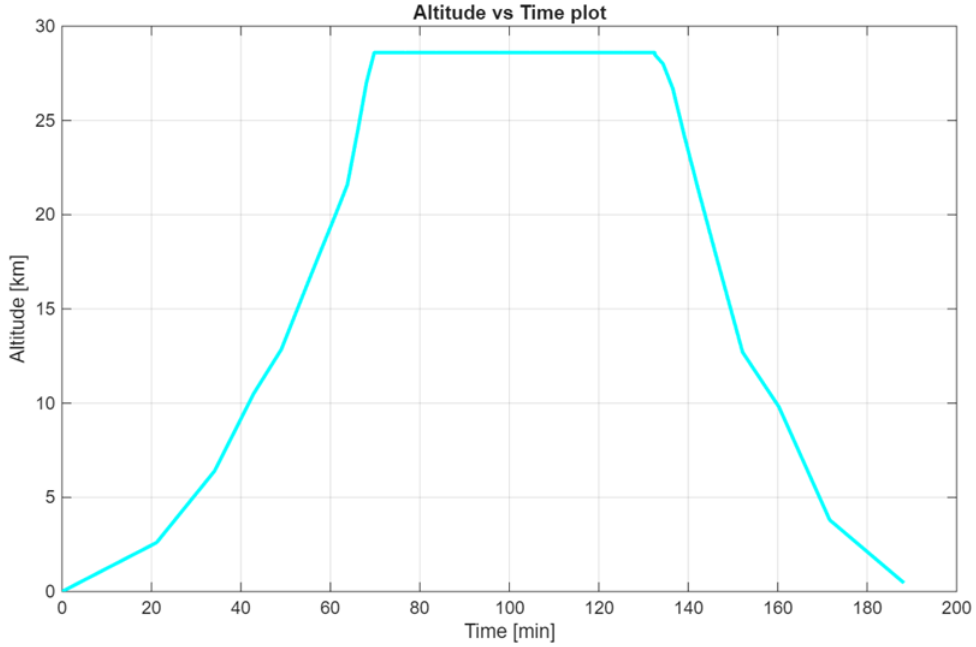


**(a)** Altitude over time

**Figure 3.2:** Reconstructed mission trajectory profiles.

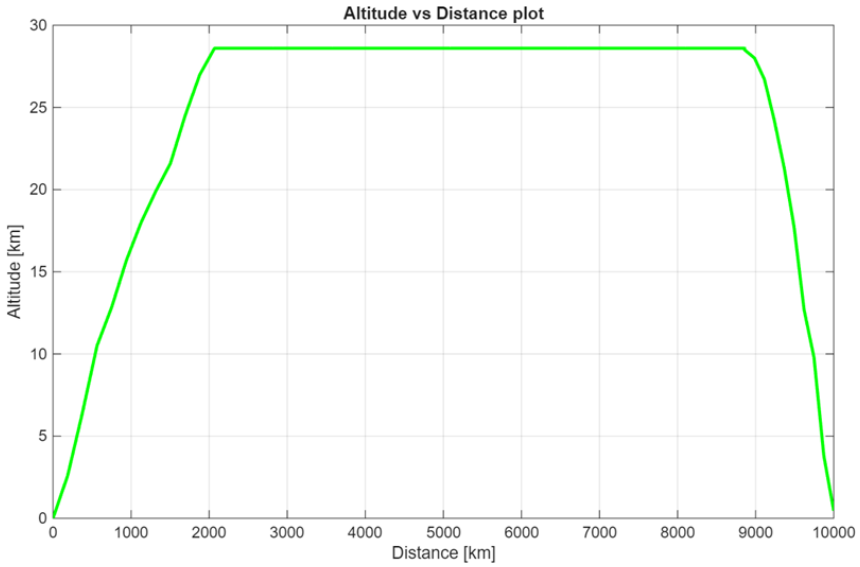


**(b)** Altitude over distance

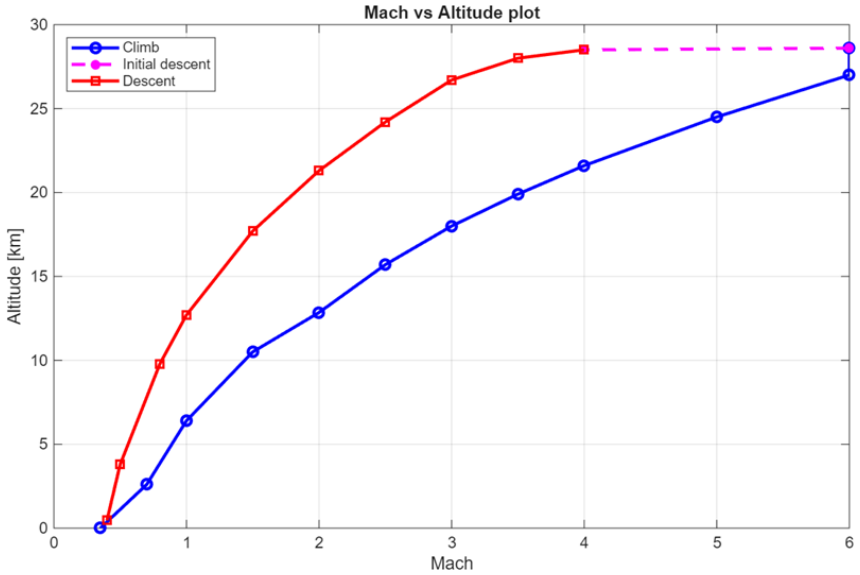


**(c)** Altitude over Mach

**Figure 3.2:** Reconstructed mission trajectory profiles (continued).

| **Phase** | **Horizontal Distance [km]** | **Approx. Time [min]** | **Key Constraint** |
|---|---|---|---|
| Climb | 2,069 | ∼69 | Variable $q \rightarrow$ Constant $q = 47.88$ kPa |
| Cruise | 6,790 | ∼63 | Mach 6.0 at 28.6 km |
| Descent | 1,141 | ∼56 | Constant $q = 11.97$ kPa $\rightarrow$ Final approach |
| **Total** | **10,000** | **∼188** | |

**Table 3.1:** Flight Phases with Distances and Times

# Chapter 4

# Preliminary Design Method

The sizing analysis model developed in this work is inspired by the ***HASA*** *'Hypersonic Aerospace Sizing Analysis'* methodology, originally developed by NASA in the 1990s for the preliminary design of advanced aerospace systems, Ref. [7]. This methodology was conceived to support the design of a wide variety of high-speed vehicles, including hypersonic transports and fighter aircraft, supersonic transport concepts, as well as single and two-stage-to-orbit configurations.

The strength of the *HASA* approach lies in its ability to provide reliable estimates of both **vehicle weight** and key **geometric characteristics** such as overall length, wingspan, fuselage diameter, and internal volume. Weight breakdowns are obtained by means of statistical correlations and semi-empirical equations applied to individual subsystems and components, including wings, fuselage, empennages, avionics, fuel tanks, propulsion system and structure, landing gear, electronic equipment, thermal protection system, and hydraulic systems.

Although this robust framework is adopted, the computational tool developed for this thesis introduces several **significant enhancements** to the original HASA model. First, the propulsion sizing logic has been refined to calculate the **total installed thrust** at each iteration as a function of the updated vehicle weight rather than treating it as a fixed input, thus maintaining a constant Thrust-to-Weight ratio ($T/W$). More importantly, the mission **fuel calculation** has been fundamentally redesigned, replacing the simple fixed fuel fraction with a more complex iterative logic. The fuel burn during cruise is not a static calculation, but is dynamically re-evaluated during each sizing iteration. This creates a crucial dependency: the required fuel (and thus its weight and volume) is related to the aerodynamic efficiency (L/D) of the aircraft, which in turn is recalculated based on the wetted area $S_{ref}$ and the volume of the fuselage $V_{tot}$, both of which change as the vehicle is resized.

Moreover, the methodology was extended to include the generation of a geometric sketch

(specifically a **planform view**) of the converged vehicle. This visual output allows for a direct inspection of the aircraft's layout and proportions, ensuring consistency with the numerical sizing results.

This improved methodology was selected because it retains the flexibility of *HASA*, allowing for variations in mission, propulsion architectures, and fuel types, while providing a much tighter integration between the vehicle's geometry, performance, and fuel requirements. This adaptability is central to the investigation of LNG as an alternative fuel.

The following sections present the calculation of the **fuel weight fractions** and the **computational tool developed** in *MATLAB*, which implements this enhanced methodology. The code is described in detail, with emphasis on the governing equations, the underlying assumptions, and the logic flow adopted to perform the sizing analysis.

## 4.1 Fuel weight fraction definition

A significant portion of the Maximum Take-Off Weight (MTOW) of an aircraft is due to the fuel required for the flight. The amount of fuel needed depends on the mission profile, the aerodynamic characteristics of the aircraft, and the specific fuel consumption of the engine (SFC). While the mission is usually predefined, the aerodynamic and propulsion parameters can be estimated during the conceptual design phase. A key goal in this context is to estimate the **fuel fraction**, defined as the ratio between fuel weight and take-off weight $\frac{W_f}{W_{TO}}$.

First, it is useful to clarify a convention common throughout aerospace engineering: the use of **weight** ($W$) instead of **mass** ($m$) for performance calculations. This is a standard practice simply because the main equations of aircraft performance are based on forces, where weight ($W = mg$) is the natural term for gravitational pull.

The entire fuel fraction analysis is built upon non-dimensional **weight fractions** like $W_{i+1}/W_i$. These are, by definition, numerically identical to the corresponding mass fractions, since the gravitational constant $g$ cancels out of the ratio. The convention of using weights is therefore adopted for consistency with the force-based performance equations used elsewhere in the work.

To calculate the total fuel required, the mission is broken down into several distinct **flight segments**, as shown in Figure 4.1. These phases cover the entire flight, including taxi, take-off, climb, cruise, descent, and landing. Each transition point between these segments is marked by a sequentially numbered aircraft weight. Following the notation in the figure, $\mathbf{W_1}$ is the weight at the start of take-off, $\mathbf{W_2}$ is the weight after take-off is complete, $\mathbf{W_3}$ marks the *Top of Climb (TOC)*, $\mathbf{W_4}$ is the weight just before starting the descent, and $\mathbf{W_5}$ is the weight right before the final landing.

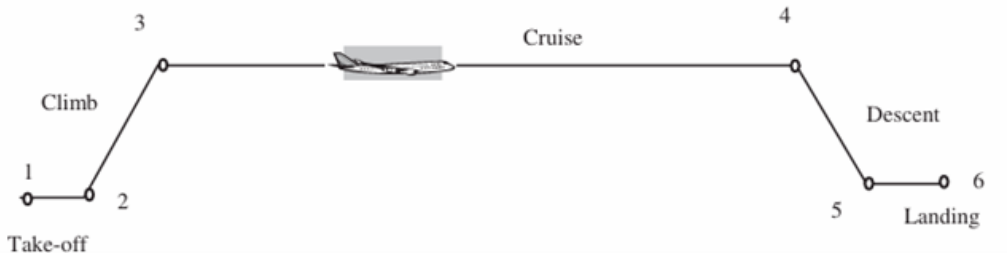


**Figure 4.1:** Typical mission profile segments

The ratio of the aircraft's weight at the end of a segment to its weight at the beginning is called the **segment weight fraction** $\frac{\mathbf{W_{i+1}}}{\mathbf{W_i}}$, for example, the fraction ($\frac{W_4}{W_3}$) represents fuel usage during the cruise. These fractions account for the fuel burnt during each phase. By multiplying all segment weight fractions, the total weight loss during the mission can be estimated, allowing the overall fuel fraction to be determined. The difference between the take-off weight and the final landing weight gives the total amount of fuel consumed:

$$W_f = W_{TO} - W_{landing} \tag{4.1}$$

To ensure flight safety, it is standard practice to include reserve fuel in case the intended destination is unavailable, such as when an airport is unexpectedly closed, requiring the aircraft to divert to an alternate location. This additional safety fuel typically accounts for approximately 5 % of the total weight of the aircraft. Consequently, this reserve is factored into the calculation of the total fuel weight fraction, which can then be expressed as follows:

$$\frac{W_f}{W_{TO}} = 1.05 \cdot (1 - \frac{W_{landing}}{W_{TO}}) \tag{4.2}$$

The final weight in relation to the take-off weight can be calculated as a product of the fractions of the individual segments of the mission:

$$\frac{W_{landing}}{W_{TO}} = \frac{W_6}{W_1} = \prod_{i=1}^{n} \frac{W_{i+1}}{W_i} \tag{4.3}$$

To calculate the total fuel weight fraction, it is first necessary to estimate the weight fractions associated with each phase of the flight. These segments can generally be grouped on the basis of the relative amount of fuel consumed.

### 4.1.1 Empirical fractions (fixed segments)

Phases such as taxi, take-off, climb, descent, approach, and landing consume relatively little fuel compared to the Maximum Take Off Weight of the aircraft. Furthermore, these segments follow **standardised operational procedures**, meaning their duration and energy requirements remain effectively constant regardless of the specific mission range.

For these, fuel weight fractions are typically derived from statistical data, table 4.1 provides the average values commonly used for conventional kerosene powered aircraft (Ref [8]).

| No. | Mission segment | $(W_{i+1}/W_i)_{kerosene}$ |
|---|---|---|
| 1 | Taxi and take-off | 0.97 |
| 2 | Climb | 0.88 |
| 4 | Descent | 0.985 |
| 5 | Approach and landing | 0.995 |

**Table 4.1:** Fuel weight fractions of mission segments

For an aircraft powered by **liquid methane**, the corresponding weight ratios will be slightly closer to unity because of the favourable properties of the fuel. Specifically, liquid methane has a specific energy density approximately 1.25 times higher than that of conventional kerosene. Taking this into account, an adjusted formula was derived to reflect the improved fuel efficiency:

$$(\frac{W_{i+1}}{W_i})_{LNG} = 1 - \frac{1 - (\frac{W_{i+1}}{W_i})_{kerosene}}{1.25} \tag{4.4}$$

where $1-(\frac{W_{i+1}}{W_i})_{kerosene} = (\frac{W_{fuel,i}}{W_i})_{kerosene}$ represents the ratio of the fuel weight consumed during phase '$i$' to the total weight of the aircraft at the beginning of that segment.

Using this expression, the weight fractions for each phase of a methane-fueled aircraft have been calculated and are presented in the following table 4.2.

| **No.** | **Mission segment** | $(W_{i+1}/W_i)_{LNG}$ |
|---|---|---|
| 1 | Taxi and take-off | 0.976 |
| 2 | Climb | 0.904 |
| 4 | Descent | 0.988 |
| 5 | Approach and landing | 0.996 |

**Table 4.2:** Fuel weight fractions of mission segments for the LNG-powered aircraft

### 4.1.2 Analytical fraction (cruise segment)

The simplified empirical estimates used for segments such as take-off and landing are a valid simplification, as these phases are generally short, repeatable, and account for a minor portion of the total fuel. However, this methodology cannot be applied to the **cruise segment**, as the cruise is responsible for the vast majority of the mission fuel consumption and, more importantly, its duration is not fixed.

Instead, the fuel fraction of the cruise must be determined analytically. This distinction is critical because the **cruise range** is the primary **variable** that defines a specific mission profile, whereas the other phases are generally assumed to be constant.

The fuel weight fraction for the cruise segment is calculated using the *Breguet range equation*, which assumes flight at a constant airspeed and a constant lift coefficient. This approach enables a more accurate estimate of fuel consumption during the cruise, where fuel burn is the most significant.

$$\textbf{Breguet Equation :} \qquad \frac{W_4}{W_3} = e^{-\frac{R}{I_{SP} \cdot V \cdot \frac{L}{D}_{cruise}}} \tag{4.5}$$

- The range '**R**' represents the total distance covered during the cruise phase. In this study, it has been fixed at $6,790 km$, based on the predefined mission profile described earlier.

- The specific impulse '$\mathbf{I_{SP}}$', measured in seconds, is an indicator of engine efficiency and varies depending on the number of Mach of the flight and the propulsion system used. In this study, a combined **turbojet — ramjet** configuration is considered; however, during cruise at Mach 6, only the ramjet operates. In the reference literature, specifically Ref. [6], a specific impulse ($I_{SP}$) of $3,008\,s$ is reported for a turbojet – ramjet propulsion system operating with liquid hydrogen during cruise. The specific impulse of a propulsion system is directly related to the velocity of the exhaust gas, which in turn depends on the energy content of the fuel. Fuels with a higher energy density per unit mass generally produce higher exhaust velocities, increasing thus $I_{SP}$.

  Taking kerosene as fuel, the corresponding value of the specific impulse is approximately $1,074\ s$. Switching to liquid methane, whose specific energy is approximately 25 % higher than that of kerosene, results in an estimated specific impulse of $\mathbf{I_{SP,LNG}} = 1.25 \cdot I_{SP,kerosene} = \mathbf{1,343}\,\mathrm{s}$.

- The cruise velocity '**V**', expressed in meters per second, can be directly calculated, since both the cruise altitude and the cruise Mach number are known. Given that the Mach number represents the ratio between the speed of the aircraft and the speed of sound in the surrounding medium, the velocity can be obtained using the following relation:

  $$V_{cruise} = M_{cruise} \cdot a(h_{cruise})$$

  where $M$ is the Mach number and $a$ is the speed of sound at the cruise altitude. The value of $a$ can be directly determined from the standard atmosphere model (ISA) at the specified altitude.

- The Lift-to-Drag ratio '**L/D**' represents the aerodynamic efficiency of the aircraft during cruise. For hypersonic aircraft, typical Lift-to-Drag (L/D) ratios are restricted to the **2 − 8 range**. This is considerably lower than the efficiencies achieved by conventional aircraft, a limitation driven by dominant aerodynamic phenomena such as shock-induced wave drag and severe skin friction at high Mach numbers. The lift-to-drag ratio can be expressed as a function of the Mach number and the geometry

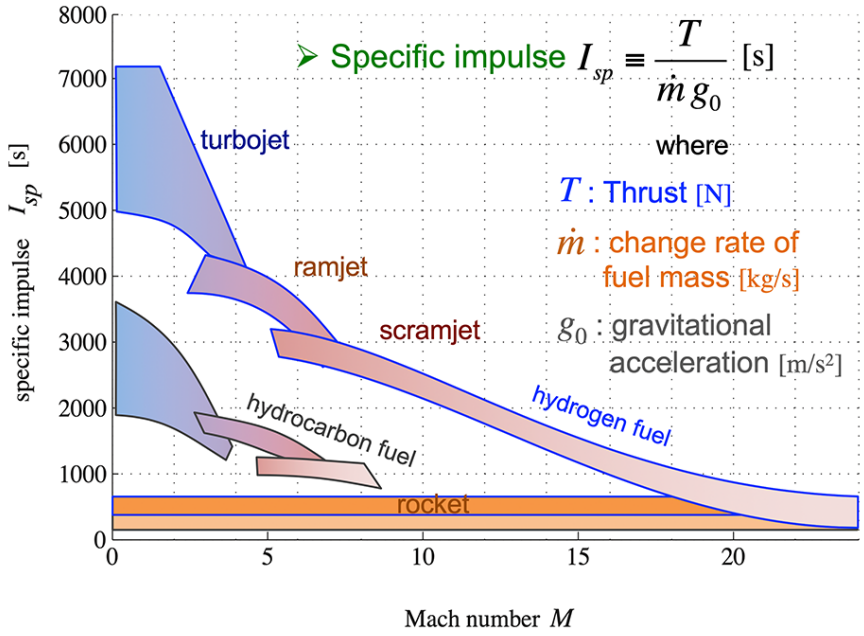


**Figure 4.2:** Specific Impulse

of the aircraft using the parameter $\tau$, known as the **Küchemann parameter** [9], defined as:

$$\tau = \frac{V_{tot}}{S_{ref}^{1.5}} \tag{4.6}$$

where $V_{tot}$ is the total volume of the aircraft and $S_{ref}$ is the reference area of the wing.

Using this parameter, the ratio $(L/D)$ can be expressed using the following empirical formula:

$$\frac{L}{D} = \frac{A(M+B)}{M} \left[ \frac{1.0128 - 0.2797 \cdot \log\left(\frac{\tau}{0.03}\right)}{1 - \frac{M^2}{673}} \right] \tag{4.7}$$

where $A$ and $B$ are two coefficients with values of 6 and 2, respectively. This expression captures the influence of both the flight regime, through the Mach number $M$, and the aircraft configuration, through $\tau$, on aerodynamic performance during cruise.

## 4.2 Vehicle input parameters

To begin the sizing process, the vehicle model requires a specific set of input parameters. For practical flexibility, these values are not hard-coded as constants within the *MATLAB* script. Instead, they are managed in an external Excel file, allowing the data to be easily inspected, modified, and managed without requiring direct alterations to the source code.

The first step of the programme involves loading this data set. A uniform nomenclature has been adopted, ensuring a direct correspondence between the variable names in the Excel file and the internal structures used by the code. This consistent naming scheme facilitates the tracking of any parameter from its initial definition through to its final converged value.

### 4.2.1 Nomenclature

| | |
|---|---|
| $A_{hfp}$ | Ratio between the horizontal stabilizer area and the wing area |
| $A_{vfp}$ | Ratio between the vertical stabilizer area and the wing area |
| $A_{lorb}$ | Ratio of the body cylinder length to the body radius |
| $AR$ | Wing aspect ratio |
| $B_b$ | Body width $[m]$ |
| $C_{root}$ | Chord at root $[m]$ |
| $D_{be}$ | Equivalent body diameter $[m]$ |
| $F_r$ | Body fineness ratio = $L/D$ equivalent |
| $Fuel_{frac}$ | Fuel weight fraction $W_{prop}/W_{gtot}$ |
| $H_{tsjm}$ | Height of scramjet module $[m]$ |
| $ISP$ | Specific impulse $[s]$ |
| $k_b$ | Length calibration constant |
| $k_c$ | Calibration coefficient for non-idealized body |
| $k_n$ | Ratio of body depth to body width |
| $L_b$ | Total body length $[m]$ |
| $mf$ | Modifying factor |
| $N_{engsj}$ | Number of scramjet modules |
| $N_{engtj}$ | Number of turbojet engines |
| $N_{engtr}$ | Number of turboramjet engines |
| $Q_{max}$ | Maximum dynamic pressure $[kg/m^2]$ |
| $S_{btot}$ | Body wetted surface area $[m^2]$ |
| $S_{ref}$ | Reference wing area $[m^2]$ |
| $S_{tb}$ | One half body wetted surface area $[m^2]$ |
| $S_{wfh}$ | Horizontal stabilizer planform area $[m^2]$ |
| $S_{wfv}$ | Vertical stabilizer planform area $[m^2]$ |
| $t/c$ | Wing thickness to chord ratio |
| $T_{tott}$ | Total momentum thrust of all airbreathing engines $[N]$ |
| $T/W$ | Thrust to Weight ratio |

| | |
|---|---|
| $ULF$ | Ultimate load factor |
| $V_{af}$ | Volume of air factory $[m^3]$ |
| $V_{fuel}$ | Volume of propellant $[m^3]$ |
| $V_{pay}$ | Volume of payload $[m^3]$ |
| $V_{tot}$ | Total vehicle volume $[m^3]$ |
| $W_a$ | Engine airflow $[kg/s]$ |
| $W_b$ | Weight of body structure $[kg]$ |
| $W_{elect}$ | Weight of electronics $[kg]$ |
| $W_{emp}$ | Vehicle empty weight $[kg]$ (dry) |
| $W_{eng}$ | Total engine weight $[kg]$ |
| $W_{equip}$ | Weight of onboard equipment $[kg]$ |
| $W_{finh}$ | Weight of horizontal stabilizer $[kg]$ |
| $W_{finv}$ | Weight of vertical stabilizer $[kg]$ |
| $W_{fuel}$ | Total weight of propellant $[kg]$ |
| $W_{gear}$ | Weight of landing gear $[kg]$ |
| $W_{gtot}$ | Total vehicle gross weight $[kg]$ |
| $W_{H2}$ | Weight of hydrogen to take-off gross weight |
| $W_{hydr}$ | Weight of hydraulics $[kg]$ |
| $W_{ins}$ | Unit weight of thermal protection system $[kg/m^2]$ |
| $W_{pay}$ | Weight of payload $[kg]$ |
| $W_{pros}$ | Total weight of propulsion system $[kg]$ |
| $W_{load}$ | Wing loading $[kg/m^2]$ |
| $W_{span}$ | Wingspan $[m]$ |
| $W_{str}$ | Total weight of structural system $[kg]$ |
| $W_{sub}$ | Total weight of subsystems $[kg]$ |
| $W_{taves}$ | Weight of avionics $[kg]$ |
| $W_{thrst}$ | Total weight of thrust structure $[kg]$ |
| $W_{thrua}$ | Weight of airbreathing thrust structure $[kg]$ |
| $W_{tnk}$ | Total weight of propellant tanks $[kg]$ |
| $W_{tps}$ | Weight of thermal protection system $[kg]$ |
| $W_{trj}$ | Weight of ramjet engines $[kg]$ |
| $W_{tsj}$ | Weight of scramjet engines $[kg]$ |
| $W_{ttj}$ | Weight of turbojet engines $[kg]$ |
| $W_{ttr}$ | Weight of turboramjet engines $[kg]$ |
| $W_w$ | Weight of wing structure $[kg]$ |
| $\delta$ | Percentage of fuel stored in the fuselage |
| $\lambda$ | Wing taper ratio |
| $\lambda_{1/2}$ | Mid-chord sweep angle $[deg]$ |
| $\eta_{vol}$ | Vehicle volumetric efficiency |
| $\rho_a$ | Vehicle density $[kg/m^3]$ |
| $\rho_{fuel}$ | Fuel density $[kg/m^3]$ |

| | |
|---|---|
| $\rho_{tank}$ | Density of propellant tank $[kg/m^3]$ |
| $w_{pass}$ | Payload weight per passenger $[kg]$ |
| $\rho_{pay}$ | Payload density $W_{pay}/V_{pay}$ $[kg/m^3]$ |
| $\theta_f$ | Fore cone half angle $[deg]$ |
| $\theta_r$ | Aft cone half angle $[deg]$ |
| $\tau$ | Küchemann parameter |

### 4.2.2 Input list

This list of parameters contains all values required to initialise the code and execute the first iteration. It serves as a summary description of the reference vehicle configuration.

The input data are managed in an external *Excel file* which includes **two distinct configurations**:

- one for the **Liquid Methane (LNG)** powered vehicle;
- another for the **Liquid Hydrogen ($LH_2$)** configuration.

The $LH_2$ model, while based on the original HASA work, has been adapted to meet the specific requirements of the mission and refined for this study, particularly in the iterative fuel calculation where the aerodynamic efficiency, inherently dependent on the fuselage configuration, is re-evaluated during each sizing cycle. Both configurations share the same geometry and mission requirements but differ in their fuel-dependent parameters, such as density and specific impulse.

As shown in Figure 4.4, the structure of the file is as follows: the first column of the Excel file contains the variable names along with their corresponding units, separated by a comma. Units are included for clarity, but the code automatically filters them out during execution, retaining only the names of the variables. The subsequent columns list the values of these parameters for each reference vehicle, identified by the header in the first row, which is the name of the vehicle.

All values contained in this file are expressed in the *Imperial System of Units*. This choice is necessary because the empirical, non-linear relations employed in the design model were originally developed using Imperial units and would not be directly applicable to values expressed in the *International System of Units* (SI). To maintain consistency, all calculations are therefore carried out entirely in Imperial units. Only at the final stage of the code are all parameters converted into SI units, ensuring that the results are presented in a standardised and widely accepted format.

Once the program is launched, the user is prompted to select the desired reference vehicle, as shown in Fig. 4.3, and the code automatically extracts the corresponding data set from the appropriate column.

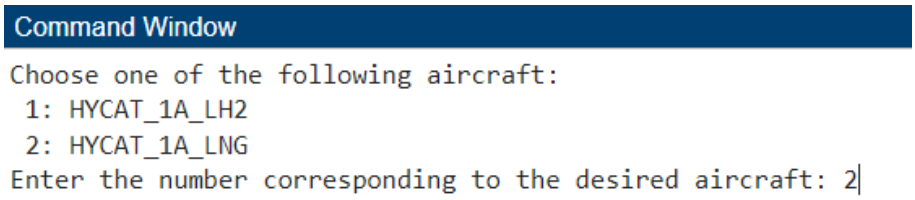


**Figure 4.3:** Selection of the reference vehicle

| INPUT_LIST | HYCAT_1A_LH2 | HYCAT_1A_LNG |
|---|---|---|
| Range, km | 10000 | 10000 |
| Passengers | 200 | 200 |
| w_pass, lb/pass | 210 | 210 |
| rho_pay, lb/ft3 | 3,03030303 | 3,03030303 |
| A_hfp | 0,1366 | 0,1366 |
| A_vfp | 0,1125 | 0,1125 |
| A_lorb | 8,65 | 8,65 |
| AR | 1,357 | 1,357 |
| C_root, ft | 90 | 90 |
| F_r, ft | 14,1 | 14,1 |
| lambda_mezzi, deg | 40 | 40 |
| theta_f, deg | 4,04 | 4,04 |
| theta_r, deg | 10,48 | 10,48 |
| t/c | 0,03 | 0,03 |
| lambda | 0,154 | 0,154 |
| Wing_load | 86 | 86 |
| L_b, ft | 344,9 | 344,9 |
| D_be,ft | 24,46 | 24,46 |
| Sb_tot, ft2 | 21997 | 21997 |
| W_span, ft | 96,2 | 96,2 |
| eta_vol | 0,7 | 0,7 |
| H_tsjm, in | 0 | 0 |
| N_engsj | 0 | 0 |
| N_engtj | 4 | 4 |
| N_engrj | 4 | 4 |
| N_engtr | 0 | 0 |
| T_tott, lb | 306000 | 306000 |
| W_a, lb/sec | 551 | 551 |
| rho_a, lb/ft3 | 7 | 7 |
| rho_fuel, lb/ft3 | 5,25 | 28 |
| rho_tnk, lb/ft3 | 1,75 | 1,75 |
| Q_max, lb/ft2 | 1000 | 1000 |
| W_ins, lb/ft2 | 1,5 | 1,5 |
| ULF | 3,75 | 3,75 |
| mf | 1,12 | 1,12 |
| delta | 1 | 1 |
| W_gtot, lb | 613174 | 613174 |
| V_tot, ft3 | 91434 | 91434 |
| Mach | 6 | 6 |
| T_W | 0,48 | 0,48 |
| ISP, s | 3008 | 1343 |

**Figure 4.4:** Input list

## 4.3 Sizing and weighting analysis

The computational model relies on a robust **fixed-point iterative strategy**. This approach is essential to address the strong mutual dependence between the vehicle's geometry and its mass properties. In each calculation cycle, the vehicle undergoes an initial geometric sizing step to establish key parameters such as fuselage length, equivalent diameter, wetted area, and total internal volume. Once the geometry is defined, a comprehensive weight analysis is performed. The resulting weight estimates are then fed back into the loop as the input for the subsequent iteration, ensuring that the design progressively converges toward a consistent solution where the estimated structural weight perfectly matches the required geometric volume.

To ensure numerical stability and physical consistency, the algorithm is structured into four sequential phases:

1. **Data Import and Initialisation:** The process starts by loading the reference vehicle database. Using these inputs, the code performs an initial mass breakdown to establish the baseline Gross Weight ($W_{G,tot}^{(1)}$) and the Total Volume ($V_{tot}^{(1)}$).
2. **Initial Calibration:** Using these initialised values alongside the reference geometry, the code calculates the first set of calibration constants ($k_n, k_b, k_c$). This crucial step aligns the empirical dimensioning equations with the specific architecture of the reference vehicle.
3. **Preliminary Sizing Cycle:** A complete sizing and weighting analysis is executed using the newly calibrated constants. This step generates a refined estimate of the vehicle's weight ($W_{G,tot}^{(2)}$), establishing the necessary baseline value required to initialise the convergence check.
4. **Iterative Convergence Loop:** Subsequently, the algorithm enters the main loop. At each step, the convergence condition

$$|W_{G,tot}^{(i)} - W_{G,tot}^{(i-1)}| < \epsilon$$

is verified. If the tolerance ($\epsilon = 10\ lb$) is not met, the calibration constants are updated based on the current geometry, and the sizing cycle is repeated until stability is achieved.

The general architecture of the code, which illustrates this sequential relationship, is schematically represented in Figure 4.5.

### 4.3.1 Geometry definition and calibration strategy

The geometric sizing of the vehicle relies on a set of semi-empirical correlations. To ensure that these correlations accurately represent the shape of the baseline hypersonic architec-

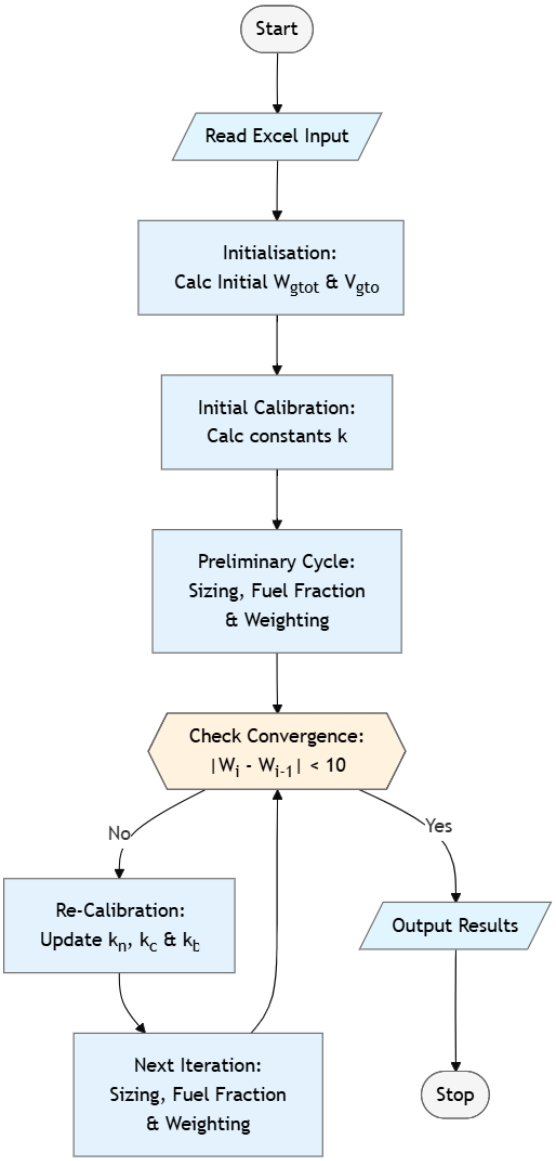


**Figure 4.5:** Flowchart

ture, three dimensionless **calibration constants** are introduced: $k_n$, $k_b$, $k_c$.

These constants are mathematically derived as functions of idealised geometric inputs such as the half-angles of the fore body ($\theta_f$) and the aft body ($\theta_r$), as well as the parameter $A_{lorb}$ defined as the ratio of the length of the cylindrical portion of the fuselage to the body radius.

Crucially, these constants also depend on the vehicle's total internal volume ($V_{tot}$), equivalent diameter ($D_{be}$), and body length ($L_b$). This creates a **circular dependency**, since these geometric variables are themselves the result of the sizing process. To resolve this, the process is initialised using the known database of the reference vehicle. These preliminary values allow for the **first evaluation** of the calibration constants, which is the prerequisite step to "tune" the geometric model before entering the main iterative loop.

### Calibration Constants

The calibration constants serve as **shape factors** that constrain the geometric scaling. They are expressed through the following relations:

$$k_n = D_{be} \cdot \left( \frac{2\pi \left( \frac{1}{6\tan(\theta_f)} + \frac{A_{lorb}}{2} + \frac{1}{6\tan(\theta_r)} \right)}{V_{tot}} \right)^{\frac{1}{3}} - 1 \tag{4.8}$$

where $\mathbf{k_n}$ is the ratio between depth and width.

$$k_c = \frac{2D_{be}^2}{(1+k_n)^2 \cdot 3.309\sqrt{L_b V_{tot}}} \left( \frac{\pi}{2\sin(\theta_f)} + \pi A_{lorb} + \frac{\pi}{2\sin(\theta_r)} \right) \tag{4.9}$$

where $\mathbf{k_c}$ is the calibration coefficient for a non-idealised shape.

$$k_b = \frac{D_{be}}{1+k_n} \cdot \left( \frac{1}{\tan(\theta_f)} + A_{lorb} + \frac{1}{\tan(\theta_r)} \right) \cdot \frac{1}{L_b} \tag{4.10}$$

where $\mathbf{k_b}$ is a length calibration constant.

These expressions guarantee that the geometric evolution of the vehicle remains consistent with the aerodynamic requirements. By updating these constants at the start of each iteration using the last values, the code ensures that the fuselage stretches or widens proportionally, preserving the fundamental shape characteristics of the reference configuration.

### Geometric Parameters

Once the three constants have been determined, they can be applied to compute the geometric characteristics of the vehicle for the next iteration. This step updates parameters such as the wetted area, length, and diameter, thus providing the refined inputs required for the subsequent weight analysis. The following set of **five equations** serves as the basis for defining the geometry of the vehicle.

Total **wetted area** of the body:

$$S_{btot} = 3.309\, k_c \sqrt{L_b V_{tot}} \tag{4.11}$$

Total **length** of the vehicle:

$$L_b = k_b \left( \frac{F_r^2 V_{tot}}{\frac{\pi}{4}\eta_{vol}} \right)^{\frac{1}{3}} \tag{4.12}$$

Body equivalent **diameter**:

$$D_{be} = \sqrt{\frac{V_{tot}}{L_b \frac{\pi}{4} \eta_{vol}}} \tag{4.13}$$

**Fineness ratio** equation:

$$F_r = \frac{L_b}{D_{be}} \tag{4.14}$$

Body **width** equation:

$$B_b = \frac{2D_{be}}{1 + k_n} \tag{4.15}$$

The **volumetric efficiency** $\eta_{vol}$ is an input parameter of the vehicle model and is typically assumed to be around 0.7. In the first iteration, the guess value of the **total internal volume** $V_{tot}$ is used. The output values obtained from the analysis are then fed back as input for the subsequent iteration, and the process is repeated until convergence is reached.

### 4.3.2 Weights analysis

As discussed previously, the weight analysis model employs the iterative methodology described earlier: once the vehicle has been sized, its weight is estimated. The aircraft is decomposed into individual **subsystems**, each of which is associated with a dedicated weight equation. These equations account for the contributions of propellant, fuselage, wing, horizontal and vertical stabilizers, thrust structure, propellant tanks, landing gear, propulsion system, thermal protection system, avionics, hydraulics, electronics, and onboard equipment.

It should be emphasised that all equations have been derived using **weights expressed in pounds**; therefore, the corresponding constants are valid only within this unit system.

#### Fuel weight

The total fuel weight can be easily determined. As presented in the previous chapter 4.1, the methodology to derive the overall **fuel fraction** of the mission has already been established. Once this fraction is known, the total required fuel weight is simply the product of this mission fraction and the total gross weight of the aircraft.

$$W_{fuel} = Fuel_{frac} \cdot W_{gtot} \tag{4.16}$$

#### Payload weight and volume

The total payload is defined by two key input parameters, both expressed on a per-passenger basis. These values are derived from standard reference aircraft data tables. The first parameter is the **equivalent passenger weight** ($w_{pass}$), which represents the

average weight of the passenger plus their baggage. The second is the **equivalent passenger volume** ($\rho_{pass}$), which represents the total average cabin and cargo hold volume assigned to each passenger. Once these inputs are known, the total payload weight and total payload volume are easily determined as functions of the **design number of passengers**:

$$W_{pay} = N_{pass} \cdot w_{pass} \tag{4.17}$$

$$V_{pay} = N_{pass} \cdot \rho_{pay} \tag{4.18}$$

### Body weight

The weight of the body does not include systems, propellant tanks, or engines, but only represents the major structural components of the fuselage. The formulation, adapted from [10], includes a key parameter called **modifying factor ($m_f$)**. The purpose of this factor is to adjust the calculation for different structural materials; for example, to account for the weight difference between a standard aluminium baseline and a titanium structure. This factor is a function of the structural temperature of the material.

The equation is as follows:

$$W_b = 0.341 \cdot mf \left( \left( \frac{L_b \cdot ULF}{D_{be}} \right)^{0.15} \cdot Q_{max}^{0.16} \cdot S_{btot}^{1.05} \right) \tag{4.19}$$

### Wing weight

The wing weight ($W_w$) represents the weight of the primary wing structure itself, its support structure, and the associated aerodynamic control surfaces. The formulation used to estimate this weight, adapted from the reference manual [11], incorporates design parameters such as the aspect ratio and the taper ratio to accurately characterise the planform geometry of the wing.

Before presenting the equation, two key component terms must be defined. First, the **empty weight ($W_{emp}$)** used in this context is defined as:

$$W_{emp} = W_{gtot} - W_{fuel} \tag{4.20}$$

where $W_{gtot}$ is the gross weight and $W_{fuel}$ is the total fuel weight.

Second, the parameter $\delta$ is introduced to define the fuel allocation between the wing and the fuselage:

- If $\delta = 1$, it is assumed that all fuel is stored within the fuselage.

- If $\delta = 0$, the fuel is stored in integral wing tanks.

The resulting equation is as follows:

$$W_w = 0.2958 \cdot mf \cdot \left[ \left( \frac{(W_{emp} - (1-\delta) \cdot W_{tnk}) \cdot ULF}{1000} \right)^{0.52} \cdot S_{ref}^{0.7} \cdot AR^{0.47} \cdot \left( \frac{1+\lambda}{t/c} \right)^{0.4} \cdot \left( 0.3 + \frac{0.7}{\cos(\Lambda_{1/2})} \right) \right]^{1.017} \tag{4.21}$$

The use of the term $(W_{emp} - (1-\delta) \cdot W_{tnk})$ is a crucial correction. If the tanks are in the fuselage ($\delta = 1$), this term simply resolves to $W_{emp}$. However, if integral wing tanks are used ($\delta = 0$), the term becomes $W_{emp} - W_{tnk}$. This subtraction is necessary to avoid double-counting. Since the integral tank weight is physically located within the wing, it must be removed from the definition of the empty weight used in equation 4.21 to ensure that the total structural weight is estimated correctly.

### Tail stabilizers

The equations used for the weight estimation of both tail surfaces are derived from [10]. The areas of the tail surfaces $S_{wfh}$ and $S_{wfv}$ are obtained through their respective coefficients $A_{hfp}$ and $A_{vfp}$, which represent the ratio of each tail surface area to the wing reference area.

For the **horizontal stabilizer**, the weight is estimated as:

$$W_{finh} = 0.0035 \cdot \left( \left( \frac{W_{gtot}}{S_{ref}} \right)^{0.6} \cdot (S_{wfh})^{1.2} \cdot (Q_{max})^{0.8} \right) \tag{4.22}$$

The weight of the **vertical stabilizer** is calculated using the following expression:

$$W_{finv} = 5 \cdot S_{wfv}^{1.09} \tag{4.23}$$

### Thermal protection system

The thermal protection system (TPS) is modelled as covering a surface equal to the combination of the wing planform area $S_{ref}$, the horizontal tail planform area $S_{wfh}$, and half of the body wetted surface area $S_{tb}$. An average areal density ($W_{ins}$) is applied to the entire area requiring thermal protection.

From this, the total weight of the TPS is obtained as:

$$W_{tps} = W_{ins} \cdot (S_{tb} + S_{ref} + S_{wfh}) \tag{4.24}$$

### Landing gear

The weight of the landing gear represents the combined weight of the nose gear, the main gear, and their associated control systems. The formulation, adapted from [10], estimates this component directly as a function of the vehicle's total gross weight using the following relation:

$$W_{gear} = 0.00916 \cdot W_{gtot}^{1.124} \tag{4.25}$$

### Thrust structure

The weight of the thrust structure, which means the supports of the engines, depends on the total momentum thrust. The equation for air breathing engines, derived from [10], is:

$$W_{thrua} = 0.00625 \cdot T_{tott} + 69 \tag{4.26}$$

In the original HASA model, the **total installed thrust** is treated as a fixed constant determined by the initial input. However, since the vehicle's gross weight changes during the sizing iterations, maintaining a static thrust value leads to physical inconsistencies (i.e., a varying $T/W$ ratio). To address this, the logic was modified to treat total thrust as a **dynamic variable**. Instead of directly fixing the thrust, an optimal **Thrust-to-Weight at lift-off** ($T/W_{LO}$) is defined in the input parameters file, based on values retrieved from Ref. [6]. Consequently, the code recalculates the total thrust required at each iteration as a function of the updated weight of the vehicle ($T_{tott} = (T/W)_{LO} \cdot W_{gtot}$), ensuring that the propulsion sizing remains consistent with the aircraft's dimension as it converges.

### Total structural weight

The structural weight of the vehicle is obtained by summing the contributions of the body, wings, tail surfaces, thermal protection system, landing gear, and thrust support structure:

$$W_{str} = W_b + W_w + W_{finh} + W_{finv} + W_{tps} + W_{gear} + W_{trua} \tag{4.27}$$

### Engine

Hypersonic vehicles fundamentally rely on multi-mode propulsion systems, already discussed in section 2.3, to handle distinct speed regimes, and for this reason, the methodology was structured to include a wider variety of air-breathing engine options. Although this specific study focusses on a combined turbojet–ramjet configuration, the code was designed to preserve the generality of the original *HASA* tool, including four types of engine: turbojets, turboramjets, ramjets, and scramjets.

The formulation used to estimate the **turbojet** engine weight equation relies on the formulation presented in [12]:

$$W_{ttj} = \frac{N_{eng} \cdot (W_a \cdot 133.3 - 16600)}{4} \tag{4.28}$$

To estimate the **turboramjet** weight equation, the correlation proposed by [10] was adopted:

$$W_{ttr} = 1782.63 \cdot N_{engtr} \cdot e^{0.003 \cdot W_a} \tag{4.29}$$

The weight estimation for the **ramjet** engine system is not based on the number of engines. Instead, it is calculated as a function of the total required thrust expressed in lbf through the formulation shown in eq. 4.30, derived from [10]. In this expression, the coefficient **0.01** serves as the conversion factor from thrust to weight. This specific value was selected as it represents the typical weight-to-thrust ratio of a **low-volume ramjet** architecture.

$$W_{trj} = 0.01 \cdot T_{tott} \tag{4.30}$$

The **scramjet** weight equation, taken from [13], is expressed as a function of the module height ($H_{tsjm}$):

$$W_{tsj} = N_{engsj} \cdot (87.5 \cdot H_{tsjm} - 850) \tag{4.31}$$

### Tank

The weight of the tank is assumed to scale proportionally with the required volume. This component is calculated directly using the parameter $\rho_{tank}$, defined as the structural weight of the tank per unit volume of onboard fuel, using the following expression:

$$W_{tnk} = V_{fuel} \cdot \rho_{tnk} = \frac{W_{fuel}}{\rho_{fuel}} \cdot \rho_{tnk} \tag{4.32}$$

For cryogenic propellants such as hydrogen or methane, **integral tanks** embedded within the vehicle structure are considered. In this analysis, the weight of the thermal insulation required to prevent the boil-off of cryogenic fuel is included in the parameter $\rho_{tank}$. The fidelity of the analysis could be further enhanced by including a dedicated thermal analysis of the insulation system. This addition would allow the model to explicitly account for the specific storage requirements of different cryogenic fuels, such as the significantly lower temperature of Liquid Hydrogen compared to LNG, and the resulting variations in insulation thickness.

### Total weight of the propulsion system

The total weight of the **propulsion system** is defined as the weight of the propellant system plus the weight of the engines:

$$W_{pros} = W_{tnk} + W_{eng} \tag{4.33}$$

### Subsystem Weight

Some additional secondary components are now introduced, namely the hydraulic, avionics, electrical, and general equipment subsystems. The corresponding empirical relations used for their weight estimation are derived from Ref. [10].

The weight of the **hydraulic system** comprises the components required to generate and regulate hydraulic pressure, including pumps, control valves, storage tanks, and the distribution network but without actuators.

Its weight is evaluated through the following relation:

$$W_{hydr} = 2.64 \cdot \left( \left( \frac{(S_{ref} + S_{wfv} + S_{wfh}) \cdot Q_{max}}{1000} \right)^{0.334} \cdot \left( L_b + W_{span}^{0.5} \right) \right) \tag{4.34}$$

The **avionics system** encompasses the guidance and navigation units, which ensure continuous knowledge of vehicle position and trajectory. It also includes the instrumentation required for measurement and monitoring of the flight parameters, as well as the communication equipment necessary to maintain links between the vehicle and external air or ground stations. The corresponding weight is estimated as:

$$W_{taves} = 66.37 \cdot W_{gtot}^{0.361} \tag{4.35}$$

The **electrical subsystem** accounts for the components required to generate, convert, and distribute the electrical power necessary to operate the various onboard systems. The main elements include batteries, AC generators, transformer–rectifier units, control devices, and the power distribution network. The weight of all these elements of the electrical subsystem is calculated using the following equation:

$$W_{elect} = 1.167 \cdot \left( W_{gtot}^{0.5} \cdot L_b^{0.25} \right) \tag{4.36}$$

Finally, the **equipment weight** includes the environmental control systems (ECS) as well as other auxiliary mechanical, hydraulic, and electrical installations. This category specifically captures components, such as certain actuators, that are not already included in the primary hydraulic subsystem calculation.

The corresponding weight contribution is estimated using the following relationship:

$$W_{equip} = 10000 + 0.01 \cdot (W_{gtot} - 0.0000003) \tag{4.37}$$

The sum of these contributions yields the **total weight of the subsystems**, which typically represents between 5% and 10% of the total gross weight of the vehicle.

$$W_{sub} = W_{hydr} + W_{taves} + W_{elect} + W_{equip} \tag{4.38}$$

### 4.3.3 Global parameters update and convergence verification

Once the vehicle geometry is defined and the weight estimation for all individual subsystems is complete, the code updates the global vehicle parameters. Specifically, the new **Total Gross Weight** ($W_{G,tot}$) and **Total Vehicle Volume** ($V_{tot}$) are calculated.

$$W_{g,tot} = W_{fuel} + W_{pay} + W_{str} + W_{prop} + W_{sub} \tag{4.39}$$

$$V_{tot} = \frac{W_{gtot} - \delta \cdot (W_{fuel} + W_{tnk}) - W_{pay} - W_{tps}}{\rho_A} + \delta \cdot \frac{W_{fuel}}{\rho_{fuel}} + V_{pay} \tag{4.40}$$

Subsequently, the algorithm proceeds to the **convergence check**. This verification is based on the stability of the gross weight between iterations. The sizing loop ends only when the absolute difference between the current weight ($W_{gtot,i}$) and the weight from the previous iteration ($W_{gtot,i-1}$) falls below a specified tolerance threshold ($\epsilon$), set to 10 lbf:

$$|W_{G,tot,i} - W_{G,tot,i-1}| \leq \epsilon \tag{4.41}$$

If this condition is not satisfied, the algorithm initiates a new iteration. A critical step before re-entering the sizing loop is the **re-calibration** of the three geometrical constants ($k_c$, $k_b$, $k_n$). Unlike the initialisation step, which relied on preliminary estimates, this re-calibration employs the computed vehicle characteristics from the sizing loop itself. For example, the constant $k_n$ is recalculated using the newly updated total volume ($V_{tot}$), leading to the reformulated expression of Equation 4.8:

$$k_n = D_{be} \cdot \left( \frac{2\pi \left( \frac{1}{6\tan(\theta_f)} + \frac{A_{lorb}}{2} + \frac{1}{6\tan(\theta_r)} \right)}{\frac{W_{gtot} - \delta \cdot (W_{fuel} + W_{tnk}) - W_{pay} - W_{tps}}{\rho_A} + \delta \cdot \frac{W_{fuel}}{\rho_{fuel}} + V_{pay}} \right)^{\frac{1}{3}} - 1 \tag{4.42}$$

## 4.4 Geometrical representation of the configuration

The final part of the preliminary design tool provides a graphical representation of the aircraft geometry through a **two-dimensional sketch**. In this step, additional equations

are introduced to complement those previously defined, particularly with regard to the wing and tail geometry parameters.

To generate the geometric layout, a set of input parameters is required to describe the characteristics of the fuselage and horizontal surfaces. These parameters, summarised below, define the fuselage geometry and the proportions and relative positioning of the lifting surfaces and are used in the *MATLAB* code to update the configuration geometry:

- $L_b$, Total fuselage length.
- $B_b$, Body width is the maximum width of the fuselage cross-section.
- $\theta_f$ and $\theta_r$, Angles that define the inclination of the nose and rear segments of the fuselage, respectively.
- $S_{ref}$, Wing surface.
- $W_{\text{span}}$, Total wingspan of the aircraft.
- $AR$, Aspect ratio of the wing.
- $\lambda$, Wing taper ratio, defined as the ratio between the lengths of the tip and the root chord.
- $C_{\text{root}}$, Wing root chord, computed iteratively as a function of wing area and span.
- $x_{\text{LE}}/L_b$, Non-dimensional longitudinal position of the wing leading edge relative to the length of the fuselage.
- $\Lambda_{\text{LE}}$ and $\Lambda_{\text{TE}}$, Sweep angles of the leading and trailing edge.
- $A_{hfp}$, Ratio of horizontal stabilizer area over the wing area.
- $AR_{tail}$, Aspect ratio of the tail.
- $\lambda_{tail}$, Taper ratio of the tail.
- $\Lambda_{\text{LE}_{tail}}$, Sweep angle of the leading edge of the tail.

**Wing**

The wing taper ratio, $\lambda$, is kept constant and equal to that of the reference configuration. Conversely, the length of the root chord $C_{\text{root}}$, which depends on the reference surface of the wing and the wingspan, is updated at each iteration according to the following relation:

$$C_{\text{root}} = \frac{2\, S_{\text{ref}}}{W_{\text{span}} \cdot (1+\lambda)} \tag{4.43}$$

The input parameter $\Lambda_{1/2}$ corresponds to the mid-chord angle of sweep. However, for the generation of the planform sketch, the leading and trailing edge sweep angles are required. Their computation has been integrated into the code through the following expressions:

$$\Lambda_{\mathrm{TE}} = \tan^{-1}\left(\frac{C_{\mathrm{root}} \cdot (1-\lambda)}{W_{\mathrm{span}}}\right) \tag{4.44}$$

$$\Lambda_{\mathrm{LE}} = \tan^{-1}\left(\tan(\Lambda_{\mathrm{TE}}) + \frac{1-\lambda}{AR(1+\lambda)}\right) \tag{4.45}$$

where $\Lambda_{\mathrm{LE}}$ and $\Lambda_{\mathrm{TE}}$ are defined as the angles between the respective wing edges and the $y$-axis of the aircraft, following the typical aeronautical convention as illustrated in Fig. 4.6.

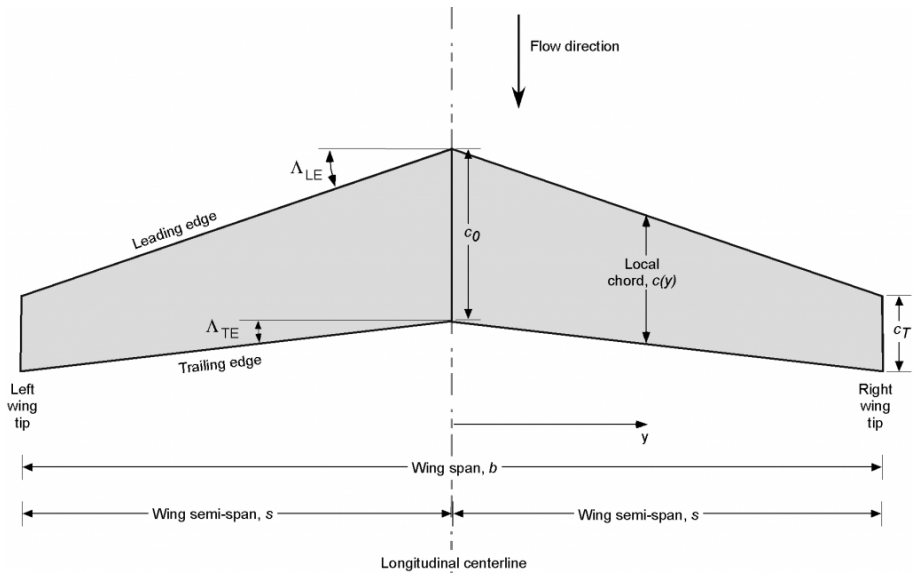


**Figure 4.6:** Wing sweep angle $\Lambda$ [14]

Another important geometric parameter is the ratio between the longitudinal position of the leading edge of the wing and the total length of the fuselage. From the schematic representation reported in Ref. [6], the position of the leading edge can be approximated, allowing the evaluation of the non-dimensional parameter $x_{\mathrm{LE}}/L_b$, which is then used as an input for the geometric model. For the present analysis, based on the *HYCAT-1A* configuration, this ratio has been set to 0.41.

### Horizontal Tail

For the geometric representation of the tail surface, the only parameter already included among the input variables used in the iterative sizing process is the horizontal ratio between the tail and the wing area $A_{hfp}$. Through this parameter, the horizontal tail reference area can be expressed as:

$$S_{\mathrm{tail}} = A_{hfp} \cdot S_{\mathrm{ref}} \tag{4.46}$$

The remaining geometric parameters of the tail, namely the aspect ratio $AR_{\mathrm{tail}}$, the leading-edge angle of sweep $\Lambda_{\mathrm{LE,tail}}$, and the taper ratio $\lambda_{\mathrm{tail}}$, were kept equal to those of the original *HYCAT-1A* configuration. These values were set respectively to $AR_{\mathrm{tail}} = 1.76$,

$\Lambda_{\text{LE,tail}} = 55°$, and $\lambda_{\text{tail}} = 0.314$, while the total tail surface area $S_{\text{tail}}$ varies iteratively according to the overall sizing process.

Based on these parameters, the unknown geometric quantities of the horizontal tail, such as the span, mean aerodynamic chord, and lengths of the root and tip chord, are determined using the following relations:

$$b_{\text{tail}} = \sqrt{AR_{\text{tail}} \cdot S_{\text{tail}}} \tag{4.47}$$

$$\bar{C}_{\text{tail}} = \frac{b_{\text{tail}}}{AR_{\text{tail}}} \tag{4.48}$$

$$C_{\text{root,tail}} = \frac{3}{2}\bar{C}_{\text{tail}}\left(\frac{1+\lambda_{\text{tail}}}{1+\lambda_{\text{tail}}+\lambda_{\text{tail}}^2}\right) \tag{4.49}$$

$$C_{\text{tip,tail}} = \lambda_{\text{tail}} \cdot C_{\text{root,tail}} \tag{4.50}$$

This formulation ensures that the tail geometry evolves consistently with the wing design, maintaining the same proportionality with respect to the reference configuration while allowing for updates during the iterative process.

The implemented code makes it possible to generate a two-dimensional representation of the aircraft planform, constructed from the parameters derived in the previous sections. This visualization serves both as a validation tool for the geometric relations and as a preliminary reference for the configuration layout, as shown in Fig. 4.7.

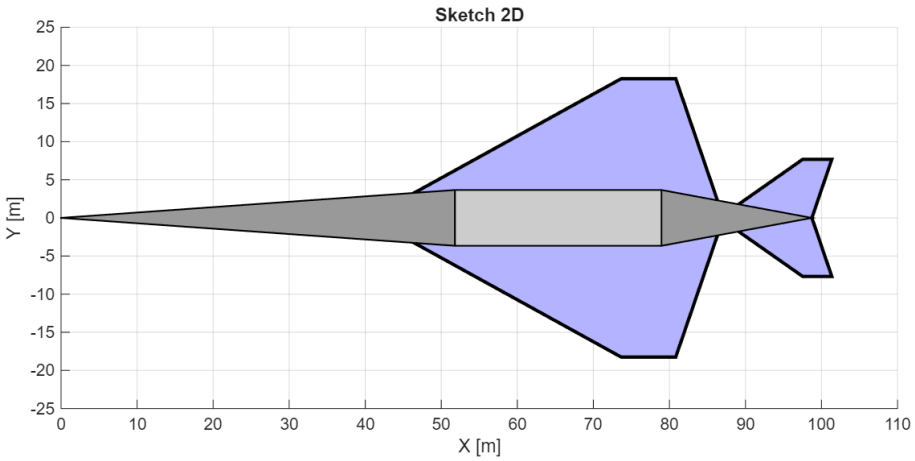


**Figure 4.7:** Sketch of the configuration

# Chapter 5

# Results and Performance Evaluation

This chapter presents the detailed results obtained from the preliminary design analysis of the **Liquid Methane (LNG)** powered aircraft. The chapter is organised to reflect the design workflow, moving from the definition of the performance constraints to the final vehicle sizing.

First, the **Matching Chart analysis** is presented to define the feasible design space. By intersecting the requirements derived from the subsonic, supersonic, and hypersonic flight regimes, the viable region for the Thrust-to-Weight ratio ($T/W$) and Wing Loading ($W/S$) is identified.

Subsequently, the operational flexibility of the vehicle is assessed through the **Payload-Range diagram**, illustrating the aircraft's performance capabilities.

Finally, the chapter details the **preliminary design results** generated by the iterative sizing code. This section provides an in-depth description of the converged vehicle configuration, focusing on its final geometric characteristics, mass breakdown, and component weights.

## 5.1 Matching chart analysis

The matching chart is a useful tool for the conceptual design phase. It allows us to represent for the performance requirements in terms of **Thrust to Weight ratio** and **Wing Loading** for different mission phases. The main goal is to find the region that meets all aircraft performance requirements, to obtain from the beginning a reference vehicle configuration. Accurately defining the fundamental performance parameters of the vehicle, such as thrust, weight, and lifting surface, is essential to identify a realistic design point that can serve as a baseline for subsequent development phases.

The wing loading ratio ($W/S$) indicates how much load is held by each unit area of the wing, while the thrust-to-weight ratio ($T/W$) is usually associated with aircraft powered

by air breathing engines; it represents how much thrust is needed for each unit of weight.

In the design of high-speed vehicles, the performance requirements must be evaluated separately for **subsonic**, **supersonic**, and **hypersonic** regimes, since a single matching chart is no longer sufficient to capture the entire operational envelope. A direct comparison between subsonic and hypersonic cruise requirements is irrelevant, since the two flight regimes are typically supported by different propulsion systems. In the present case, a turbojet is employed during the subsonic phase, while the ramjet operates throughout the hypersonic cruise. Moreover, normalising the hypersonic cruise requirement with respect to sea-level atmospheric conditions would lead to unrealistically high thrust demand. Another important aspect concerns the wing loading ($W/S$): at high speeds the effective vehicle weight is lower than in the subsonic case, as part of the propellant is consumed during acceleration to hypersonic conditions. Consequently, defining the hypersonic cruise requirement on the basis of the maximum take-off weight (MTOW) would not provide a realistic representation of the actual operating condition.

As a result, a single design point can only represent one specific operating mode of the propulsion system, and merging the requirements of different speed regimes into one diagram may lead to ambiguous results. To overcome this limitation, the present work adopts a **Multiple Matching Chart** methodology, inspired by the approach presented in [15]. This framework allows for the independent evaluation of thrust-to-weight ($T/W$) and wing loading ($W/S$) requirements for each flight regime.

To build a meaningful chart, it is essential to rely on validated reference data. In the present work, the mission profile has already been described in the dedicated section, while the **performance data** adopted for the construction of the matching charts are taken from the reference configurations *HYCAT-1A* and *HYCAT-1*, as reported in Ref [6] and Ref [3]. These datasets provide a validated benchmark, ensuring consistency with established concepts of hypersonic vehicles and offering a solid foundation for assessing the design requirements. In particular, information on the aerodynamic behaviour of the aircraft throughout the different mission phases, specifically the lift and drag coefficients, must be available from the outset of the analysis.

### 5.1.1 Subsonic requirements

Having established the general concept of the matching chart, the analysis now shifts to its application for the **subsonic part** of the mission. This phase presents a significant design challenge for a hypersonic vehicle.

The core issue is that the airframe, which is inherently optimised for high-Mach and high-altitude flight, must also satisfy the operational and safety demands of a conventional aircraft during low-speed, low-altitude flight. This regime is governed by stringent airworthiness regulations that dictate performance metrics such as *take-off field length*, minimum *second-segment climb gradients*, and *landing approach distance*.

Each of these subsonic segments imposes unique, and often conflicting, constraints on the aircraft's primary design parameters. The subsonic matching chart is the tool used to navigate this complex design space because it provides a graphical representation of all these competing requirements, conventionally plotting the **thrust-to-weight ratio** $(T/W)$ against the **wing loading** $(W/S)$.

The objective is to identify the "*feasible region*" or "*design window*", a region on the chart where all subsonic constraints are met simultaneously. It is crucial to note that for this specific analysis, the requirements in terms of thrust refer exclusively to the performance of the **turbojet engines**, since the only engines operating in this regime.

### Take-off distance

According to *CS-25 regulations*, the take-off distance with all engines operating is defined as 115 % of the ground roll distance needed to clear a 35 $ft$ obstacle.

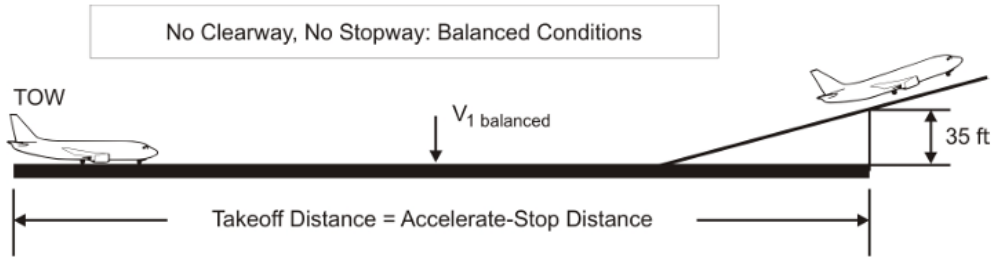


**Figure 5.1:** Take-off distance length [16]

However, in the context of the Matching Chart, the requirement is generally expressed in terms of lift-off distance, i.e., the ground distance required for the aircraft to become airborne, rather than the full certified take-off phase.

The take-off distance requirement is expressed by the following equation:

$$\left(\frac{T}{W}\right)_{LO} = \frac{\frac{W_{LO,kg}}{S}}{\rho_0 \sigma l_{LO} C_{L_{LO}}} \tag{5.1}$$

In this expression, $\rho_0$ denotes the **sea-level air density** $(1.225\,kg/m^3)$, while $\sigma$ represents the **relative density ratio**, introduced to normalise the governing equations to the standard atmospheric conditions at sea level. The parameter $l_{LO}$ refers to the **lift-off ground run distance**; consistent with the reference study, a total take-off field length of $3,000\,m$ was assumed, applying the standard engineering approximation that the lift-off point occurs at 60% of the total take-off distance. Finally, the aerodynamic term $C_{L_{LO}}$ represents the **lift coefficient during the ground roll**. This was set to 0.46, corresponding to a configuration with deflected flaps and a rotation angle of attack of 10°, representative of the take-off rotation.

### Second segment

The second segment of the take-off trajectory begins once the aircraft clears the virtual obstacle located at 35 $ft$ altitude (gear up altitude) and extends up to a minimum height of 400 $ft$. Throughout this phase, the aircraft maintains the lift-off configuration.

The performance requirement for this segment can be expressed through the following relation:

$$\left(\frac{T}{W}\right)_{2nd} = \frac{N_{engines}}{N_{engines} - 1} \cdot \left(\frac{1}{E_{2nd}} + G_{2nd}\right) \cdot \frac{1}{\sigma} \tag{5.2}$$

No specific **climb gradient** requirements are imposed for high-speed vehicles; therefore, the minimum value prescribed for conventional aircraft was adopted. For multi-engine configurations these are:

- 2.4 % in case of two engines
- 2.7 % in case of three engines
- 3 % in case of four engines

The configuration studied in this work is equipped with four engines, and thus a climb gradient of 3 % was adopted. The reference **altitude** was set at 200 $m$ and, finally, the **aerodynamic efficiency** parameter $E_{2nd}$ was assumed equal to 4.8, consistent with the climb phase values reported in the table of the reference mission profile [3].

### Subsonic climb

The subsonic climb requirement is formulated to ensure that the aircraft can achieve the necessary altitude gain under realistic aerodynamic and propulsion conditions. This constraint is typically expressed in terms of *climb gradient* and *dynamic pressure*, using the following equation:

$$\left(\frac{T}{W}\right)_{subclimb} = \left(\frac{q_\infty C_{D0}}{\frac{W_{kg}}{S} g} + G_{subclimb}\right) \cdot \frac{1}{\Pi \cdot \sigma} \tag{5.3}$$

The climb segment commences immediately following the second segment. To evaluate the performance requirement, a **representative operating altitude** was selected first. Since the nominal flight path reaches the subsonic cruise condition (Mach 0.9) at 7,000 $m$, a midpoint altitude of 3,500 $m$ was adopted as the reference condition for this analysis. By interpolating the nominal trajectory, a corresponding **flight speed** of Mach 0.65 was obtained, from which the **true airspeed velocity** was derived. At this altitude the atmospheric properties, specifically the density ratio $\sigma$, were evaluated using the *International Standard Atmosphere (ISA)* model.

Regarding the aerodynamic loads, the mission trajectory detailed in Section 3 indicates that dynamic pressure varies significantly, increasing from $\approx 9 kPa$ at take-off to a constant $48\,kPa$ ($\approx 1,000\,psf$) at Mach 2. For the specific calculation of the climb requirement, the **reference dynamic pressure** was computed according to the standard definition:

$$q_\infty = \frac{1}{2}\rho V^2 \tag{5.4}$$

Finally, regarding the performance assumptions, the subsonic **climb gradient** was fixed at $G_{subclimb} = 0.02$, with a maximum **throttle setting** ($\Pi = 100\,\%$). The **zero-lift drag coefficient** was assumed equal to $C_{D_0} = 0.02$.

### Subsonic cruise

The equation for subsonic cruise is similar to that of the subsonic climb requirement, neglecting the climb gradient, which is usually irrelevant during cruise. The drag coefficient can be computed in two different ways; for this reason, it is possible to distinguish between:

$$\textbf{Best Range Equation :} \qquad \left(\frac{T}{W}\right)_{subcruise,BR} = \left(\frac{4/3\, q_\infty C_{D_0}}{\frac{W_{kg}}{S}\cdot g}\right)\frac{1}{\Pi\cdot\sigma} \tag{5.5}$$

$$\textbf{Best Endurance Equation :} \qquad \left(\frac{T}{W}\right)_{subcruise,Be} = \left(\frac{2\, q_\infty C_{D_0}}{\frac{W_{kg}}{S}\cdot g}\right)\frac{1}{\Pi\cdot\sigma} \tag{5.6}$$

In this study, the requirement was imposed using the **Best Range formulation**.

In the subsonic cruise phase, the **reference flight condition** was defined at Mach 0.9. Once the Mach number was fixed, the corresponding altitude was determined by interpolating the nominal trajectory, resulting in $7,000\,m$. At that altitude, the density ratio $\sigma$ was evaluated using the International Standard Atmosphere model, which also provides the density and temperature values required to compute both the velocity and the dynamic pressure.

For this phase, the **zero-lift drag coefficient** was assumed unchanged ($C_{D_0} = 0.02$), while the throttle setting was maintained at $100\,\%$.

### Landing

In compliance with *CS-25 regulations*, the landing distance is defined as the horizontal distance required for the aircraft to descend from $50\,ft$ above the runway and come to a complete stop, as illustrated in the figure below.

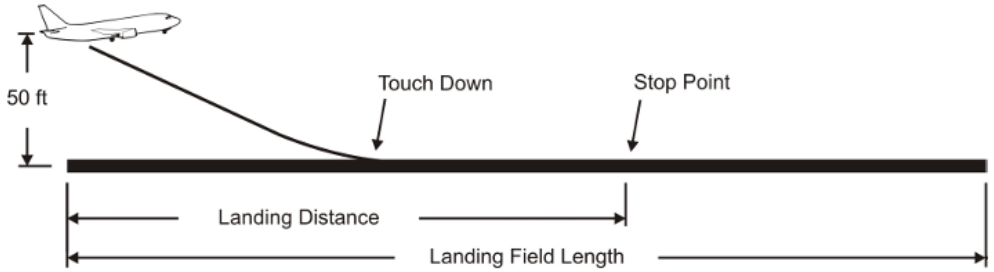


**Figure 5.2:** Landing field length [16]

For the present concept, the **landing field length** was taken from the reference literature and set to $3,200\,m$. This value was also verified through an analysis of runway lengths at major international airports. This constraint ensures compatibility with nearly all primary hubs around the world, confirming it as a reasonable and operationally viable design choice.

The **wing loading** at landing is determined from the following relation:

$$\left(\frac{W}{S}\right)_{lnd} = \frac{\rho V_{app}^2 C_{L_{app}}}{2\,g} \tag{5.7}$$

Moreover, the correlation between the **approach speed** and landing field length for jet aircraft is provided by Ref. [16] and is expressed as:

$$V_{app} = k_{app} \cdot \sqrt{s_{lfl}} \tag{5.8}$$

where $k_{app} = 1.7\,\sqrt{m/s^2}$ represents the so called "***Loftin parameter***".

For this calculation, the **density ratio** $\sigma$ was assumed equal to 1 since sea-level conditions were considered in this phase. The approach configuration corresponds to an angle of attack of 10° at Mach 0.35. From the "low-speed lift" reference curve of Fig. 2.9, this yields a **Lift Coefficient** of $C_{L_{app}} = 0.56$.

### 5.1.2 Supersonic requirements

Following the subsonic analysis, the focus now shifts to the **supersonic domain**, which is characterised as the flight regime from Mach 1.0 up to 5.0. This regime requires a completely separate performance evaluation since the characteristics of the aircraft differ significantly from those observed at lower speeds.

Two major factors drive this complexity:

- **Aerodynamics:** The appearance of compressibility effects, specifically the introduction of **wave drag** at $M > 1$, fundamentally alters the lift to drag ratio of the aircraft.

- **Propulsion:** This phase is defined by a complex propulsion "hand-off". The system must transition from the pure turbojet used during the subsonic flight, through a combined TurboJet-RamJet mode assumed here between Mach 1 and 3.5, before relying solely on the ramjet engine at higher speeds.

A dedicated **Supersonic Matching Chart** is therefore developed to map the design space under these new conditions. Its purpose is to find a viable ($T/W$, $W/S$) solution that takes into account the high dynamic pressures, the severe wave drag, and the changing thrust characteristics of the combined-cycle propulsion. The methodology and assumptions used to derive this matching chart are detailed in the following sections.

### Supersonic climb

The model adopted for the supersonic climb closely follows the formulation used in the subsonic case. However, the main difference lies in the evaluation of the drag coefficient, which at supersonic speeds must account for wave drag and compressibility effects.

The requirement for the supersonic climb can therefore be expressed as:

$$\left(\frac{T}{W}\right)_{super,climb} = \left(\frac{q_\infty C_{D_{sup}}}{\frac{W_{kg}}{S}\cdot g} + G_{sup,climb}\right)\frac{1}{\Pi\cdot\sigma^*} \tag{5.9}$$

Following the nominal flight path discussed in section 3, this portion of the trajectory extends from an altitude of about $7,000\,m$ to $24,500\,m$, where Mach 5 is reached. For the evaluation of the requirement, a **representative operating condition** was selected at the midpoint of the speed range, corresponding to Mach 3. From the mission profile, the associated **altitude** at this Mach number was found to be approximately $18,500\,m$, which was subsequently used to determine the dynamic pressure.

The supersonic **drag coefficient** was derived following the methodology outlined in Section 2.2.2. Based on the aerodynamic curves for an angle of attack of 4°, a value of $C_{D_{sup}} = 0.0203$ was obtained.

The minimum **climb gradient** was set to $G_{sup,climb} = 0.014$, a value slightly lower than that adopted for the subsonic phase. This assumption is supported by the trajectory analysis of the mission, which shows an increase in altitude from 7 to $27km$ over a horizontal distance of $1,500\ km$, corresponding to an average slope of approximately 1.4 %. The **throttle** setting was maintained at maximum ($\Pi = 100\,\%$).

Regarding density corrections, the effective density ratio ($\sigma^*$) is typically defined relative to specific reference altitudes such as the *Beginning Of Supersonic Climb* (**BOC**) or the *Top Of Supersonic Climb* (**TOC**). However, in the present case, correction using the effective density ratio $\sigma^*$ is not required, since the supersonic matching chart includes only the climb requirement, and no other conditions referenced to different altitudes are represented.

#### Supersonic wing loading

The wing loading requirement is represented as a vertical line on the supersonic matching chart. It was calculated using the same **design reference wing area** adopted for the subsonic regime and the **aircraft weight** corresponding to approximately the midpoint of the supersonic climb. This weight was derived by subtracting the fuel consumed during taxi operations and approximately 60 % of the total fuel required for the entire climb, including both subsonic and supersonic portions. This approach provides a realistic representation of the operating condition in supersonic flight, ensuring a consistent and accurate estimation of the required thrust-to-weight ratio relative to the specific flight regime.

### 5.1.3 Hypersonic requirements

In the hypersonic regime, corresponding to Mach numbers between 5 and 6 where the RamJet engine is used, the matching chart methodology is adapted to reflect the unique flight characteristics at these extreme speeds. Only the climb and cruise segments are considered since phases like take-off and landing does not influence hypersonic flight.

The analysis also accounts for the reduction in vehicle weight resulting from previous high-speed acceleration and propellant consumption. This approach provides a clear visualization of the performance envelope at hypersonic speeds and facilitates the identification of a feasible global design point for the vehicle.

#### Hypersonic climb requirement

With the exception of the specific formulation for the drag coefficient, the hypersonic climb requirement follows the same methodological approach adopted for the previous climb segment and is included primarily for completeness, although the shallow climb rates typical of this regime are not expected to represent a dimensioning constraint.

The thrust-to-weight ratio requirement for the hypersonic climb is governed by the following relationship:

$$\left(\frac{T}{W}\right)_{hyp,climb} = \left(\frac{q_\infty C_{D_{hyp,climb}}}{\frac{W_{kg}}{S}\cdot g} + G_{hyp,climb}\right)\frac{1}{\Pi\cdot\sigma^*} \tag{5.10}$$

This segment begins immediately after the vehicle exceeds Mach 5, corresponding to an altitude of approximately $24,500\,m$, and extends to the initial cruise altitude of $27,000\,m$, where the design Mach number of 6 is reached. To evaluate this requirement, a **representative operating condition** was selected at the midpoint of the Mach range, corresponding to Mach 5.5 and an **altitude** of approximately $26,000\,m$.

The **hypersonic drag coefficient** was evaluated following the methodology described in Section 2.2.2; using the aerodynamic data for an angle of attack of 4°, a value of $C_{D_{hyp,climb}} = 0.0146$ was obtained. The **climb gradient** was assumed identical to that

used for the subsonic climb phase, namely $G_{hyp,climb} = 0.014$, and the maximum **throttle setting** was maintained.

In this context, the reference altitude used to normalise the requirement was selected as the *Top of Climb* (**TOC**) condition. This choice ensures consistency with the reference wing loading line displayed in the matching chart, which was calculated using the aircraft weight at the end of the climb segment. Consequently, the corresponding **correction factor** was applied through the density ratio:

$$\sigma^* = \frac{\rho_{26000}}{\rho_{28600}}$$

**Hypersonic cruise requirement**

The hypersonic cruise requirement is formulated in a way similar to the hypersonic climb, with the only difference being that the climb gradient is neglected.

The corresponding equation is, therefore:

$$\left(\frac{T}{W}\right)_{hyp,cruise} = \left(\frac{q_\infty C_{D_{hyp,cruise}}}{\frac{W_{kg}}{S} \cdot g}\right) \frac{1}{\Pi \cdot \sigma^*} \tag{5.11}$$

Operationally, hypersonic aircraft do not typically maintain a perfectly constant altitude during cruise. Instead, a continuous increase in flight level is performed as fuel is consumed and the overall weight decreases. This practice, known as *step climb*, improves aerodynamic efficiency while reducing both drag and thermal loads. For the reference mission, the trajectory indicates an increase in altitude from approximately $27,000\,m$ at the start of the segment to $28,600\,m$ at the end.

However, as discussed in the Mission Profile section, this study adopted a simplifying assumption, modelling the entire cruise phase at a constant altitude corresponding to the maximum level reached. Consequently, to maintain consistency, the representative **cruise altitude** adopted for the analysis of the performance requirement was fixed at $28,600\,m$.

The **throttle setting** was set to maximum (100%), while the hypersonic **drag coefficient** was determined using the aerodynamic data for an angle of attack of $4° \,/\, 0°$, yielding a value of:

$$C_{D_{hyp,cruise}} = \left[C_{D_i} + C_{D_w} + C_{D_f}\right]_{M=6} = 0.0142 \tag{5.12}$$

Both the hypersonic climb and wing loading constraints are referenced to the **Top of Climb (TOC)** condition. Therefore, no density correction factor is required for the hypersonic cruise curve, as it shares the same reference altitude.

**Hypersonic wing loading**

The wing loading requirement in the hypersonic regime is depicted as a vertical line on the corresponding matching chart. This limit was determined using the same reference **wing area** adopted for the previous regimes, while the **aircraft weight** was defined at the Top Of Climb (TOC) in hypersonic conditions. This specific weight was derived by subtracting the fuel consumed during the taxi phase and the entire climb segment from the vehicle's gross weight.

## 5.2 Payload-Range diagram

With the mission profile and performance requirements now defined, the next step is to evaluate the vehicle's operational envelope. To do this, the **Payload — Range diagram** is introduced as the fundamental tool to visualise the relationship between transport capacity and achievable distance.

This diagram effectively maps the utility of the aircraft, illustrating the trade-off between the payload carried and the range that can be flown without refuelling. It allows for an immediate assessment of the vehicle's versatility, showing what kind of missions are feasible beyond the nominal design point.

The shape of this curve is unique to each configuration and depends on several design and performance factors, including aerodynamic efficiency, structural characteristics, propulsion performance and, critically for cryogenic-powered aircraft, the available fuel volume. Consequently, the resulting diagram acts as a "signature" of the technological choices adopted.

It is important to note that in this context, the Payload–Range diagram serves primarily as a **performance verification tool**, aimed at defining operational limits and mission feasibility, rather than a sizing instrument for the sizing methodology.

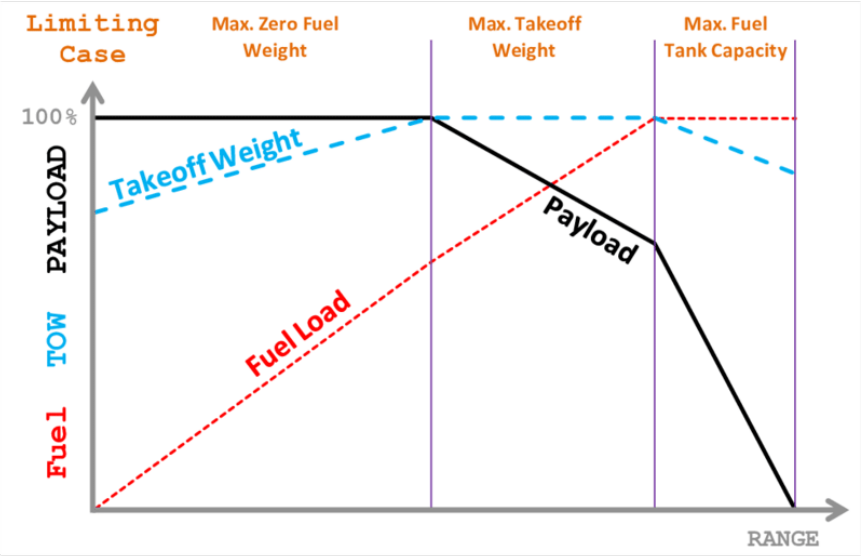


**Figure 5.3:** Example Payload - Range diagram [17]

In its general form, the resulting curve defines the vehicle's operational envelope through **three distinct segments**:

- The first segment is horizontal, representing the **Maximum Design Payload** regime. Here, the vehicle carries its full payload and the range is extended by adding fuel. This constant-payload phase continues until the total weight of the aircraft reaches the Maximum Take-Off Weight (MTOW).
- Beyond this point, extending the range further is possible, but requires entering the **MTOW-limited** regime. To accommodate the additional fuel weight required for longer distances without exceeding the gross weight limit, the payload must be progressively reduced. This creates the characteristic downward slope, representing the direct trade-off between payload capacity and fuel endurance.
- The final segment is defined by the **Maximum Fuel Capacity**. Once the tanks are physically full, no further range increase is possible, even if the MTOW limit has not been reached. The absolute maximum distance achieved at this point, typically with zero or negligible payload, is referred to as the *ferry range*.

By delineating these boundaries, the payload – range diagram effectively summarises the operational flexibility of the vehicle, providing engineers and operators with a clear understanding of its capabilities across various loading conditions and mission profiles.

### 5.2.1 Payload-Range diagram definition

This section details the specific Payload — Range diagram corresponding to the **Liquid Methane (LNG)** concept aircraft developed. Unlike the generic curve described previously, the diagram for this specific design is defined by two primary operational extremes:

the **Design Point** and the **Ferry Range**.

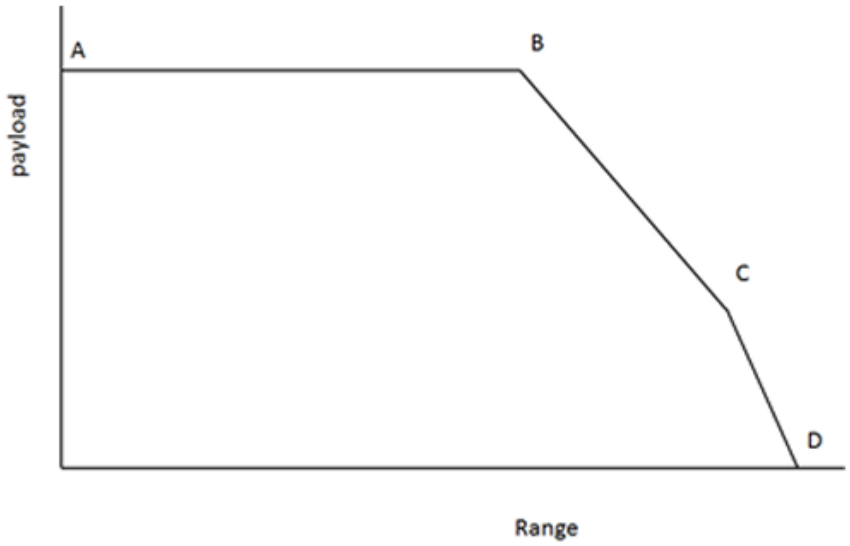


**Figure 5.4:** Payload - Range points

Points A and B are directly determined by the top-level inputs of the analysis. **Point A** represents the condition of maximum payload capacity with limited fuel, while **Point B** corresponds to the **Design Mission**: the vehicle carries the maximum payload (200 passengers) over the required design range. Crucially, since the sizing code calculates the tank volume exactly to satisfy this design mission, the total fuel capacity is strictly dimensioned to this requirement. Consequently, in this preliminary sizing context, the traditional "Point C" (Maximum Fuel with reduced payload) effectively coincides with the design fuel load.

The point requiring a dedicated analytical calculation is **point D** (Ferry Range). This represents the maximum achievable distance with **zero payload** while maintaining the **maximum design fuel load**, identical to the fuel weight calculated for Point B, including the 5 % safety margin discussed in the corresponding Section 4.1. Under these conditions, the aircraft operates at a weight significantly lower than the total gross weight. This lower weight reduces the absolute fuel consumption during the fixed-fraction mission segments (e.g., taxi, take-off, climb). The fuel saved in these phases is, therefore, redistributed to the cruise segment, extending the range. To quantify this extension, the *Breguet Range Equation* is rearranged to solve explicitly for the distance:

$$R = \frac{I_{SP} \cdot V_{cruise} \cdot E}{1000} \cdot \ln(\frac{W_{initial}}{W_{final}}) \tag{5.13}$$

The aircraft weights at the beginning and end of the cruise phase were determined based

on the following breakdown. The **Maximum Take-Off Weight (MTOW)** is defined as:

$$MTOW = OEW + W_{\text{fuel}} + W_{\text{pay}} \tag{5.14}$$

where **OEW** (Operating Empty Weight) represents the baseline weight of the aircraft. This value includes the structural weight, crew, and all systems and fluids required for operation, such as engine oil, coolant, water, unusable fuel, and standard equipment, excluding only usable fuel and payload.

For the specific case of **Point D**, where the payload is zero, the take-off weight is reduced to:

$$W_{\text{TO}} = OEW + W_{\text{fuel}} \tag{5.15}$$

Using this specific take-off weight and the fixed fuel fractions established for the mission segments, the fuel consumed before the cruise phase can be calculated. Accordingly, the **weight at the start of cruise** is:

$$W_{\text{initial}} = OEW + W_{\text{fuel}} - W_{\text{fuel,taxi}} - W_{\text{fuel,climb}} \tag{5.16}$$

Conversely, the **weight at the end of cruise** is defined by the remaining weight of the aircraft plus the fuel required for the subsequent phases (descent and landing):

$$W_{\text{final}} = OEW + W_{\text{fuel,descent}} + W_{\text{fuel,landing}} \tag{5.17}$$

With these weight values defined, the Breguet equation yields the updated cruise range for the ferry mission ($R_{D,cruise}$). The total Ferry Range ($R_D$) is then calculated by substituting the design cruise range ($R_{B,cruise}$) with this new value, while keeping the other mission segments unchanged:

$$R_D = R_B - R_{B,cruise} + R_{D,cruise} \tag{5.18}$$

This additive approach is valid under the assumption (described in the Mission Profile section) that the longitudinal distances covered during the climb and descent segments remain constant regardless of the payload.

The calculated payload and range values for the key operational points are summarised in Table 5.1. It should be noted that, although the sizing formulations discussed previously are based on weight parameters ($lbf$), the results presented in this table were converted to mass and are expressed in $kg$.

| Point | Range [km] | Payload [kg] | Fuel [kg] |
|---|---|---|---|
| A | 0 | 19 051 | 0 |
| B | 10 000 | 19 051 | 199 065 |
| D | 11 021 | 0 | 199 065 |

**Table 5.1:** Payload Range diagram relevant points (LNG)

Figure 5.5 illustrates the standard payload – range diagram. This analysis is further expanded in Figure 5.6, which details the **fuel mass** and the evolution of the **total gross mass** as a function of range.

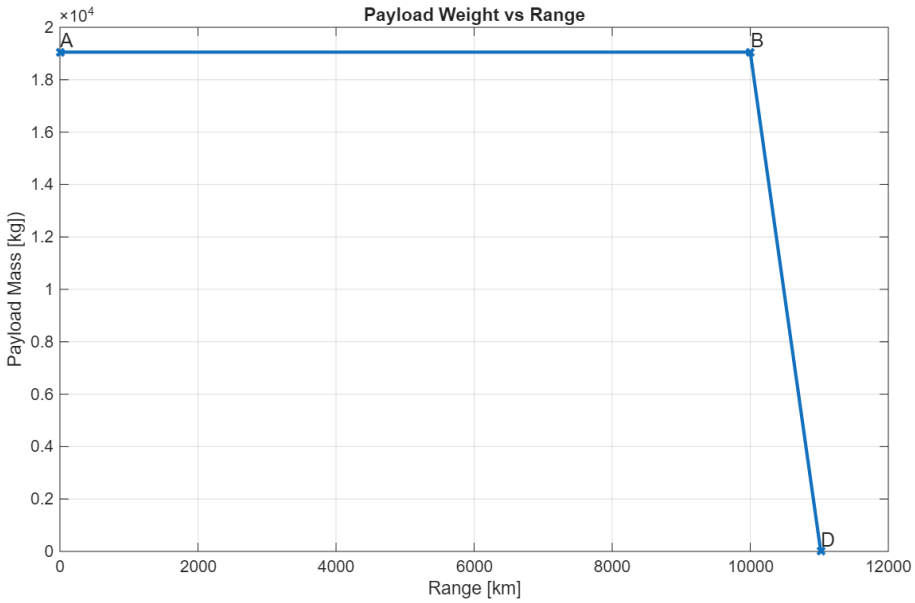


**Figure 5.5:** Payload - Range diagram

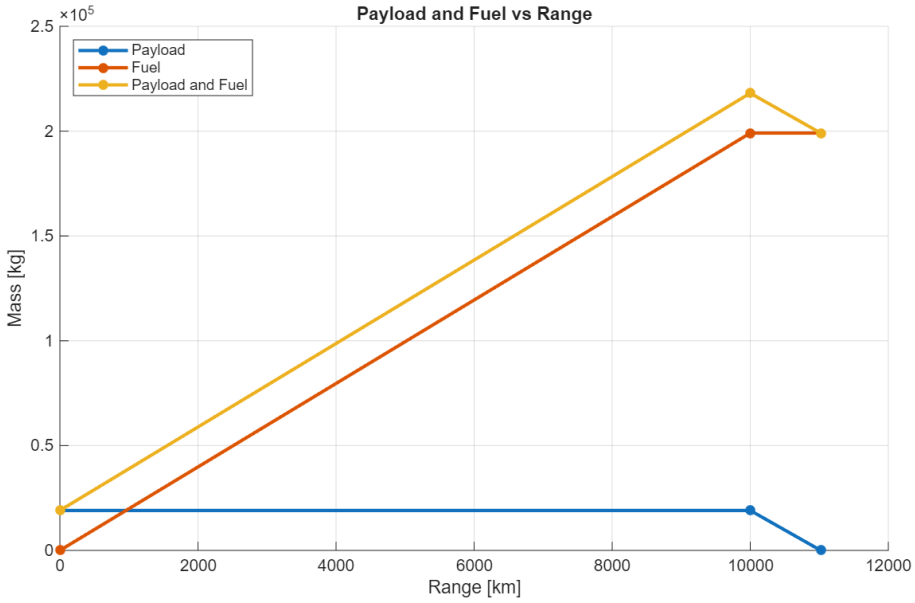


**Figure 5.6:** Fuel and Payload - Range diagram

## 5.3 Results of the preliminary design model

The preliminary design tool developed was applied to the hypersonic transport configuration inspired by the *HYCAT-1A* reference vehicle and adapted for operation with **liquefied natural gas (LNG)** as primary fuel. The code integrates all the correlations and models described in the previous sections, iteratively converging toward a consistent set of geometric and mass parameters that satisfy the imposed mission and performance requirements.

The sizing algorithm converged to the final vehicle configuration after 109 iterations. The key parameters defining this solution, such as the main geometrical characteristics, the reference areas, and subsystem masses, are summarised in Figure 5.7. To facilitate comparison with both the original input data list and the results of the original HASA method, and to ensure compatibility with standard aerospace design practices, the results are provided in both imperial and SI units. These outputs serve as the basis for the subsequent analysis process, including the matching chart generation and the payload-range analysis.

| Variables | Imperial Units | International Units |
|---|---|---|
| L_b | 323,95 | 98,74 |
| D_be | 21,51 | 6,56 |
| F_r | 15,06 | 15,06 |
| B_b | 24,00 | 7,32 |
| W_span | 119,77 | 36,50 |
| C_root | 152,96 | 46,62 |
| W_S | 86,00 | 419,88 |
| S_ref | 10570,43 | 982,02 |
| Sb_tot | 16735,20 | 1554,75 |
| S_tb | 8367,60 | 777,38 |
| S_wfh | 1443,92 | 134,14 |
| S_wfv | 1189,17 | 110,48 |
| W_b | 57487,54 | 26075,89 |
| W_fuel | 438863,93 | 199065,17 |
| W_tnk | 27338,19 | 12400,39 |
| W_emp | 470192,91 | 213275,74 |
| W_w | 78614,26 | 35658,80 |
| W_finh | 78744,29 | 35717,78 |
| W_finv | 11245,72 | 5100,97 |
| W_tps | 30572,92 | 13867,63 |
| W_gear | 45640,65 | 20702,23 |
| W_thrua | 2796,17 | 1268,32 |
| W_str | 305101,54 | 138391,62 |
| W_ttj | 56848,30 | 25785,93 |
| W_ttr | 0,00 | 0,00 |
| W_trj | 4363,47 | 1979,24 |
| W_tsj | 0,00 | 0,00 |
| W_eng | 61211,77 | 27765,17 |
| W_pros | 88549,97 | 40165,56 |
| W_hydr | 1322,71 | 599,97 |
| W_taves | 9397,73 | 4262,74 |
| W_elect | 4720,46 | 2141,16 |
| W_equip | 19090,57 | 8659,33 |
| W_sub | 34531,48 | 15663,20 |
| W_gtot | 909046,92 | 412336,41 |
| V_tot | 82377,81 | 2332,68 |

**Figure 5.7:** Results of the Sizing and Weighting analysis for the methane powered aircraft

In order to verify the numerical stability of the iterative procedure implemented in the preliminary design tool, the evolution of key parameters was closely monitored throughout the convergence loop. Specifically, Fig. 5.8 shows the evolution of the ***Calibration***

***constants*** $k_b$, $k_c$, and $k_n$. During the first iterations, these parameters demonstrate oscillatory behaviour around a mean value, which is a sign that the algorithm explores the surrounding solution space. As the computation proceeds, the size of the oscillation progressively decreases and the parameters get closer to equilibrium values, thus confirming the implemented convergence criteria.

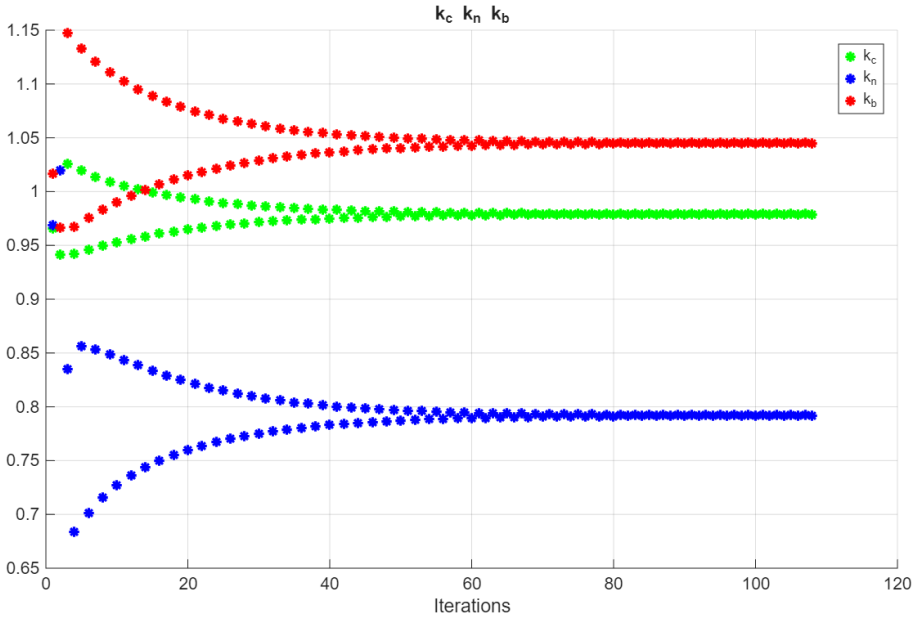


**Figure 5.8:** Calibration constants evolution

Similarly, Fig. 5.9 illustrates the evolution of the ***Total Gross Weight***, showing a consistent convergence trend. Although starting from a preliminary estimate, the value rapidly stabilises after a limited number of iterations.

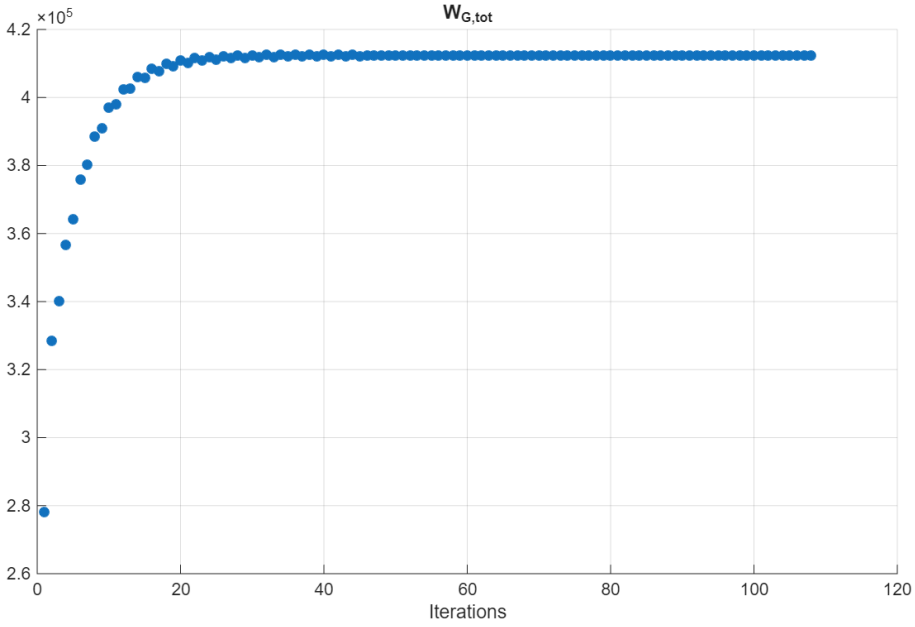


**Figure 5.9:** Total gross weight evolution

This general behaviour confirms that the implemented iterative scheme leads to a stable and consistent convergence of both global design parameters and local calibration factors, providing confidence in the robustness of the preliminary sizing methodology.

### 5.3.1 Matching Chart results

As discussed in the section dedicated to the matching charts, three distinct graphs are generated. The charts corresponding to the **supersonic** and **hypersonic** regimes are easily understandable, while the matching chart for the **subsonic** regime requires a more detailed analysis.

Typically, the critical design point is located at the maximum Thrust-to-Weight (T/W) and maximum Wing Loading (W/S). A closer examination of the **subsonic matching chart** reveals the presence of two different wing loading requirements, represented by the vertical lines: the *pink dashed line* indicates the take-off requirement, where the aircraft is at its maximum weight, while the *black dashed line* represents the landing requirement.

For a given wing area, the aircraft weight must vary between these two phases; meaning that the aircraft cannot land at take-off weight. This is a common practice for heavy transport vehicles, and in cases where an immediate landing is required, part of the fuel has to be jettisoned immediately to reduce the aircraft's weight and allow for a safe landing.

In the chart, the black vertical line intersects the blue curve representing the cruise requirement, whereas the pink vertical line intersects the take-off requirement curve. Both intersections occur at similar Thrust-to-Weight values, but the corresponding aircraft weight is clearly different. The **feasible design region** is located above the blue cruise curve and to the left of the black vertical line, while the area between the two vertical lines is only feasible if the wing area remains constant.

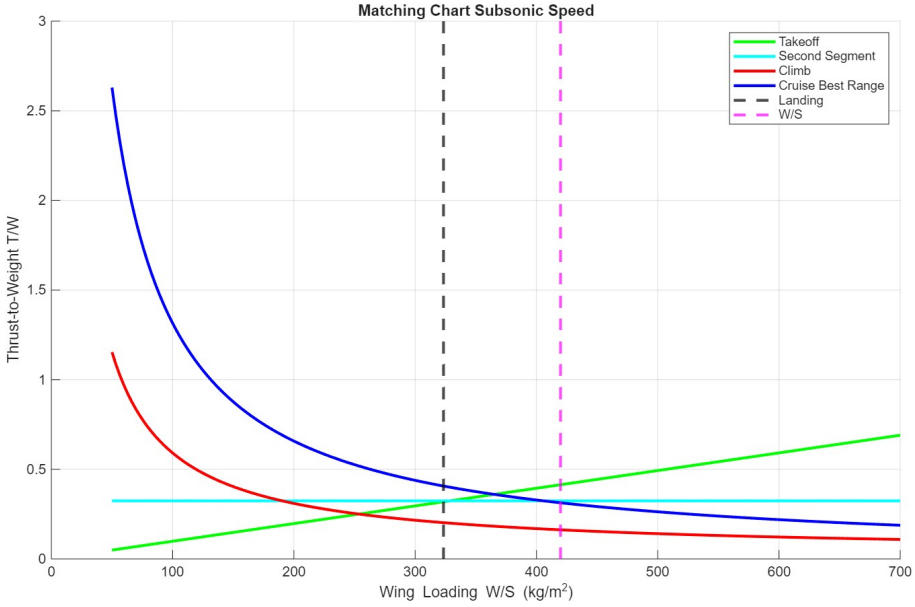


**Figure 5.10:** Matching chart at subsonic speed

The charts corresponding to the **supersonic** and **hypersonic** regimes are relatively straightforward. In both cases, the design point is identified at the intersection of the vertical wing loading line with the **limiting requirement**: specifically, the **climb curve** for the supersonic regime and the **cruise curve** for the hypersonic regime.

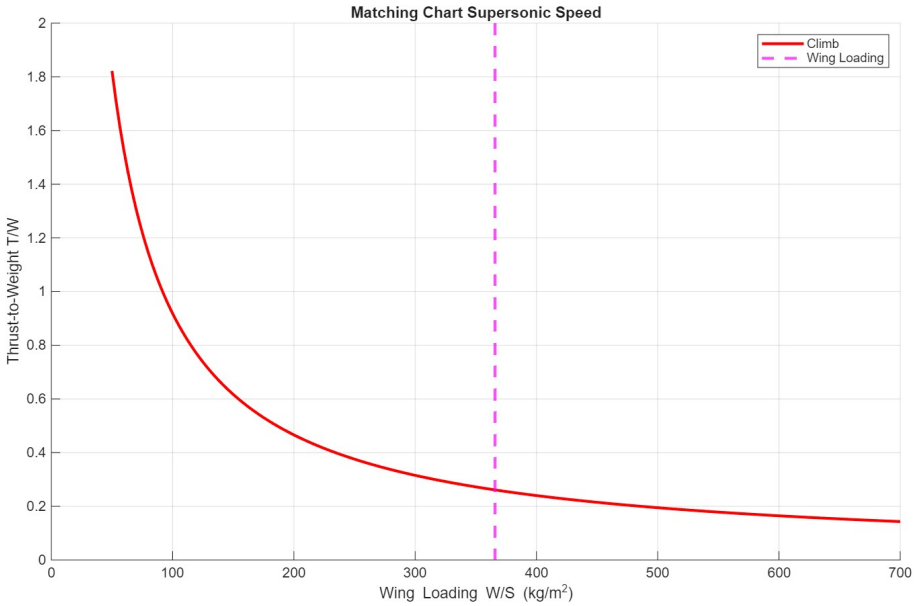


**Figure 5.11:** Matching chart at supersonic speed

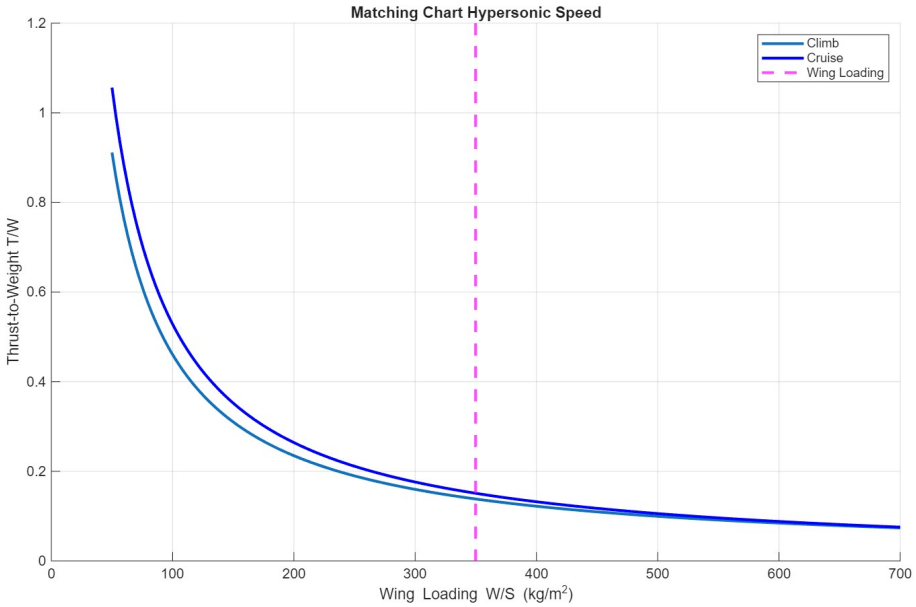


**Figure 5.12:** Matching chart at hypersonic speed

# Chapter 6

# Comparative Analysis: Liquid Hydrogen Case Study

With the preliminary design of the Liquid Methane (LNG) configuration now complete, the analysis can be extended to a critical comparison, with the goal of benchmarking the LNG design against its main cryogenic alternative, Liquid Hydrogen. As mentioned in the introduction, the choice between the two fuels is complex. $LH_2$ is an attractive option due to its zero $CO_2$ emissions and its superior calorific value, which means a higher specific impulse $I_{SP}$ and thus a lighter fuel mass .

However, these benefits come with a price, driven primarily by the extremely low density of $LH_2$. This physical property demands voluminous cryogenic tanks, imposing a severe penalty on the *Total Wetted Area* of the vehicle, which also increases aerodynamic drag. Furthermore, the challenges of storing $LH_2$ at $-253° C$ add complexity and mass to the tank structure, directly impacting the Operating Empty Weight (OEW).

This leads to the central trade-off that the sizing tool can now investigate: **Does the significant fuel mass saved by the high $\mathbf{I_{sp}}$ of $\mathbf{LH_2}$ actually compensate for the inevitable mass penalties from the larger and heavier tankage needed to store it?**

To answer this quantitatively, the flexibility of the MATLAB sizing methodology is used. A complete sizing iteration is performed for an $LH_2$-powered variant of the aircraft. This section details the necessary modifications to the input file and presents the resulting vehicle size, allowing a direct, data-driven comparison against the LNG baseline.

## 6.1 Specific assumptions and input parameters for the $LH_2$ vehicle

To perform a direct comparison, the core mission requirements and top level constraints were held constant for the $LH_2$ sizing run. The vehicle is still required to carry 200 passengers over the same reference mission profile, and the fundamental aerodynamic and geometric database of the *HYCAT-1A* are still used as a starting point. Therefore, any difference in final size is driven by the parameters directly affected by the change in fuel from LNG to $LH_2$.

The key **modifications to the input data** set are described below:

- **Fuel Properties:** The most significant changes are the **density** and **energy content** of the fuel. Liquid Hydrogen has a density of $\mathbf{71\,kg/m^3}$ compared to $450 kg/m^3$ for LNG and a Heating Value (HV) of $\mathbf{120\,MJ/kg}$, compared to $55\,MJ/kg$ for LNG.
- **Propulsion Performance and Fuel Fractions:** The higher energy content and superior combustion properties of hydrogen result in a much better specific impulse $I_{sp}$, which directly affects the performance of the propulsion system. The sizing model does not employ separate, detailed performance models for turbojet or ramjet engines. Instead, fuel consumption during the entire mission is calculated using the **fuel fraction method**, which consists of the definition of $W_{i+1}/W_i$ for each phase of the flight 'i'. For the cruise segment, this calculation is **dynamic**, using the *Breguet Range equation*, which is directly dependent on the vehicle's $I_{sp}$ and L/D ratio. For the other phases (e.g. take-off, climb, descent), simplified **fixed fuel fractions** are used, but a key feature of the code is that it automatically detects the fuel type based on the input density. It then uses this to scale all fixed fuel fractions for the non-cruise segments, which means it not only applies the appropriate $I_{sp}$ for hydrogen in the cruise formula. This ensures to account for the superior efficiency of hydrogen across the entire mission profile.
- **Fuel Tankage and Storage:** This is the primary penalty for $LH_2$ because, as already noted, storing fuel at a temperature of $-253^\circ C$ is significantly more complex than storing it at $-162^\circ C$, as required for Liquid Natural Gas. However, the model does not include a detailed sizing of the cryogenic insulation systems considering differences in the *multi-layer insulation (MLI)*. Instead, a simplified assumption was made and the **same tank mass fraction**, defined as the ratio of tank weight to the fuel weight it contains, is used for both the $LH_2$ and LNG configurations. An eventually difference in *Empty Weight* related to tankage is therefore driven by the different total *Fuel Volume* required as a consequence of the low density

These modifications define the complete input data set required to characterise the hydrogen-powered variant.

## 6.2 Sizing results of the $LH_2$ variant

Upon execution of the sizing analysis with these specific parameters, the algorithm successfully converged after 131 iterations to a feasible vehicle design that satisfies all mission constraints.

| Variables | Imperial Units | International Units |
|---|---|---|
| L_b | 340,22 | 103,70 |
| D_be | 22,58 | 6,88 |
| F_r | 15,07 | 15,07 |
| B_b | 25,20 | 7,68 |
| W_span | 100,42 | 30,61 |
| C_root | 128,25 | 39,09 |
| W_S | 86,00 | 419,89 |
| S_ref | 7431,49 | 690,41 |
| Sb_tot | 18455,41 | 1714,56 |
| S_tb | 9227,71 | 857,28 |
| S_wfh | 1015,14 | 94,31 |
| S_wfv | 836,04 | 77,67 |
| W_b | 63710,41 | 28898,53 |
| W_fuel | 199613,25 | 90542,97 |
| W_tnk | 66537,75 | 30180,99 |
| W_emp | 439495,25 | 199351,53 |
| W_w | 59028,58 | 26774,89 |
| W_finh | 51594,02 | 23402,63 |
| W_finv | 7659,48 | 3474,28 |
| W_tps | 26511,51 | 12025,41 |
| W_gear | 30715,76 | 13932,42 |
| W_thrua | 1986,33 | 900,98 |
| W_str | 241206,09 | 109409,15 |
| W_ttj | 56848,30 | 25785,93 |
| W_ttr | 0,00 | 0,00 |
| W_trj | 3067,72 | 1391,49 |
| W_tsj | 0,00 | 0,00 |
| W_eng | 59916,02 | 27177,43 |
| W_pros | 126453,77 | 57358,42 |
| W_hydr | 1171,79 | 531,52 |
| W_taves | 8275,31 | 3753,61 |
| W_elect | 4006,81 | 1817,46 |
| W_equip | 16391,09 | 7434,87 |
| W_sub | 29845,00 | 13537,45 |
| W_gtot | 639118,10 | 289898,86 |
| V_tot | 95375,23 | 2700,72 |

**Figure 6.1:** Sizing results for the $LH_2$-Powered Variant

The primary characteristics of the resulting vehicle powered by $LH_2$ are shown in Figure 6.1. This figure presents the main key geometric parameters and the weight breakdown in the same format used for the LNG baseline.

In order to demonstrate the **convergence and stability** of this design obtained as a result of the iterative analysis, the evolution of the calibration constants along with the Total Gross Weight are shown in Figure 6.2.

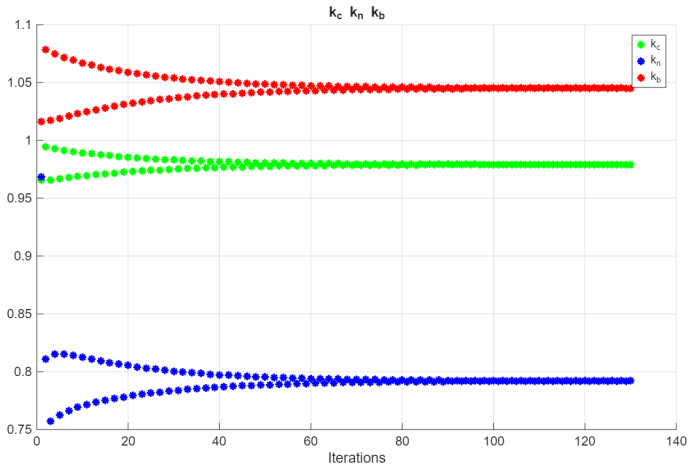


**(a)** Calibration constants evolution of the ($LH_2$) configuration

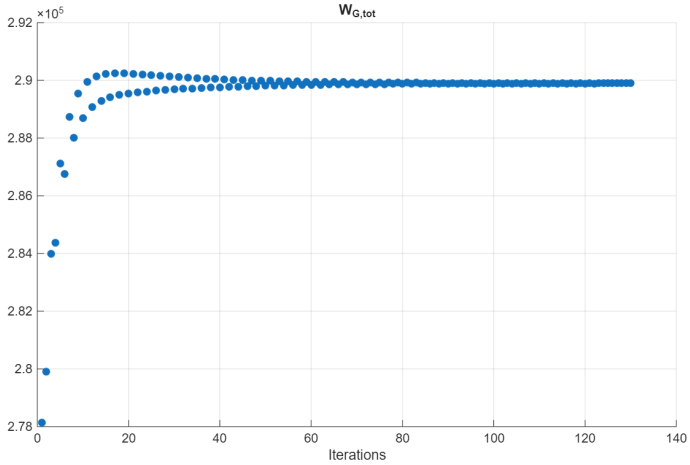


**(b)** Total gross weight evolution of the ($LH_2$) configuration

**Figure 6.2:** Side-by-side comparison of the $LH_2$ and LNG vehicle configurations.

To illustrate the operational performance of this configuration, the corresponding **Payload and Fuel vs Range diagram** was generated and is presented in Figure 6.3. This chart depicts the vehicle's range capability as a function of both payload mass and fuel mass. The characteristic points defining the payload curve, represented in blue, are summarised in Table 6.1.

| Point | Range [km] | Payload [kg] | Fuel [kg] |
|---|---|---|---|
| A | 0 | 19 051 | 0 |
| B | 10 000 | 19 051 | 90 543 |
| D | 11 165 | 0 | 90 543 |

**Table 6.1:** Payload Range diagram relevant points ($LH_2$)

The **Matching Charts** are identical for both the Liquid Hydrogen and Liquid Methane configurations. This outcome is a direct and intentional consequence of the model's ar-

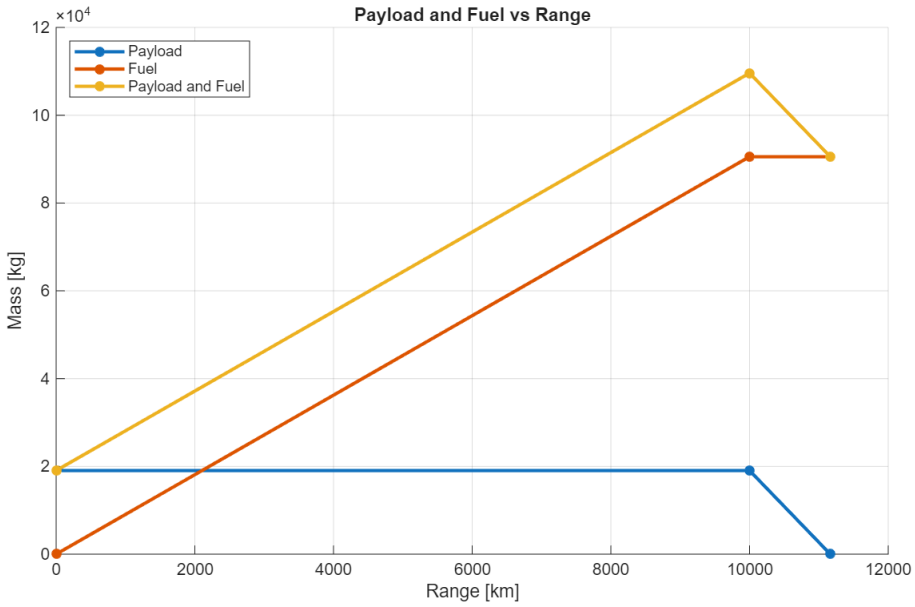


**Figure 6.3:** Fuel and Payload - Range diagram ($LH_2$)

chitecture. The sizing methodology relies on a unified aerodynamic database where the lift ($C_L$) and drag ($C_D$) coefficients used to generate the Thrust Required curve ($T_{req}$) are based on the *HYCAT-1A* reference vehicle. These coefficients are not dynamically recalculated based on geometric changes, such as fuselage length, that result from the sizing loop.

Finally, a dimensioned **sketch** of the vehicle is provided in Figure 6.4, showing the overall planform layout.

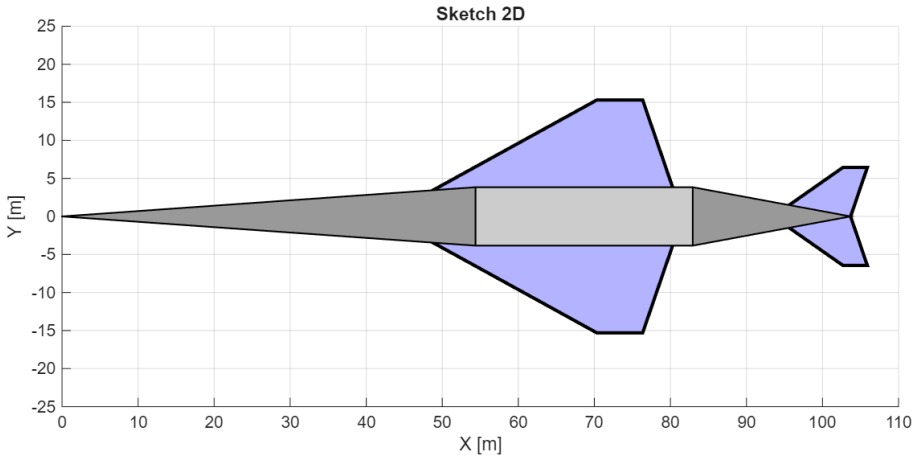


**Figure 6.4:** Sketch of the $LH_2$-powered configuration

## 6.3 Direct comparison and discussion: LNG vs $LH_2$

This section performs the final direct comparison between the **Liquid Methane (LNG)** vehicle and the **Liquid Hydrogen ($LH_2$)** variant. The primary objective is to quantita-

tively assess the engineering trade-offs between the two cryogenic fuels, using the results generated by the sizing code.

For a clear side-by-side analysis, the key sizing metrics for both configurations are presented in Table 6.2. These specific parameters were selected as they best represent the designs, capturing the interplay between the main mass properties, the key geometric results, and the resulting aerodynamic efficiency (L/D).

| **Parameter** | **LNG Baseline** | **$LH_2$ Variant** | **% Change** |
|---|---|---|---|
| *Mass Parameters [kg]* | | | |
| Gross Mass, $M_{G,tot}$ | 412 336 | 289 899 | -29.7% |
| Operating Empty Mass (OEM) | 213 275 | 199 351 | -6.5% |
| Total Fuel Mass | 199 065 | 90 543 | -54.5% |
| Tank Structure Mass | 12 400 | 30 181 | +143.4% |
| *Geometric & Volumetric Parameters* | | | |
| Vehicle Length [m] | 98.74 | 103.70 | +5.0% |
| Fuselage Diameter [m] | 6.56 | 6.88 | +4.9% |
| Wing Reference Area, $S_{ref}$ [$m^2$] | 982.00 | 690.40 | -29.7% |
| Total Wetted Area, $S_{btot}$ [$m^2$] | 1 555 | 1 714 | +10.2% |
| Total Fuel Volume [$m^3$] | 442.4 | 1 275.3 | +188.3% |
| Total Vehicle Volume [$m^3$] | 2 333.0 | 2 700.7 | +15.8% |
| *Aerodynamic Performance* | | | |
| Cruise L/D Ratio, E | 5.911 | 4.315 | -27.0% |

**Table 6.2:** Side-by-Side Sizing Comparison: LNG vs. $LH_2$ Configurations.

The data in the table reveal a deep and complex engineering trade-off. The primary **advantage** of the $LH_2$ configuration is, as expected, its superior propulsive efficiency. Driven by a much higher $I_{sp}$, the $LH_2$ variant requires a remarkable **54.5 % less *Fuel Mass*** to complete the same mission. However, the most revealing metric is the **Operating Empty Mass (OEM)**. Although the *Tank Structure Mass* for the $LH_2$ variant is much higher (+143.4 %) due to the massive *Fuel Volume*, the final OEM of the vehicle is actually **6.5 % lighter** than the LNG baseline. This seemingly counter-intuitive result is a direct consequence of the sizing loop logic: the 54.5 % reduction in *Fuel Mass* leads to a 29.7 % lighter *Gross Mass*. This lighter aircraft requires a proportionally smaller wing to support it, as seen from the *Wing Reference Area* ($S_{ref}$), which is also 29.7 % smaller. A smaller wing then results in a significantly lighter wing structure, and this mass reduction is large enough to offset the penalty of the heavier hydrogen tanks. The identical reduction in Gross Mass and $S_{ref}$ is not a coincidence. It is a direct consequence of the design methodology, where the **wing loading (W/S)** was maintained **constant** as a top-level constraint, matching that of the reference aircraft.

The **true penalty** of using hydrogen, therefore, is not structural, but rather **volumetric and aerodynamic**. The $LH_2$-powered vehicle requires 188.3 % more *Fuel Volume*, which

means a *Fuselage Geometry* that is longer (+5.0 %) and wider (+4.9 %). This geometric expansion is also confirmed by the *Total Volume* (+15.8 %) and the *Total Wetted Area* ($S_{btot}$) of the vehicle, which increases by 10.2 %.

This larger, less-streamlined shape directly impacts the **aerodynamic efficiency** of the aircraft. As shown in the table, the $LH_2$ variant suffers a severe 27.0 % reduction in its *cruise L/D ratio*. It is important to note that within the sizing model, the calculation of the Lift-to-Drag ratio is primarily driven by $S_{ref}$ and the *Total Volume* of the vehicle. The *Total Wetted Area* metric serves as a valuable diagnostic output which, increasing even if $S_{btot}$ itself is not a direct input to the L/D calculation, provides confidence that the code correctly captures the geometric consequences of fuel choice.

In summary, the comparison shows that the trade-off is not just a simple 'mass-only' comparison as the fuel choice affects multiple and conflicting design aspects. The analysis demonstrates that, despite being 27.0 % less aerodynamically efficient, the superior specific energy of Liquid Hydrogen is significant enough to overcome the other design penalties. This is what allows the $LH_2$ vehicle to achieve a lighter *Gross Mass* (−29.7 %).

Although Table 6.2 provides the quantitative data, this fundamental design difference is best illustrated visually. Figure 6.5 can be used to present the converged vehicle layouts for both configurations, appropriately scaled, highlighting the differences in the wing surface, fuselage length, and overall vehicle shape driven by fuel choice.

### 6.3.1 Fuel cost analysis

The comparative analysis was extended to a preliminary estimate of the **operating fuel cost**. It is important to note that the current (2025) market prices for green liquefied $LH_2$ are extremely high, often exceeding €10.00 per $kg$, due to the highly-dispendious and low-scale nature of the current production and liquefaction process. Therefore, this analysis uses more relevant **industrial cost projections for a 2035 scenario**, which assume a mature, large-scale production market.

The following procurement costs were assumed, based on industry projections such as those of the *International Energy Agency (IEA)* [18]:

- **LNG Cost: €0.50 per kg**
- **Green $LH_2$ Cost: €2.00 per kg**, based on a production target of €1.00/kg, plus an additional €1.00/kg for liquefaction and logistics.

Applying these costs to the required fuel masses per mission, as defined in Table 6.2, yields the propellant cost per flight:

- **LNG Mission Cost:** $199,065\,kg \times €\ 0.50/\text{kg} =$ **€99,533**
- **$LH_2$ Mission Cost:** $90,543\,kg \times €\ 2.00/\text{kg} =$ **€181,086**

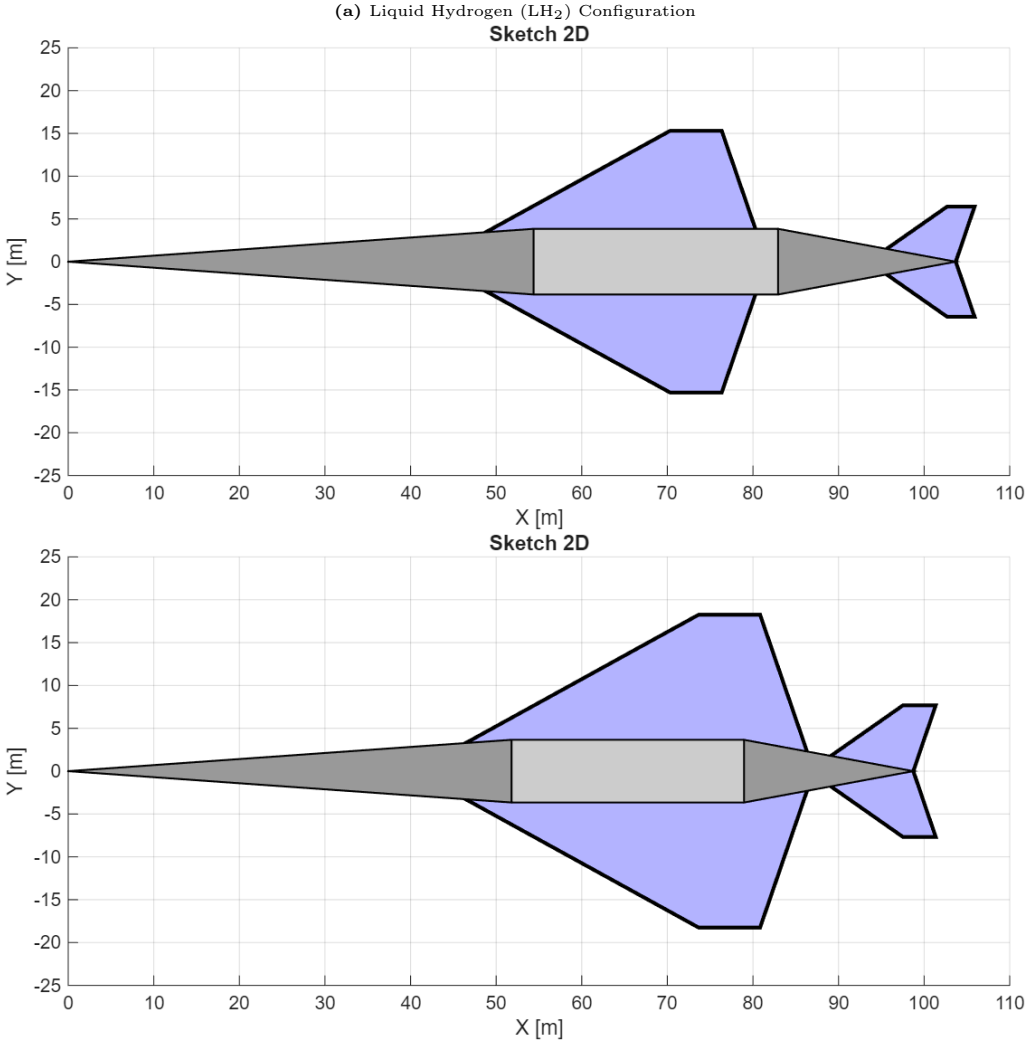


**(a)** Liquid Hydrogen ($LH_2$) Configuration

**(b)** Liquid Natural Gas (LNG) Configuration

**Figure 6.5:** Side-by-side comparison of the $LH_2$ and LNG vehicle configurations.

This economic analysis highlights a result that is the inverse of the mass analysis. Although the $LH_2$ vehicle is lighter and requires 54.5% less fuel mass, its propellant cost per mission in this 2035 scenario is estimated to be **82 % higher** than its LNG-powered counterpart.

This shows that while $LH_2$ offers a clear advantage in terms of MTOW, the LNG configuration appears to be the most economically viable solution from a propellant cost perspective. A cost **parity point** would only be reached if the delivered cost of green $LH_2$ fell to approximately **€1.10 per kg**, a scenario currently considered extremely optimistic.

### 6.3.2 Environmental Impact Assessment

Finally, the comparison was extended to evaluate the environmental footprint. Using standard stoichiometric emission indices ($EI$), the total mass of Carbon Dioxide ($CO_2$) and Water Vapor ($H_2O$) released per mission were estimated.

It is crucial to premise that compared to conventional **Jet A-1 (Kerosene)**, the **LNG** solution adopted in this thesis already represents a significant improvement: methane combustion naturally produces $\approx$ 15% less $CO_2$ per $kg$ than kerosene, and eliminates completely the emission of particulate matter (soot).

Comparison of the two cryogenic solutions analyzed:

- **LNG Emissions:**
  - $CO_2$: **547,429 kg**
  - $H_2O$: **447,896 kg**
- **$LH_2$ Emissions:**
  - $CO_2$: **0 kg**
  - $H_2O$: **814,887 kg**

Although the $LH_2$ configuration provides the clear benefit of zero carbon emissions, this comes with a major trade-off that is often underestimated: **Water Vapor emission**. From the analysis, it appears that the $LH_2$ vehicle releases almost **double the water vapor** (+82%) compared to the LNG baseline.

This difference is due to the chemical properties of the fuels: while burning 1 kg of methane produces about 2.25 $kg$ of water ($EI_{H2O} \approx 2.25$), burning hydrogen produces nearly 9 $kg$ ($EI_{H2O} \approx 9$). Even though the hydrogen aircraft carries significantly less fuel mass, this is not enough to balance out such a high production rate of water.

For a conventional aircraft flying at lower altitudes, this might be a minor issue. However, for **hypersonic flight**, the context is different. These vehicles operate in the stratosphere, where water vapor acts as a greenhouse gas and can lead to the formation of persistent contrails that trap heat in the atmosphere.

For these reasons, LNG represents a very effective compromise. It allows for a significant reduction in carbon emissions compared to kerosene, but avoids injecting the extreme amounts of water vapor that are unavoidable with hydrogen propulsion.

Finally, regarding **$NO_x$ (Nitrogen Oxides)**, LNG offers some physical advantages. Methane burns cleaner than kerosene, producing almost **no soot**, and does not contain the fuel-bound nitrogen often found in jet fuels. Methane has also a lower peak flame temperature compared to hydrogen. Since high temperatures are the main driver for thermal $NO_x$ formation, the use of methane could simplify the thermal management of the engine and help keep emissions within limits.

# Chapter 7

# Conclusions and Future Work

## 7.1 Summary of the Analysis

The primary objective of this thesis was the preliminary design and performance evaluation of a 200-passenger hypersonic transport aircraft powered by **Liquid Methane (LNG)**. The goal was to assess the viability of LNG as an alternative cryogenic fuel, quantifying its impact on the vehicle's sizing compared to a more conventional cryogenic option.

To achieve this, a comprehensive sizing methodology based on the "HASA framework" was implemented in *MATLAB*. This computational tool was specifically adapted to manage the unique properties of different fuels, integrating a dynamic iterative calculation for the fuel required during cruise rather than relying only on fixed-fraction estimates.

The analysis successfully yielded a feasible design for the LNG-powered configuration. To contextualise these results a comparative analysis was performed against a **Liquid Hydrogen ($LH_2$)** powered variant which was designed to the exact same mission requirements (200 pax, same range) and top-level constraints.

## 7.2 Discussion of Key Results

The side-by-side comparison, detailed in Table 6.2, revealed a deep and complex engineering trade-off. As expected, the $LH_2$ variant benefits enormously from hydrogen's high specific energy (calorific value), which translates to a superior $I_{sp}$. This results in a remarkable **54.5% reduction in the required fuel mass**.

This massive fuel saving is the primary driver for the $LH_2$ vehicle's **29.7% lower Maximum Take-Off Mass (MTOM)**. Perhaps even more significantly, this mass advantage extends to the **Operating Empty Mass (OEM)**, which results **6.5% lower** than the LNG baseline, despite the fuel tanks being **143.4% heavier**.

This significant reduction across all mass metrics is explained by the constraints im-

posed by the design methodology. Since the top-level performance requirements (defined by the Matching Charts) and the aerodynamic coefficients were kept identical for both configurations, the **solution space** remained constant. Consequently, the final design point was driven by the same limiting values for **wing loading ($W/S$)** and **thrust-to-weight ratio ($T/W$)**. This fixed design point leads to a significant secondary mass reduction: because the MTOM of the $LH_2$ vehicle is much lower, the *absolute thrust* required ($T = T/W \times W_{MTOM}$) is proportionally lower, allowing for smaller and lighter engines. Similarly, the constant $W/S$ dictates a smaller reference wing area, reducing the structural mass of the wing. These combined savings in propulsion and structure are large enough to completely offset the penalty of the heavier cryogenic tanks, resulting in a lighter vehicle overall.

However, the analysis also quantified the severe **volumetric and aerodynamic penalties of using $LH_2$**. The hydrogen vehicle requires 191.3 % more fuel volume, requiring a longer and wider fuselage. This geometric "bloat" results in a less-streamlined shape which, even within the model's simplified aerodynamic calculation, led to a reduction in the cruise L/D ratio.

In summary, the LNG configuration, while resulting in a significantly heavier aircraft, represents a more geometrically balanced and aerodynamically efficient design. The $LH_2$ configuration achieves a lower MTOW, but at the price of extreme volumetric demands and a significant penalty for aerodynamic efficiency.

## 7.3 Limitations and Future Work

This analysis provides a robust comparison at the preliminary design level, but is based on several key simplifications that must be addressed in future work.

The first limitation is the modeling of the **cryogenic tanks**. The analysis relied on a simplified mass fraction (tank mass / fuel mass) which, as an assumption, was held constant for both fuel types. A detailed thermo-structural analysis of the multi-layer insulation (MLI) and boil-off management systems is therefore a critical next step. Such an analysis would quantify the severe engineering challenge of storing $LH_2$ at $-253^\circ C$, a far greater task than for LNG at $-162^\circ C$, likely strengthening the case for the LNG design by revealing the complexity and mass penalty of the $LH_2$ storage system.

Another limitation is the **aerodynamic model**, since the coefficients (e.g., $C_{L,max}$, $C_{D,0}$) used in the analysis were derived from the *Hycat-1A* and maintained constant for both the LNG and $LH_2$ variants. This assumption represents an oversimplification, as the sizing loop converged to two vehicles with significantly different wing area and volumes. The drop in L/D for the $LH_2$ vehicle was driven by the total volume and the reference surface of the wing, not by a true aerodynamic re-evaluation. A higher-fidelity model would find that the larger $LH_2$ airframe produces a higher zero-lift drag coefficient ($C_{D,0}$) due to its

increased wetted area. This new, higher $C_D$ would, in turn, directly alter the performance constraint curves in the **matching charts** (especially for climb and cruise). This feedback would likely increase the required $T/W$ for the $LH_2$ vehicle, affecting the entire converged solution in a way this study could not capture.

Based on these limitations, the following steps are recommended for future research:

1. **Detailed Tank Design:** A dedicated study on the structural and thermal design of the non-cylindrical, conformal cryogenic tanks required to fit inside the fuselage, comparing the specific insulation and mass penalties for LNG and $LH_2$.
2. **Economic and Cost Analysis:** This thesis provided a preliminary analysis of the propellant cost, which revealed a clear operational economic advantage for the LNG variant in a 2035 scenario. However, this initial finding should be expanded into a comprehensive Life Cycle Cost (LCC) study. Such an analysis would be required to determine the overall economic viability of the two concepts. It would need to factor in not only the operational fuel cost but also the enormous infrastructure development costs, where the existing global supply chain of LNG would be a significant benefit.
3. **Integrated Aerodynamic Analysis:** This step involves the development of a parametric CAD model of the vehicle, which would be integrated with the *MATLAB* sizing loop. This integration would enable the code to automatically generate the final converged vehicle geometry, which could then be passed to a CFD solver or a high-fidelity panel method to calculate the specific aerodynamic coefficients corresponding to that design.
4. **$NO_x$ Quantification:** While this study qualitatively discussed the potential advantages of LNG regarding $NO_x$ formation, a precise quantitative assessment is lacking. Future work should integrate detailed chemical kinetics simulations to model the combustor. This is crucial to accurately compare the thermal-$NO_x$ produced by the high-temperature hydrogen flame versus the methane flame and to assess their respective impacts on the stratospheric ozone layer.

# Appendix A

# The International Standard Atmosphere (ISA) Model

The accurate calculation of aircraft performance, particularly for supersonic or high altitude flight, requires a standardised definition of the atmosphere's properties. For this purpose, the **International Standard Atmosphere (ISA)**, defined by the International Civil Aviation Organization (ICAO), is the universally accepted static atmospheric model used in aerospace engineering.

The ISA model is a hypothetical, idealised description of the atmosphere's mean conditions, based on a set of reference values at Sea Level (SL) and an assumed vertical temperature gradient profile.

## A.1 ISA reference conditions (Sea Level)

The standard defines the following baseline properties at an altitude of $h = 0$ m (mean sea level):

| **Parameter** | **Symbol** | **Value** | **Unit** |
|---|---|---|---|
| Temperature | $T_0$ | 288.15 | K (15°C) |
| Pressure | $p_0$ | $101,325$ | Pa |
| Density | $\rho_0$ | 1.225 | $\mathrm{kg/m^3}$ |
| Lapse Rate (Troposphere) | $L_{\mathrm{trop}}$ | $-0.0065$ | K/m |
| Lapse Rate (Stratosphere) | $L_{\mathrm{str}}$ | 0.001 | K/m |

**Table A.1:** ISA Sea Level Reference Values

## A.2 Altitude layers and governing equations

The ISA model divides the atmosphere into distinct layers, each characterised by a specific temperature gradient (*lapse rate*). Within each layer, pressure ($p$), temperature ($T$), and density ($\rho$) are determined using the hydrostatic equation and the ideal gas law.

The implemented function, `isa_atmosphere(h)`, utilises these principles and defines the following primary layers up to 32 km:

### A.2.1 Troposphere, $0 \text{ m} < h < 11,000 \text{ m}$

- Gradient: Constant temperature decrease ($L_{\text{trop}} = -0.0065$ K/m).
- Governing Equations:

$$T = T_0 + L_{\text{trop}} \cdot h$$
$$p = p_0 \left( \frac{T}{T_0} \right)^{-\frac{g}{L_{\text{trop}} R}}$$

### A.2.2 Tropopause (isothermal layer), $11,000 \text{ m} < h < 20,000 \text{ m}$

- Gradient: Zero temperature change ($L_{\text{iso}} = 0$ K/m).
- Governing Equation: The temperature is constant ($T_{\text{trop}} = 216.65$ K), and the pressure decreases exponentially:

$$p = p_{\text{trop}} \cdot e^{-\frac{g\,(h - h_{\text{trop}})}{R\,T_{\text{trop}}}}$$

### A.2.3 Lower stratosphere, $20,000 \text{ m} < h < 32,000 \text{ m}$

- Gradient: Positive temperature increase ($L_{\text{str}} = 0.001$ K/m).
- Governing Equations:

$$T = T_{\text{trop}} + L_{\text{str}}(h - h_{\text{iso}})$$
$$p = p_{\text{iso}} \left( \frac{T}{T_{\text{trop}}} \right)^{-\frac{g}{L_{\text{str}} R}}$$

## A.3 Application in aircraft performance calculations

The ISA model is crucial for normalising and comparing aircraft performance data. Specifically, the model provides the following essential parameters for the thesis calculations:

- The **atmospheric density** ($\rho$), computed from the calculated pressure and temper-

ature using the Ideal Gas Law:

$$\rho = \frac{p}{R \cdot T}$$

- The **density ratio** ($\sigma$), which is the ratio of local density to sea level density ($\rho_0$), and it is a fundamental parameter for aerodynamic analysis, especially in calculating lift and drag forces:

$$\sigma = \frac{\rho}{\rho_0}$$

- The **temperature** ($T$), necessary for determining the local **speed of sound** ($a$), which is only a function of temperature in a dry gas like the atmosphere:

$$a = \sqrt{\gamma R T}$$

where $\gamma$ is the ratio of specific heats ($\approx 1.4$) and $R$ is the specific gas constant for air. The speed of sound $a$ allows the conversion between the Mach number and the True Airspeed $V$ ($M = V/a$). The ccurate determination of $T$ from the ISA model is therefore indispensable for all flight regime analysis.

# Bibliography


[1] C. Pirrello, A. Baker, and J. Stone, "A fuselage/tank structure study for actively cooled hypersonic cruise vehicles, summary," NASA, Tech. Rep., 1976.

[2] R. Hawkins and J. A. Penland, "Invariance of hypersonic normal force coefficients with reynolds number and determination of inviscid wave drag from laminar experimental results," NASA, Tech. Rep., 1997.

[3] R. Morris and G. Brewer, "Hypersonic cruise aircraft propulsion integration study, volume 2," NASA, Tech. Rep. CR-158926-2, 1979.

[4] W. Huang, L. Yan, and J.-g. Tan, "Survey on the mode transition technique in combined cycle propulsion systems," *Aerospace Science and Technology*, vol. 39, pp. 685–691, 2014.

[5] A. M. Z. H. Almeldein, "Propulsion system selection & optimization for a hypersonic civil transport," Ph.D. dissertation, Faculty of Engineering at Cairo University, 2011.

[6] R. Morris and G. Brewer, "Hypersonic cruise aircraft propulsion integration study, volume 1," NASA, Tech. Rep. CR-158926-1, 1979.

[7] G. J. Harloff and B. M. Berkowitz, "Hasa: Hypersonic aerospace sizing analysis for the preliminary design of aerospace vehicles," NASA, Tech. Rep. CR-182226, 1988.

[8] J. Roskam, "Preliminary sizing of airplanes," *Airplane Design*, pp. 5–196, 1988.

[9] A. Ingenito, S. Gulli, and C. Bruno, "Preliminary sizing of an hypersonic airbreathing airliner," *Transactions of the Japan Society for Aeronautical and Space Sciences, Aerospace Technology Japan*, vol. 8, no. ists27, pp. 19–28, 2010.

[10] C. Glatt, "Waats: A computer program for weights analysis of advanced transportation systems," NASA, Tech. Rep., 1974.

[11] B. Oman, *Vehicle Design Evaluation Program, Technical Report: A Computer Program for Weight Sizing, Economic, Performance & Mission Analysis of Fuel-conservative Aircraft, Multibodied Aircraft & Large Cargo Aircraft Using Both JP & Alternative Fuels*. National Aeronautics and Space Administration, Langley Research Center, 1977.

[12] J. B. Whitlow, J. D. Eisenberg, and M. D. Shovlin, *Potential of Liquid-Methane Fuel for Mach 3 Commercial Supersonic Transports*. National Aeronautics and Space Administration, 1966, vol. 3471.

[13] R. A. Jones and P. W. Huber, "Toward scramjet aircraft," *Astronautics and Aeronautics*, vol. 16, 1978.

[14] J. G. Leishman, "Wing shapes & nomenclature," *Introduction to Aerospace Flight Vehicles*, 2023.

[15] D. Ferretto, R. Fusaro, and N. Viola, "Innovative multiple matching charts approach to support the conceptual design of hypersonic vehicles," *Proceedings of the Institution of Mechanical Engineers, Part G: Journal of Aerospace Engineering*, vol. 234, no. 12, pp. 1893–1912, 2020.

[16] L. K. Loftin Jr, "Subsonic aircraft: Evolution and the matching of size to performance," NASA, Tech. Rep. L-13367, 1980.

[17] E. Botero et al., "Suave: An open-source environment for conceptual vehicle design and optimization," in *54th AIAA aerospace sciences meeting*, 2016.

[18] International Energy Agency (IEA), *Global Hydrogen Review 2023*. IEA, 2023. [Online]. Available: https://www.iea.org/reports/global-hydrogen-review-2023.